Kinetic Inductance Detectors and Metal-Mesh Filters for Far-Infrared Astronomy

by

Joanna Perido

B.A., University of Texas at San Antonio, 2016

M.S., University of Colorado Boulder, 2021

A thesis submitted to the

Faculty of the Graduate School of the

University of Colorado in partial fulfillment

of the requirements for the degree of

Doctor of Philosophy

Department of Physics

2023

Committee Members:

Prof. Nils Halverson, Chair

Dr. Jason Glenn

Prof. Kevin France

Prof. Konrad Lehnert

Prof. Charles Rogers

Dr. Joel Ullom

Perido, Joanna (Ph.D., Physics)

Kinetic Inductance Detectors and Metal-Mesh Filters for Far-Infrared Astronomy

Thesis directed by Dr. Jason Glenn

This thesis focuses on the development and characterization of superconducting detectors, known as kinetic inductance detectors (KIDs), for mid- to far-infrared (IR) observatories. KIDs are a form of cryogenic superconducting detector that are easy to multiplex into large arrays and offer equal or better sensitivity than other cryogenic detectors [64]. They can detect a range of wavelengths and are very popular in submillimeter (submm) and millimeter (mm) astronomy. I will present work on three different KID prototype arrays for the proposed observatories The Balloon Experiment for Galactic INfrared Science (BEGINS), The Galaxy Evolution Probe (GEP), and The PRobe far-Infrared Mission for Astrophysics (PRIMA). I will discuss their dark and optical performance and sensitivities. I will also present the design and characterization of a prototype mid- to far-IR linear variable filter (LVF), which will define the bandpasses of the detectors for the lower wavelength ranges of BEGINS and PRIMA. LVFs are filters with bandpasses that vary linearly along one direction. This work is necessary to increase the technology readiness of lens-coupled KIDs and LVFs that enable compact instruments for space-based observatories.

Dedication

To my supportive parents, who taught me to be resilient and never give up.

To all minorities in STEM, who continue to strive in a field that many times feels hard to belong to.

Acknowledgements

I am extremely grateful to all those who have helped me on this journey towards a PhD. First, I would like to thank all of my family and friends! They have supported me in every way possible and always encouraged me to keep going when I wanted to give up. I am very blessed to have such an amazing support system. I would also like to thank all of my colleagues that have contributed to my success in attaining a PhD. I am very thankful to my advisor, Jason Glenn, for being understanding during the different obstacles faced in the past years. I would like to thank Peter Day, Steven Hailey-Dunsheath and Edward Wollack, who took the time to answer any questions I had to improve my understanding of our work. I am especially grateful to Peter Day, without his collaboration I would not have been able to complete the research in this thesis. I would like to thank Nicholas Cothard, who was always patient when I needed any sort of help, taught me how to navigate and run a lab and basically trained me in instrumentation. I am so glad you decided to join our group when you did! I would like to thank Nils Halverson, who helped me fix my thesis and gave me detailed edits on such short notice. To all the grad students I got close to, thanks for being so awesome! Jose Valencia and Ting-Wei Hsu, I would not have survived Boulder without the both of you! Thank you for always being available to hangout and take phone calls when things got stressful. Maria Prado (from another Univ.), thank you for teleworking with me and making it less lonely while I worked on my thesis. I am not sure I would have finished without the extra motivation! The work in this thesis was made possible by the funding of NASA's Future Investigators in NASA Earth and Space Science and Technology Grant, Grant NNH19ZDA001N-FINESST. Again, I am SUPER grateful!! :)

Contents

Tables

Table

Figures

Figure

Chapter 1

Motivation

This thesis focuses on the development and characterization of superconducting detectors, known as kinetic inductance detectors (KIDs), and optical bandpass filters for mid- to far-infrared (IR) observatories. In this chapter I will give a brief overview of the mid- to far-IR astronomy that motivates the development of these detectors and filters, I will present various mid- to far-IR observatories and their contribution to astronomical science, and I will introduce two proposed observatories that set the technological requirements for the detectors and filters presented in this thesis. At the end of the chapter I will discuss the organization of the rest of this thesis.

1.1 Mid- to Far-IR Astronomy

Observations of the mid- and far-IR ($\sim$3 μm - 1000 μm) are necessary to explore the origins of galaxies, stars, and planets that make up the universe. They enable us to study dust-obscured active galactic nuclei, super massive black hole accretion rates, star formation rates, planet formation, the history of galaxy growth, the growth of metals over the age of the universe, comets, and asteroids to name a few [15, 21, 66, 84]. Below I briefly discuss observed mid- and far-IR spectral features that enable the study of star formation and galaxy evolution and planetary systems.

Star Formation and Galaxy Evolution: Stars are formed by gravitational collapse deep inside cold molecular gas and dust clouds, which makes them opaque at visible or near-IR wavelengths. The radiation from newly formed stars heats the surrounding dust which cools by emitting radiation in the mid- to far-IR. Studying the re-emitted radiation from dust grains in the interstellar medium (ISM) and intergalactic medium (IGM) helps astronomers learn about the dynamics behind star formation and active galactic nuclei activity. Spectral features observed in the far-IR used to trace star formation include emission and absorption of atomic spectral lines such as [O I] 63 μm, [N II] 122 μm, [C II] 158 μm, and several hydrogen recombination lines. Among the dust grains are polycyclic aromatic hydrocarbons (PAHs) which have broad emission bands spanning 3-12 μm. PAHs are illuminated by ultra-violet bright stars and can make up to 10% of the total infrared luminosity in star forming galaxies. These mid- to far-IR measurements are important for understanding the dominant mechanism that powers the IR emission of galaxies and in addressing problems such as, why star formation and supermassive black hole accretion peaked at redshifts of z = 2 to 3 and have declined since then [31].

Planetary Systems: Far-IR continuum observations measure the dynamics and evolution of protoplanetary disks, which allow us to understand the early formation stages of solar systems [31]. Fig. 1.1 shows a model of the mid- to far-IR emission of a protoplanetary disk which spans 4-800 μm. There are still a lack of observations in the far-IR of protoplanetary disks where the water distribution and evolving chemistry can help identify the differences between habitable and lifeless planets [62]. From far-IR observations astronomers can also characterize the atmospheric structure and composition of the ice and gas giant planets and their satellites. The future high priority flagship mission Uranus Orbiter and Probe will study the in situ heat flux of this icy giant's atmosphere in seven spectral bands spanning wavelengths from 0.2 to 300 μm [4, 77].

The two general approaches taken for these measurements are photometry/imaging or spectroscopy. Photometry is used for measurements that require a spectral resolution of R=3 to 10, this includes continuum measurements of dust grains. Spectroscopy is required for measurements with spectral resolution greater than 10^6, and is mostly used to characterize molecular and atomic spectral lines. In the following Section I will discuss a few mid- to far-IR observatories with instruments capable of making these measurements and two proposed observatories that I have contributed to with my dissertation research.

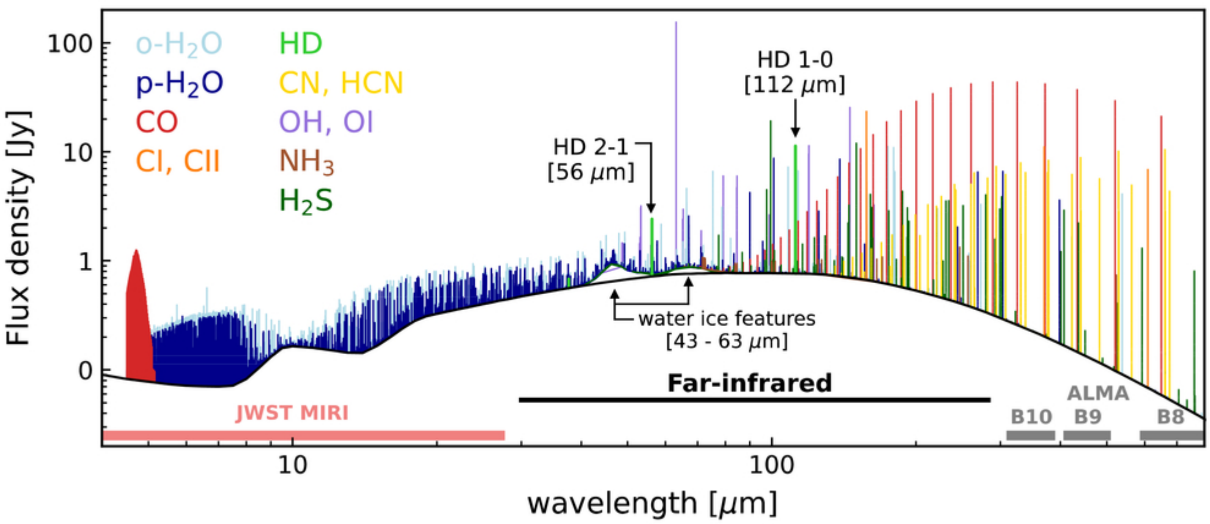

Figure 1.1: Model spectrum of a protoplanetary disk taken from [62]. The mid-IR and submm regions have spectral coverage by JWST's MIRI instrument and ALMA, respectively. However, there is a lack of coverage in the far-IR region where water molecule emission features may be found to help identify the differences between habitable and lifeless planets. The proposed observatory, PRIMA, discussed in Sec. 1.3.2 will be capable of resolving these emission features.

1.2 Past and Current Mid- to Far-IR Observatories

In this section I discuss past and current mid- to far-IR observatories and their contribution to astronomy and will put in context the space observatories discussed in Sec. 1.3.

The requirements for mid- to far-IR observatories are that they be cooled to cryogenic temperatures and be placed at high elevation or in space. They must be cooled so that the thermal radiation from the instrument does not dominate the instrument noise. They must be at high elevation due to Earth's atmosphere which absorbs infrared wavelength emission. The first space observatory to observe IR wavelengths was the Infrared Astronomical Satellite (IRAS) [79]. IRAS was a space telescope launched on Jan. 25, 1983. It mapped 96% of the sky at 12, 25, 60 and 100 μm and discovered over 250,000 IR sources. Since then many other IR observatories have been launched. The Infrared Space Observatory (ISO) was launched in 1995 to study IR wavelengths from 2.5 to 240 μm [53]. It was one of the observatories that confirmed radiation from dust was absorbed and re-emitted in the IR. Below I discuss a few more of these observatories and their contributions to astronomy.

Atacama Large Millimeter/Submillimeter Array (ALMA): ALMA is a ground-based radio telescope array in the Atacama Desert in Chile. It observes wavelengths from 300 μm to 8.5 mm with 66 dish antennae operated interferometrically [107]. The individual antennas can be arranged in different configurations depending on the desired spectral resolution and sensitivity of the observation. This has allowed for many ground breaking discoveries. However, due to Earth's atmosphere ALMA is blind to far-IR spectral lines necessary for measuring star formation between redshifts of $0.5 < z < 3$.

Herschel: Herschel was a space observatory that operated at the second Lagrange point (L_2) of the Earth-Sun system from 2009 to 2013. It had a 3.5-m passively-cooled mirror and observed from 60 μm to 670 μm with three different instruments, the Photodetector Array Camera and Spectrometer (PACS) which had an imaging photometer and an integral field spectrometer, the Heterodyne Instrument for the Far Infrared (HIFI) which was a heterodyne spectrometer, and the

Spectral and Photometric Imaging REceiver (SPIRE) [86]. These instruments enabled advances in many disciplines from the study of comets to the study of gas in nearby galaxies.

Spitzer Space Telescope: Spitzer was a space observatory in operation from 2003-2020 and was the ISO's successor. It featured a cooled 85-cm primary mirror with three instruments including imagers and spectrometers. The Infrared Array Camera (IRAC) was an imaging camera for four bands at 3.6 μm, 4.5 μm, 5.8 μm and 8 μm [32]. The Multiband Imaging Photometer for Spitzer (MIPS) (made for longer wavelengths) imaged in three bands at 24 μm, 70 μm and 160 μm [103]. The Infrared Spectrograph (IRS), contained four separate slit spectrometers that combined to observe the 5.3 - 38 μm band [46]. With these instruments Spitzer was able to resolve dusty galaxies from the cosmic infrared background and measure star formation to $z > 3$ [34].

James Webb Space Telescope (JWST): JWST is a space observatory that operates at L_2 and launched in December 2021. JWST, is the newest IR observatory with several innovative technologies developed to make groundbreaking observations in the near and mid-IR [14]. It has a segmented primary mirror with an active area of 6.6 m. The mirror and all instruments are cooled to 50 K. The Near InfraRed Camera (NIRCam), Near Infrared Spectrograph (NIRSpec), and Near InfraRed Imager and Slitless Spectrograph (NIRISS) are three of the instruments designed for imaging and spectroscopy from 0.6 μm to 5 μm. The fourth instrument, the Mid-InfraRed Instrument (MIRI), has an imager and spectrometer designed for detection from 5 μm to 28.3 μm. The first images from JWST were released in July 2022 and revealed the capability of its four instruments to produce quality science and sharp and detailed images (Fig. 1.2) [87]. Since then there have been more discoveries such as the first evidence of CO_2 on an exoplanet to detection of galaxies used to produce a new measurement of the evolving galaxy UV luminosity function from redshifts of $z = 8 - 15$ [2, 26]. Although JWST allows us to peer deeper into the universe, it is not capable of far-IR observations which could improve the measurements of dust properties as a function of their environment.

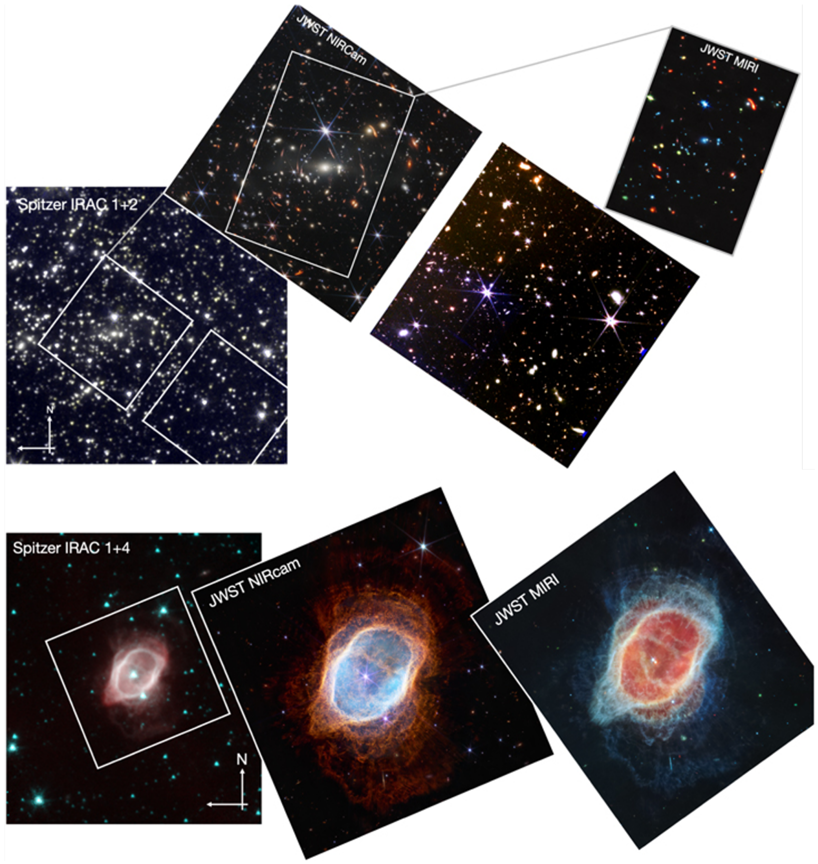

Figure 1.2: Comparisons between images produced by the Spitzer IRAC instrument and the JWST NIRCam and MIRI instruments [87]. This figure shows the capabilities and importance of observatories with improved technologies such as detectors and optical filters developed throughout the years. *Top*: Images of the galaxy cluster SMACS J0723.3-7327. *Bottom*: Images of the planetary nebula NGC 3132.

1.3 Proposed Future Mid- to Far-IR Observatories

In this section I discuss two proposed observatories that will add to and complement the mid- to far-IR astronomical science and discoveries that have been made with the observatories discussed above. The following observatories motivate the research I have performed and discuss later in this thesis.

1.3.1 Balloon Experiment for Galactic INfrared Science

The Balloon Experiment for Galactic INfrared Science (BEGINS) is a proposed sub-orbital observatory that is currently in development. BEGINS' science goal is to map the spectral energy distributions (SEDs) of interstellar dust in the vicinity of high-mass stars to measure electromagnetic radiation fields and dust properties in a variety of environments. SEDs trace the energy emitted by a source as a function of wavelength.

BEGINS will operate from 25 μm to 250 μm to map SEDs of the Cygnus molecular cloud complex centered on the DR 21 high-mass star-forming region. Fig. 1.3 shows the section of the Cygnus complex that will be observed. BEGINS will detect everything within the red contours, shown in the left image. These measurements are necessary because we currently lack observatories with the capabilities to confirm theoretical work on the predicted shapes of mid-IR SEDs, which are constructed on the assumed optical properties of dust grains in the ISM [29, 30, 49, 67]. These predicted mid-IR SED shapes show that they depend strongly on the distribution of dust grain composition and size and the illuminating radiation field. The 25 μm to 60 μm range is a unique window into both the dust grain size distribution and the radiation field intensity. Therefore, BEGINS has the capability of filling the gaps needed to confirm the shapes of mid-IR SEDs. BEGINS SED maps will also have sufficient spectral resolving power to measure and for the first time constrain the radiation field intensity, relative abundances of single- vs. multi-photon heated PAHs, and dust column density along many lines of sight. The longer wavelength bands were chosen to match Herschel's Photoconductor Array Camera and Spectrometer (70, 100, and 160 μm) and Spectral and Photometric Imaging Receiver (250 μm).

BEGINS' goals are to answer the following science questions [41]:

- Do the best current models of dust emission correctly predict the shape of the observed dust SEDs?
- How do high mass stars heat their surroundings?

- How does the dust grain size distribution change near high mass stars?

- What are the best broadband predictors of infrared luminosity?

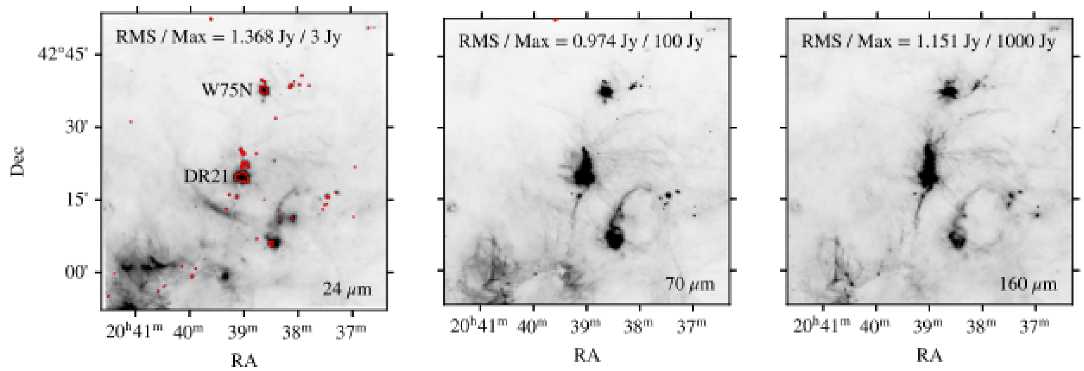

Figure 1.3: Cygnus molecular cloud complex centered on the DR 21 high-mass star-forming region imaged at different wavelengths [41]. BEGINS will detect everything within the red contours at 5σ with 10 hours of on source observing time.

1.3.1.1 BEGINS Telescope, Instrument, and Sensitivities

BEGINS will use a lightweight all-aluminum 0.5-m diameter Cassegrain telescope with a small ellipsoidal tertiary mirror in the instrument cryostat. Fig. 1.4 shows an image of the complete cryostat payload and a schematic of the telescope and instrument cross-section. BEGINS' instrument will be cooled to 300 mK and perform measurements through hyperspectral imaging from 25 μm to 65 μm with a lower limit resolving power of R=7.5 and target R=10. Resolving powers were determined through simulations that identified at R$\geq$7.5 we can separate the effects of dust grain size and radiation field intensity from 25 μm to 65 μm. Multispectral imaging will be used for wavebands centered at 70, 100, 160, and 250 μm with R = 3-6. Simulations indicated that at the longer wavebands R = 3-6 was sufficient enough for constraining dust properties. In hyperspectral imaging, many images are collected over the same spatial area at different wavelengths to create a continuous spectrum. Multispectral imaging is similar but rather than a continuous spectrum a discrete spectrum is constructed (Fig. 1.5). Spectral imaging will be achieved with the use of linear variable filters (LVFs) at the focal plane to define the bandpasses for the detectors (Fig. 1.6). LVFs are filters with bandpasses that vary linearly along their length. Our bandpasses will be defined by using metal-mesh bandpass filters which are comprised of thin film gold with cross-shaped apertures of varying sizes along the length of a silicon (Si) substrate. The filters will be anti-reflection (AR) coated on the bare Si side and metal-mesh side. Metal-mesh filters were chosen because they are compact and have a simple fabrication process. Mid-IR metal-mesh LVFs are a novel design and are a significant part of my dissertation research. They are discussed in further detail in Ch. 8.

The BEGINS detector sensitivity will be limited by the photon noise from the thermal emission of the telescope. The sensitivity is determined by the instrument's detector noise equivalent power (NEP). The optical NEP is defined as the optical power incident on the detector required to produce an output power equal to the noise output power when the optical signal is absent. Detector NEPs are discussed in greater detail in Sec. 3.3. At the focal plane of the instruments the optical NEP requirements range from 2×10^{-16} W/$\sqrt{\text{Hz}}$ to 6×10^{-17} W/$\sqrt{\text{Hz}}$ from 25-250 μm, respectively. These sensitivity requirements will be met by utilizing arrays of 1,840 lens-coupled kinetic inductance detectors (KIDs). Characterizing and measuring the response of KIDs was the bulk of my dissertation research. They will be properly introduced and discussed in detail in the following chapters. I will describe in detail the design of BEGINS KIDs and the characterization of a 25 μm prototype KID array in Ch. 5.

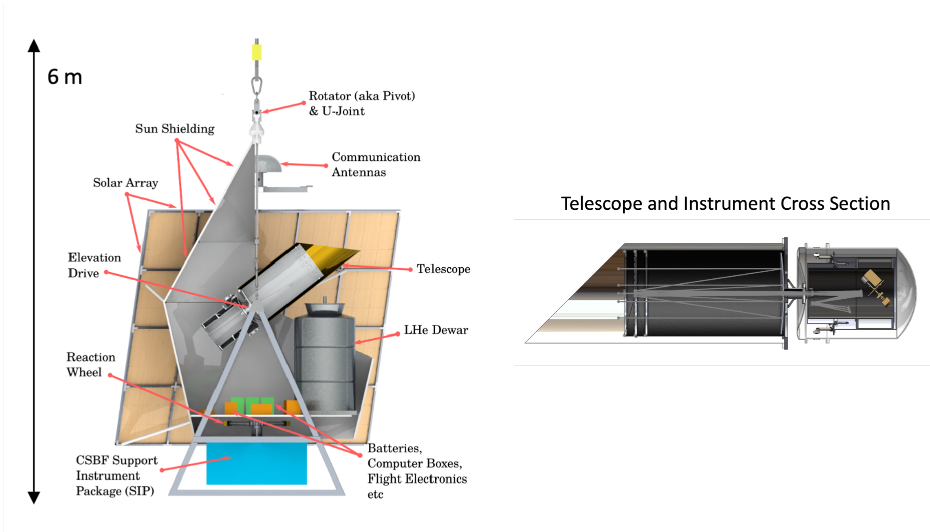

Figure 1.4: *Left*: Conceptual BEGINS gondola with major components labeled. *Right*: A zoom in of the 50-cm diameter Cassegrain telescope with its surrounding tube and the instrument cryostat. [41]

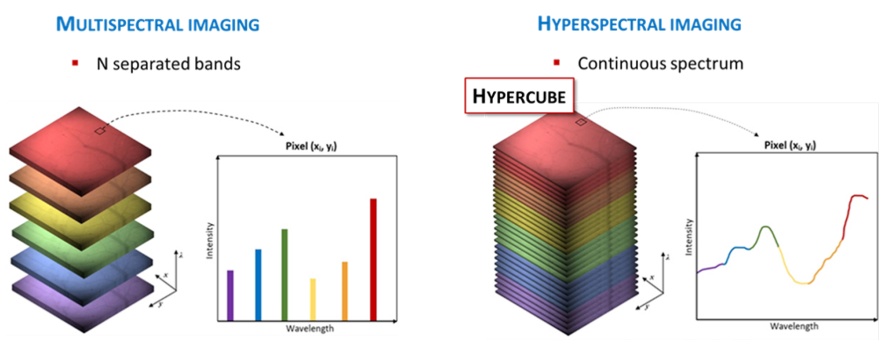

Figure 1.5: Schematic demonstration of multispectral and hyperspectral imaging [1]. In multispectral imaging many images are collected over the same spatial area at different wavelengths to produce a discrete spectrum. In hyperspectral imaging, many images are collected over the same spatial area at different wavelengths to create a continuous spectrum. The BEGINS instrument will perform both types of imaging.

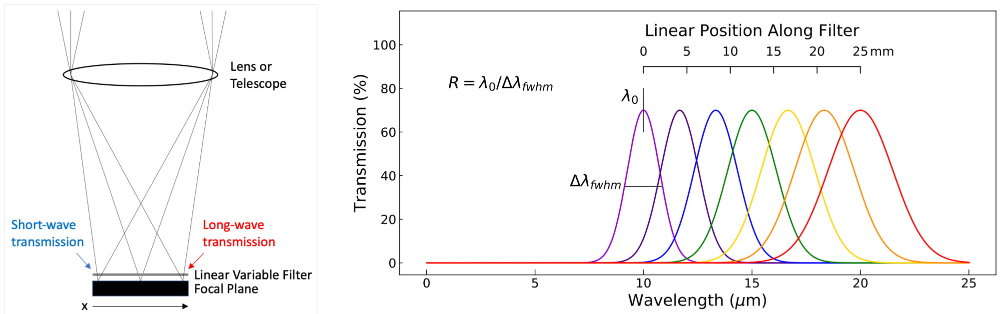

Figure 1.6: *Left*: A schematic showing how a continuous LVF is placed in an imaging optical system to create a spectral mapper. The LVF is placed directly in front of the focal plane array. *Right*: A schematic of the spectral transmission for the LVF. The bandpass central wavelength λ_0 varies continuously and smoothly along the filter length.[41]

1.3.1.2 BEGINS: Why Do We Need It?

BEGINS will demonstrate new technology to fill gaps in the current understanding of mid- to far-IR astronomy. BEGINS will be the first observatory to demonstrate a compact instrument with mid-IR LVFs and lens-coupled KIDs at the focal plane, and is important to advance technologies for future mid- to far-IR sub-orbital and orbital observatories that require sensitive detectors and cost efficient solutions. For example, the Origins Space Telescope (OST) is a 2030s Flagship mission concept that also requires large arrays of mid- and far-IR detectors to address science questions like what physical processes have governed galaxy evolution over cosmic time [31, 43, 61]. The PRobe far-Infrared Mission for Astrophysics (PRIMA) is a promising concept for a probe-class space observatory that will also utilize LVFs and lens-coupled KIDs. Since I contributed to the characterization of KIDs for PRIMA it is discussed in further detail in the following subsection, Sec. 1.3.2. BEGINS is made possible through the efforts of NASA's Goddard Space Flight Center and Jet Propulsion Laboratory (JPL).

1.3.2 PRobe far-Infrared Mission for Astrophysics

NASA's 2020 Astrophysics Decadal Survey, which identifies scientific priorities, opportunities, and funding recommendations for the next 10 years of astronomy and astrophysics, recommended

Astrophysics Probe missions. Probe missions are medium-sized missions that range within a budget of $400 million to $1 billion. The competition for probe missions will be between an X-ray probe or far-IR probe. PRIMA is a far-IR probe mission concept that will address the call for probe-class missions and is led by my advisor, Jason Glenn. It is currently under development with joint efforts between GSFC, JPL, and Caltech. At the time of this writing, a proposal is being submitted for PRIMA funding. I will briefly discuss PRIMA's science goals, telescope, instruments and sensitivity requirements.

PRIMA will operate in the wavelength range from 24 μm to 264 μm and fill the gap of wavelength coverage between ALMA and JWST. It has ambitious science goals with the hope to be an observatory for the whole astronomy community. Listed below are PRIMA's science goals[1] :

- Measure the growth of galaxies and black holes over cosmic time. PRIMA's instruments will have the capability to penetrate dust to access spectral features that uniquely measure star formation and black hole accretion in a large samples of galaxies across cosmic time.

- Measure the absolute and relative abundances of heavy elements deep in the hearts of galaxies.

- Study cosmic ecosystems. PRIMA's sensitivity to the physical conditions of the gas and dust in and around galaxies will unlock the dynamics of the galactic baryon cycle.

- Map magnetic fields in the Magellanic clouds and other nearby galaxies. This is important because magnetic fields are believed to affect star formation and galaxy evolution.

- For the first time reveal the dominant stellar accretion modes from low- to high-mass stars. This will help constrain star formation theory.

- Study the atmosphere of exoplanets and brown dwarfs to understand their formation and evolution.

[1] `https://prima.ipac.caltech.edu/page/science`

- Measure the complete spectra of hundreds to thousands of planet-forming disks, to test theories of planet formation.

- Contribute to the discovery of the origins of Earth's water. This will be done through spectroscopy of comets and asteroids.

- New discovery potential. PRIMA is designed to maximize sensitivity and efficiency that will measure the poorly explored far-IR spectral band.

1.3.2.1 PRIMA Telescope, Instrument, and Sensitivities

PRIMA's telescope will be a 2.0-m all-aluminum on-axis telescope cooled to 4.5 K. Measurments to achieve the science goals listed above will be made possible by two different instruments, PRIMAger, the PRIMA imaging instrument, and the Far-IR Enhanced Survey Spectrometer (FIRESS). PRIMAger will cover 7 different wavebands. It will provide hyperspectral imaging for the first two bands covering wavelengths from 25-80 μm using a total of 12 continuous LVFs with R=10. At longer wavelengths there will be four polarization-sensitive bands centered at 96, 126, 172, and 235 μm using four broadband filters with R=4. FIRESS will operate between 24 μm to 240 μm. It will consist of two spectrometers one for low spectral resolution mode and the other for high spectral resolution mode. The low resolution mode will have an R$\sim$130 across the entire wavelength range. The high resolution mode will have a tunable spectral resolution with a max R=17,0000 at 24 μm and R=4,400 at 112 μm.

PRIMA's sensitivity requirements will be limited by photon noise from the emission of astronomical sources such as zodiacal light, galactic dust emission, and the cosmic microwave background. Due to this PRIMA requires detectors with a low sensitivity and NEPs on the order of 2.5×10^{-19} W/$\sqrt{\text{Hz}}$. These sensitivities will be met by utilizing arrays of lens-coupled KIDs. I will describe in detail the design of PRIMA KIDs and the characterization of a 25 μm prototype KID array in Ch. 7.

1.4 Thesis Organization

This thesis is organized as follows: In Ch. 2 I will give a brief overview of KIDs. I will discuss the superconducting phenomena that makes it possible to use them as detectors, their detection method, and discuss their demonstration in different observatories. Then I will present the physics governing KIDs and present two models for the response of KIDs in the case of thermally generated quasiparticles and optically generated quasiparticles. This section presents a new responsivity model for optically generated quasiparticles that was developed with the help of Steven Hailey-Dunsheath (Model 2 in Sec. 3.2.2). I will also present a sensitivity model for the theoretical NEPs of KIDs and an iterator I developed to predict the theoretical NEPs. In Ch. 4 I discuss the KID readout methods used to gather data and analysis techniques. In Ch. 5 I present the design for a BEGINS KIDs prototype array, the optical coupling scheme, and the experimental set up for optical measurements. I also discuss the results of dark measurements and optical measurements to characterize the array. Dark measurements were performed at JPL by Byeong Ho Eom and Peter day and I performed optical measurements and data analysis. In Ch. 6 I present the Galaxy Evolution Probe (GEP) which was a predecessor to PRIMA that would have observed down to 10 μm. I discuss the design and dark measurements of a KID array designed for detection at 10 μm. I performed electromagnetic simulations to determine the absorption of the KID inductor. Dark measurements were performed at JPL and I performed the data analysis. In Ch. 7 I present the design for a PRIMA KIDs prototype array and the optical coupling scheme. I also discuss the results of dark measurements and optical measurements to characterize the array. The analysis for the characterization of this array was made with joint efforts between CalTech, JPL, and GSFC. Optical measurements were performed at JPL and I performed the data analysis. Dark measurements and their data analysis was performed at Caltech. In Ch. 8 I introduce the type of bandpass filter used for the LVF. I present how I modeled the filters through electromagnetic simulations and another model I developed using transmission line theory. I also discuss the results of transmission measurements made on a 44 μm bandpass filter and a BEGINS prototype LVF. Finally in Ch. 9 I summarize the research presented in this thesis and discuss the future work.

Chapter 2

Kinetic Inductance Detectors Concept & Background

Cryogenic detectors are used to detect elementary particles such as photons. They operate at temperatures near absolute zero in order to minimize thermal noise. They can also be fabricated into large arrays which provide a larger field of view and faster mapping speed. However, fabricating large arrays and the readout scheme for a large number of detectors can be challenging. For example, transition edge sensors (TESs) are a form of cryogenic detector which have been used for cosmic microwave background detectors for over 15 years, but due to their many-layered fabrication process and complex multiplexed readout they are costly to implement in large arrays [64]. KIDs are a form of cryogenic superconductor detector that overcome these challenges because they are easy to multiplex into large arrays and offer equal or better sensitivity than other cryogenic detectors [64]. They can detect a range of wavelengths and are very popular in submillimeter (submm) and millimeter (mm) astronomy. The concept of KIDs was first proposed by Jonas Zmuidzinas et al. at the *9th Low Temperature Detectors Workshop* [109] and their proof-of-concept with experimental measurements was first published in *Nature* by Peter Day et al.[20]

In this chapter I will give a brief introduction to KIDs. I will discuss superconductivity and kinetic inductance, the detection concept of KIDs, various KID designs, and successful demonstrations of KIDs in observational astronomy.

2.1 Superconductivity & Kinetic Inductance

Normally electrons behave as free particles in metals and repel each other. At temperatures near absolute zero the thermal vibrations of the lattice decrease making it easier for electrons to flow through the metal. Metals that exhibit superconductivity have zero electrical resistance when cooled below their critical temperature, T_c. This phenomenon can be explained through the electron-phonon interaction. At temperatures below T_c the electrons attract the positive ions that make up the lattice of the metal. The attraction causes the ions to move towards the electron and increases the positive charge density in the vicinity which then attracts another electron. The displaced ions allow the electrons to overcome their repulsion and pair up with a binding energy of $2\Delta = 3.52k_BT_c$, where Δ is the superconducting energy gap [56]. This electron pair is called a Cooper pair. While there is nearly zero electrical resistance for direct current in superconductors, there exists a non-zero impedance for alternating current. The superconductor will have a complex surface impedance expressed as

$$Z_s = R_s + j\omega L_s, \tag{2.1}$$

where R_s is the surface resistance, ω is the angular frequency, and L_s is the inductance. At temperatures much lower than T_c the surface impedance becomes almost purely inductive. The surface inductance contributes a kinetic inductance L_{ki} which arises from the inertia of the Cooper pairs in addition to the magnetic inductance L_m.

The kinetic inductance effect occurs when an alternating current is applied to superconductors and the Cooper pairs resist the change of motion. In order for them to change the direction of the effective current flow, kinetic energy is extracted from the Cooper pairs when the alternating current changes sign. This results in a dissipation that is refereed to as kinetic inductance. An expression for L_{ki} can be derived by equating the kinetic energy of the Cooper pairs in a material to the inductive energy of the circuit and is given by

$$L_{ki} = \frac{m_c}{nA^2q^2}, \tag{2.2}$$

where m_c is the mass of the Cooper pairs, n is the density of the Cooper pairs (number per unit volume), A is the cross-sectional area of the superconducting material, and q is the Cooper pair charge [7]. This conceptually and simply explains how kinetic inductance arises in a superconducting material. Sec. 3.1 formally introduces the Mattis-Bardeen theory which describes the response of a superconductor to an applied AC electromagnetic field [69]. It can be used to determine the relationship between the quasiparticle density of a superconducting thin film and its surface impedance.

2.2 KID Detection Method

KIDs utilize the AC properties of superconductors to detect photons. When photons with energy greater than the gap energy of the superconductor ($h\nu > 2\Delta$) are absorbed into the superconductor they can break apart one or more Cooper pairs (Fig. 2.1 Top Left). When the Cooper pairs break apart they create excess quasiparticles (two individual electrons) which increases the kinetic inductance. The magnetic inductance stays the same, since it is defined by the geometry of the superconducting material. This leads to an overall change in the surface impedance of the superconductor. After a time τ_{qp} the quasiparticles recombine into Cooper pairs and the surface inductance returns to its original state. By placing the superconducting material in a resonant circuit the changes in the surface impedance can be detected (Fig. 2.1 Bottom Left). Therefore, KIDs are superconducting micro-resonators with resonant frequency $f_r = \frac{1}{2\pi\sqrt{LC}}$, where L is the total inductance of the resonator and C is the capacitance.

KIDs are made by depositing superconducting thin film on a substrate. The microresonator is patterned out of the thin film and capacitively coupled to a transmission line. When the KID is probed with a signal of many frequencies there will be an absorption feature in the transmission readout that corresponds to f_r of the superconducting resonator. When L_{ki} increases from the absorption of photons and creation of quasiparticles f_r shifts to lower frequencies and its quality factor degrades (Fig. 2.1 Top Right). Large arrays of KIDs can easily be constructed by coupling resonators to the same transmission line which can easily be readout with room temperature electronics. They are easy to multiplex, because each KID in the array can be tuned to a specific frequency to map out large frequency domains. This is how KIDs can be used to detect incident radiation from astronomical sources of interest.

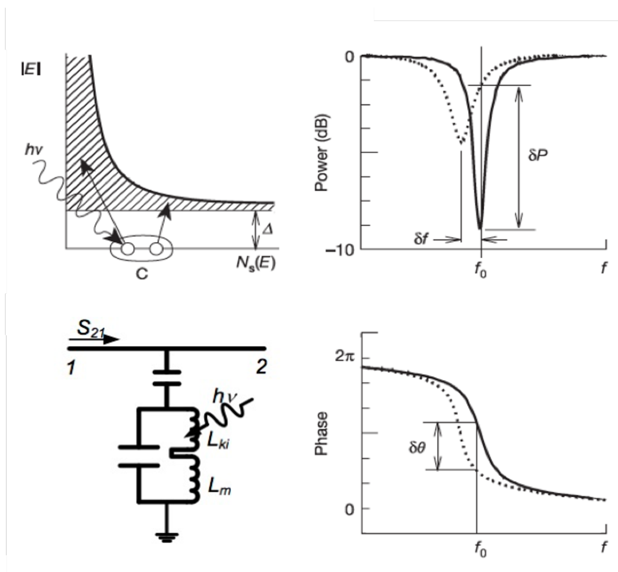

Figure 2.1: An illustration of the detection principle [70, 35]. *Top Left*: When photons with energy greater than the gap energy of the superconductor ($h\nu > 2\Delta$) are absorbed into the superconductor they can break apart one or more Cooper pairs. *Bottom Left*: Equivalent circuit representation of a KID. The upper capacitor is the coupling capacitor to the transmission line. *Top Right*: When the KID is probed with a signal of many frequencies, there will be an absorption feature in the transmission readout that corresponds to f_0 of the superconducting resonator (solid line). When L_{ki} increases from the absorption of photons and creation of quasiparticles f_r shifts to lower frequencies and its quality factor degrades (dashed line). *Bottom Right*: Depicts how the relative phase of the signal transmitted through the line with respect to the input signal changes after the KID absorbs photons.

2.3 KID Designs

KID resonator designs have evolved since their invention as a sensitive photon detector for observational astronomy. The first thorough study of KIDs for photon detection involved quarter-wave co-planar waveguide resonators (CPW KID) [20]. To improve frequency noise in CPW KIDs the interdigitated capacitor (IDC KID) was proposed [81]. To improve coupling of radiation to the resonator the lumped element resonator (LEKID) was proposed [27, 57]. The proceeding subsections will go further into detail on CPW KIDs, IDC KIDs, and LEKIDs.

2.3.1 CPW KIDs

Quarter-wave CPW resonators were an attractive design because they have a simple layout. Coupling to the readout transmission line is easy to accomplish with an elbow coupler (Fig. 2.2 Left). The length of the resonator coupler (L_c) and distance from the transmissions feedline determine the coupling strength to the transmission feedline [93]. An antenna is used to absorb incoming radiation which is guided through a superconducting micro-strip to the center strip of the quarter-wave resonator, which allows detection of radiation (Fig. 2.2 Right) [70]. This detection concept was implemented in DemoCam a sub-millimeter demonstration camera which took maps of Jupiter, Saturn, and G34.3 at the CSO. The device consisted of 32 CPW resonators with frequencies ranging from 6.5-6.81 GHz with a gap of 10 MHz between any two consecutive resonators [57, 71]. In DemoCam and previous studies CPW KIDs showed an unexplained excess frequency noise that was not due to photon noise or quasiparticle recombination [20, 57, 70]. It was discovered that the excess frequency noise came from two level system (TLS) noise[81]. TLS noise is discussed in further detail in Sec. 3.3.4.

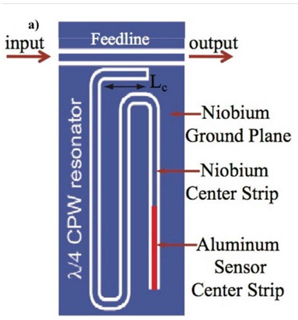

Figure 2.2: *Left*: Quarter-wave CPW resonator [57]. *Right*: The antenna absorbs radiation that gets transmitted through a superconducting micro-strip. The micro-strip has gap energy higher than the energy of the photons absorbed so no Cooper pairs will break. It is over laid on a low energy gap superconducting CPW, where the photons absorbed now have high enough energy to break apart the Cooper pairs [70].

2.3.2 IDC KIDs

IDC KIDs were studied to show that the TLS noise found in CPW KIDs was generated in the capacitive portion (elbow coupler) of the resonator [81]. The initial design was a combination of a lumped-element and quarter-wave CPW resonator. The inductive portion consist of a CPW but instead of an elbow coupler to the feedline there is an interdigitated capacitor (Fig. 2.3) [93]. Noroozian et al. showed that by incorporating an IDC, the TLS noise decreased by a factor of ∼29 [81]. The decrease in noise made IDC KIDs a promising alternative. A drawback to IDCs is they increase the pixel size of the KID and take up most of the focal plane area of an instrument in order to keep the IDCs within the MHz to low GHz range for readout electronics. This limits the number of pixels on an instrument which limits its resolution. In Sec. 5.1 we introduce a KID design with a parallel plate capacitor as an alternative that allows for smaller pixels.

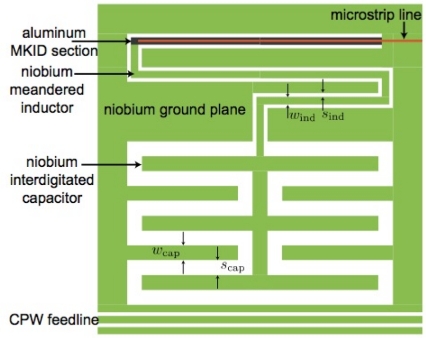

Figure 2.3: Interdigitated capacitor (IDC) KID[93].

2.3.3 LEKIDs

LEKIDs were first purposed by Simon Doyle in 2008 to create a sensitive KID for shorter wavelengths [27]. They consist of an inductive meander in series with a capacitor that is coupled to a feedline (Fig. 2.4 Left) [28]. The benefit of this design is the inductive portion of the resonator can be used as a radiation absorber that is matched to free-space. This approach eliminates the need for an antenna to couple radiation to the resonator. Radiation can be coupled to the inductor by using a horn-antenna or microlens to back-illuminate the inductor through the substrate (Fig. 2.4 Right) [72].

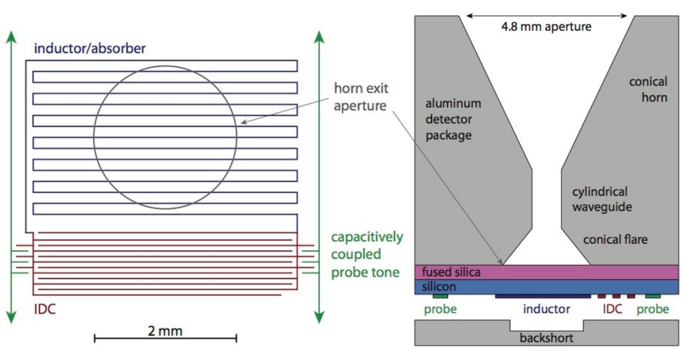

Figure 2.4: *Left*: A single LEKID with the inductive meander as the direct absorber, coupled to a transmission line[28]. *Right*: Cross-sectional view showing how horn-antenna directs radiation towards inductor [72].

2.4 Demonstration of KIDs in Observational Astronomy

KIDs have already been demonstrated in observatories. DemoCam successfully used KIDs to image Jupiter, Saturn, and G3.3 at the Caltech Submillimeter Observatory (CSO) [57]. In 2010, The N´eel IRAM KID Array (NIKA) at the 30-meter Institute for Millimetric Radio Astronomy (IRAM) telescope, produced images of Mars, quasar 3C345, radio star MWC349, and galaxy M19 [76]. In 2013, The Multiwavelength Submillimeter Kinetic Inductance Camera (MUSIC) at the CSO produced images of molecular cloud W51 in 4 different bands (Fig. 2.5) [92].

More recent observatories utilizing KIDs as their detector technology are OLIMPO[1] , the Subaru Telescope, the Balloon-Borne Large-Aperture Sub-millimeter Telescope-The Next Generation (BLAST-TNG)[2] , and the Large Millimeter Telescope (LMT). OLIMPO's instrument has four arrays of KIDs working in the 150, 200, 350, 480 GHz bands to measure the spectrum of the Sunyaev–Zel'dovich effect for a number of galaxy clusters [82]. BLAST-TNG is the first suborbital balloon to demonstrate KIDs. It's instrument has three KID arrays sensitive to both polarizations for detection of 250, 350, and 500 μm wavelengths [63]. The LMT will use the TolTECH camera to study the polarization of the cosmic microwave background (CMB). TolTECH consist of arrays of KIDs for three different bands centered at 2 mm, 1.4 mm, and 1.1 mm[3] . Finally, another example is the the MKID Exoplanet Camera (MEC) located at the Subaru Telescope which was designed to produce high contrast imaging in the near-IR band to find and characterize exoplanets. MEC has the largest superconducting detector array in the world with 20,160 KIDs. Fig. 2.6 shows an image of the five star system Theta^1 Orionis B taken by MEC in 2019 [102]. KIDs are an emerging detector technology that have shown to successfully detect astronomical sources. BEGINS and PRIMA have the potential to demonstrate their functionality in sub-orbital and orbital observatories for mid- to far-IR astronomy.

[1] `https://olimpo.roma1.infn.it/index.html`
[2] `https://sites.northwestern.edu/blast/`
[3] `http://toltec.astro.umass.edu/about.php`

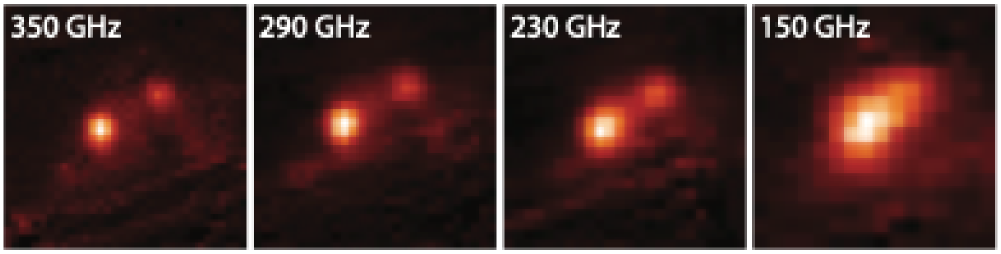

Figure 2.5: Image of W51 taken at 4 different band frequencies with KIDs by MUSIC [92].

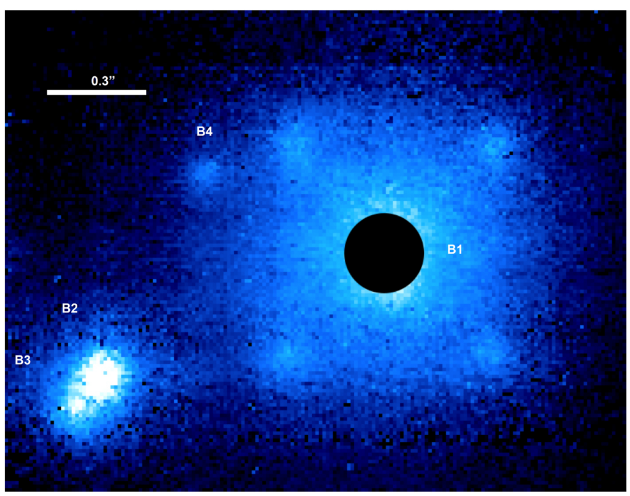

Figure 2.6: Image of Theta^1 Orionis B taken by MEC at the Subaru Telescope in 2019 with KIDs.[102].

Chapter 3

KID Theory: Response & Sensitivity Models

In this chapter I present the physics that governs the behavior of KIDs. The theories discussed allows us to model the response of KIDs under two different conditions. We can model their dark response to small changes in bath temperature which allows us to estimate T_c and the kinetic inductance fraction of the superconducting material. We can also model their response to an optical load to determine the responsivity of the KIDs. The higher the responsivity the more sensitive the KID. Finally, I will also present a sensitivity model which can be used to predict the NEPs of KIDs due to different noise sources.

3.1 Mattis-Bardeen Theory and Estimating T_c and α

Two important material properties of KIDs are their critical temperature, T_c, and their kinetic inductance fraction, α. In this section I will describe how the Mattis-Bardeen theory can be used to estimate T_c and α by relating the complex conductivity of a superconductor to its surface impedance. The Mattis-Bardeen theory, developed in 1958, describes the response of a superconductor to an applied AC electromagnetic field [69]. It can be used to determine the relationship between the quasiparticle density of a superconducting thin film and its surface impedance. To derive this relationship we must first introduce the complex conductivity of a superconductor,

$$\sigma = \sigma_1 - j\sigma_2, \tag{3.1}$$

where σ_1 is the real part of the conductivity (the inverse resistance) and σ_2 is the imaginary part of the conductivity (the inverse reactance). Using the Mattis-Bardeen theory both terms can be expressed relative to the normal state conductivity, σ_n by the following integrals [35, 70],

$$\frac{\sigma_1}{\sigma_n} = \frac{2}{\hbar\omega}\int_{\Delta-\hbar\omega}^{\infty} \frac{[f(E) - f(E+\hbar\omega)](E^2+\Delta^2+\hbar\omega E)}{\sqrt{(E^2-\Delta^2)[(E+\hbar\omega)^2-\Delta^2]}}dE \tag{3.2}$$

$$\frac{\sigma_2}{\sigma_n} = \frac{1}{\hbar\omega}\int_{\Delta-\hbar\omega}^{\Delta} \frac{[1 - 2f(E+\hbar\omega)](E^2+\Delta^2+\hbar\omega E)}{\sqrt{(\Delta^2-E^2)[(E+\hbar\omega)^2-\Delta^2]}}dE. \tag{3.3}$$

Where Δ in the non-zero temperature energy gap and $f(E) = \frac{1}{e^{E/k_BT}+1}$ is Fermi-Dirac distribution function which describes the energy distribution of quasiparticles at thermal equilibrium.

Next, the quasiparticle density in the superconductor must be derived by integrating over the product of the density of excited states in a superconductor, $N_s(E) = \frac{N_0 E}{\sqrt{E^2-\Delta^2}}$, and the Fermi-Dirac distribution. Therefore the quasiparticle density is determined by

$$n_{qp} = 4N_0\int_{\Delta}^{\infty} \frac{Ef(E)}{\sqrt{E^2-\Delta^2}}dE, \tag{3.4}$$

where N_0 is the single-spin density of electron states at the Fermi energy level.

The last equation required is the integral to relate the band gap energy at $T < T_c$ to the band gap at $T = 0$ where $\Delta_0 = \Delta(T=0)$ [94]

$$\frac{\Delta_0 - \Delta}{\Delta_0} = 2\int_{\Delta}^{\infty} \frac{f(E)}{\sqrt{E^2-\Delta^2}}dE. \tag{3.5}$$

Since we will be working in the limit where $k_BT \ll \Delta$, $\hbar\omega \ll \Delta$, and $e^{-E/k_BT} \ll 1$ the integrals in Eq. 3.2, 3.3, 3.4, and 3.5 can be simplified to the following expressions:

$$\frac{\sigma_1}{\sigma_n} = \frac{4\Delta}{\hbar\omega}e^{-\Delta/k_BT}\sinh(\xi_0)K_0(\xi_0) \tag{3.6}$$

$$\frac{\sigma_2}{\sigma_n} = \frac{\pi\Delta}{\hbar\omega}[1 - 2e^{-\Delta/k_BT}e^{-\xi_0}I_0(\xi_0)] \tag{3.7}$$

$$n_{qp} = 2N_0\sqrt{2\pi k_b T\Delta}e^{-\Delta/k_B T} \tag{3.8}$$

$$\frac{\Delta}{\Delta_0} = 1 - \sqrt{\frac{2\pi k_B T}{\Delta}}e^{-\Delta/k_B T}. \tag{3.9}$$

Where K_0 and I_0 are the zeroth order Bessel functions of the first and second kind, respectively, $\xi_0 = \frac{\hbar\omega}{2k_B T}$, and T is the temperature of the detectors. These equations can be used to derive the complex conductivity for two different cases. The first being a temperature dependent case, where the KIDs are tested in a dark environment and the bath temperature is increased from around 50 mK to 600 mK. The second being a quasiparticle dependant case, where the detectors are kept at a bath temperature around 150-300 mK and optically loaded creating optically generated quasiparticles. In the second case, we expect the number of optically generated quasiparticles to be significantly larger than the thermally generated quasiparticles. In case 1, Eq. 3.6 and 3.7 can be rewritten by substituting Eq. 3.9 in for Δ and taking the lowest order term, then setting $\Delta = \Delta_0$ since we are interested in characterizing the KIDs at $T \ll T_c$. This provides the following expressions for the complex conductivity and quasiparticle density as a function of temperature [38, 94]:

$$\frac{\sigma_1(T)}{\sigma_n} = \frac{4\Delta_0}{\hbar\omega}e^{-\Delta_0/k_B T}\sinh(\xi_0)K_0(\xi_0), \tag{3.10}$$

$$\frac{\sigma_2(T)}{\sigma_n} = \frac{\pi\Delta_0}{\hbar\omega}[1 - \sqrt{\frac{2\pi k_b T}{\Delta_0}}e^{-\Delta_0/k_B T} - 2e^{\Delta_0/k_B T}e^{-\xi_0}I_0(\xi_0)], \tag{3.11}$$

$$n_{th} = 2N_0\sqrt{2\pi k_b T\Delta_0}e^{-\Delta_0/k_B T}. \tag{3.12}$$

In case 2, Eq. 3.6 and 3.7 can be rewritten in terms of n_{qp} (Eq. 3.8) where again $\Delta = \Delta_0$. This yields the following equations

$$\frac{\sigma_1(T, n_{qp})}{\sigma_n} = \frac{1}{N_0\hbar\omega}\sqrt{\frac{2\Delta_0}{\pi k_B T}}\sinh(\xi_0)K_0(\xi_0)n_{qp} \tag{3.13}$$

$$\frac{\sigma_2(T, n_{qp})}{\sigma_n} = \frac{\pi\Delta_0}{\hbar\omega} - \frac{\pi}{2N_0\hbar\omega}[1 + \sqrt{\frac{2\Delta_0}{\pi k_B T}} e^{-\xi_0} I_0(\xi_0)] n_{qp}. \tag{3.14}$$

From Eq. 3.13 and 3.13 we also see that the quasiparticle density is proportional to σ_1 and $\delta\sigma_2 = \sigma_2 - \sigma_2(T = 0)$. If we consider small perturbations in σ_1 and σ_2, we can write the following relations [80]

$$\frac{\delta\sigma_1}{\sigma_1} = \frac{\delta n_{qp}}{n_{qp}} \tag{3.15}$$

$$\frac{\delta\sigma_2}{\sigma_2 - \sigma_2(T = 0)} = \frac{\delta n_{qp}}{n_{qp}} \tag{3.16}$$

The creation of thermally and optically generated quasipartcles can be detected by changes in the complex conductivity. The complex conductivity can be related to the surface impedance of the detector which allows us to develop a model that can be tested against experimental data. This is further explained in the following sections.

3.1.1 Complex Conductivity and Surface Impedance

In most cases we are not able to directly measure the complex conductivity of a thin film. However the complex surface impedance, Z_s, can be probed and measured. In the case of thin films such as KIDs, a relationship can be made between the complex conductivity and the surface impedance. In the thin film limit, where the film thickness t, is much smaller than the effective penetration depth λ_{eff}, and on the order of the electron mean free path l, we have the following relationship[80]

$$Z_s = R_s + j\omega L_s = \frac{1}{(\sigma_1 - j\sigma_2)t}, \tag{3.17}$$

where R_s is the sheet resistance in units of Ω/squ and L_s is the surface inductance in units of H/squ. The penetration depth is defined as the depth at which electromagnetic radiation penetrates a material and falls to 1/e of its original intensity. The electron mean free path is the average distance an electron travels in a medium before experiencing a collision. If we consider a small perturbation in the surface impedance we find the following relationship

$$\frac{\delta Z_s}{Z_s} = -\frac{\delta\sigma}{\sigma}. \tag{3.18}$$

Since we test KIDs at $T \ll T_c$, we make an approximation that $T = 0$. At $T = 0$, for superconductors $R_s = 0$ and $\sigma_1 = 0$. Therefore, $Z_s(T = 0) = j\omega L_{s,0}$ and $\sigma(T = 0) = -j\sigma_{2,0}$. The small perturbation can now be re-written as

$$\frac{\delta R_s + j\omega\delta L_s}{j\omega L_{s,0}} = -\frac{\delta\sigma_1 - j\sigma_2}{\sigma_{2,0}}. \tag{3.19}$$

Now the imaginary and real parts can be separated to yield,

$$\frac{\delta R_s}{j\omega L_{s,0}} = \frac{\delta\sigma_1}{\sigma_{2,0}} \tag{3.20}$$

$$\frac{\delta L_s}{L_{s,0}} = -\frac{\delta\sigma_2}{\sigma_{2,0}}. \tag{3.21}$$

Using Eq. 3.15 and 3.16 we can rewrite the equations above in terms of perturbation in the quasiparticle density,

$$\frac{\delta R_s}{j\omega L_{s,0}} = \frac{S_1(\omega)}{2N_0\Delta_0}\delta n_{qp} \tag{3.22}$$

$$\frac{\delta L_s}{L_{s,0}} = -\frac{S_2(\omega)}{2N_0\Delta_0}\delta n_{qp} \tag{3.23}$$

where $S_1(\omega)$ and $S_2(\omega)$ are the small perturbations in the real and imaginary parts of the conductivity in the limit that $\hbar\omega$, $k_BT << \Delta_0$ [81, 108]. In the literature they are derived to be [81, 108],

$$S_1(\omega) = \frac{2}{\pi}\sqrt{\frac{2\Delta_0}{\pi k_B T}}\sinh(\xi_0)K_0(\xi_0) \tag{3.24}$$

$$S_2(\omega) = 1 + \sqrt{\frac{2\Delta_0}{\pi k_B T}} e^{-\xi_0} I_0(\xi_0). \tag{3.25}$$

The derived relations are important because them we can relate the surface impedance to measurable quantities such as the resonant frequency f_r and internal quality factor Q_i of the resonator. The impedance of the KID resonant circuit is given by

$$Z = R_s + j\omega L_s + \frac{1}{j\omega C}. \tag{3.26}$$

Where R is the resistance, C is the capacitance, and L is the inductance. The resistance arises from the generation of quasiparticles in the thin film. The capacitance is set by the geometry of capacitive portion of the resonator. The inductance is made up of both the magnetic inductance L_m which depends on the inductor geometry and the surface inductance which is due to the kinetic inductance L_{ki} of the Cooper pairs. The inductance can then be written as $L_s = L_m + L_{ki}$. From this equation we can derive the kinetic inductance fraction α, which is a term used to characterize KIDs,

$$\alpha = \frac{L_{ki}}{L_s} = \frac{L_{ki}}{L_m + L_{ki}}. \tag{3.27}$$

The resonant frequency and internal quality factor of the resonator are described by the following expressions

$$f_r = \frac{1}{2\pi\sqrt{L_s C}} \tag{3.28}$$

$$\frac{1}{Q_i} = \frac{R_s}{\omega L_s}. \tag{3.29}$$

If we now consider a small perturbation in the resistance δR_s and the kinetic inductance δL_{ki} due to changes in the quasiparticle density we will see a fractional frequency shift δx given by

$$\delta x = \frac{\delta f_r}{f_r} = -\frac{1}{2}\frac{\delta L_{ki}}{L_s} = -\frac{\alpha}{2}\frac{\delta L_{ki}}{L_{ki}} \tag{3.30}$$

and a change in the internal quality factor given by

$$\delta\frac{1}{Qi} = \frac{\delta R_s}{\omega L_s} = \alpha\frac{\delta R_s}{\omega L_{ki}}. \tag{3.31}$$

Now that we have a relationship between the complex conductivity, surface impedance and the measurable quantities f_r and Q_i we can introduce a method to make measurements to estimate α, T_c and the responsivity of the KIDs. These parameters are necessary for characterizing the KIDs and to theoretically predict their sensitivity.

3.1.2 Estimating T_c and α

To estimate T_c and α of the KIDs we measure their resonance fractional frequency shift as a function of bath temperature in a dark environment. They are measured below $T_c/4$ which is usually a few hundred mK. At these temperatures the best noise performance is achieved. As the bath temperature increases there is an increases in the thermally generated quasiparticles as a function of temperature. This increases the kinetic inductance which decreases the resonant frequency and increases the surface resistance which decreases the internal quality. We can take Eq. 3.21 and 3.30 to derive the following relationship between the resonant frequency and the complex conductivity

$$\delta x = \frac{\delta f_r}{f_r} = -\frac{\alpha}{2}\frac{\delta\sigma_{2,0}}{\sigma_{2,0}}. \tag{3.32}$$

Which is then rewritten as

$$\frac{f_r(T) - f_r(T=0)}{f_r(T=0)} = -\frac{\alpha}{2}\frac{\sigma_2(T) - \sigma_2(T=0)}{\sigma_2(T=0)}, \tag{3.33}$$

where $\sigma_2(T)$ is the expression in Eq. 3.11. The fractional frequency shift can then be fit to the model with α and Δ_0 as the estimate parameters from which T_c can be estimated using the relation $\Delta_0 = 1.764 k_B T_c$. In these measurements $T = 0$ actually denotes the measurement at the lowest temperature we are able to achieve.

3.2 The Responsivity of KIDs

We are interested in the KIDs' response when exposed to an optical load, P_{abs}. In astronomy this would be caused by the optical load from an astronomical source through an optical system, with efficiency η_{opt}. When KIDs are exposed to an optical load the absorbed optical power causes fluctuations in the quasiparticle density, which as explained in the section above can be experimentally detected by changes in the resonant frequency and internal quality factor of the KID. The responsivity of a KID is defined by perturbations in its resonant frequency and internal quality factor due to perturbations in absorbed optical power. I will present the theoretical model used to predict the responsivity of KIDs and how we measure the responsivity in lab using a cryogenic blackbody.

3.2.1 Quasiparticle Lifetime & Generation and Recombination Rates

There are three forms of quasiparticle generation: thermal, optical and readout power. At finite temperatures Cooper pairs can be thermally excited into quasiparticles, referred to as thermal generation. In this process a Cooper pair is broken apart by a lattice vibration known as a phonon with energy greater than the binding energy of the Cooper pair, resulting in the generation of two quasiparticles. A Cooper pair can also broken apart when exposed to a photon with energy greater than its binding energy, $h\nu > 2\Delta_0$, this is referred to as optical generation. The last form is the breaking of a Cooper pair caused by the absorption of readout power P_a with energy greater than the binding energy. Another important process is the recombination of quasiparticles. This is when two quasiparticles recombine into a Cooper pair and emit a phonon. The time it takes for the particles to recombine is known as the quasiparticle lifetime, τ_{qp}. The generation and recombination of quasiparticles can be described by the following differential equation

$$\frac{dn_{qp}}{dt} = \Gamma_{th} + \Gamma_{opt} + \Gamma_a - \Gamma_{rec}. \tag{3.34}$$

Where Γ_{opt} is the generation rate due to absorption of optical photons, Γ_a is the generation rate due to the absorption of readout photons, and Γ_{th} is the generation rate due to the absorption of thermal phonons.

The generation of quasiparticles by absorbed optical power is described by

$$\Gamma_{opt} = \frac{\eta_{pb} P_{abs}}{\Delta_0}. \tag{3.35}$$

Where η_{pb} is the efficiency at which absorbed optical power generates quasiparticles. The generation rate due to absorbed readout power is described by the expression

$$\Gamma_a = \frac{\eta_a \chi_{qp} P_a}{\Delta_o}. \tag{3.36}$$

Where η_a is the efficiency at which absorbed readout power generates quasiparticles, $\chi_{qp} = \frac{Q_i}{Q_{qp}} \leq 1$ is the fraction of internal dissipation due to the quasiparticles. Where $P_a = \frac{\chi_c \chi_g P_g}{2}$, is the absorbed readout power [108]. The absorbed readout power depends on χ_c, the coupling efficiency, and χ_g, the generator detuning efficiency. The generator is tuned when generator frequency is equal to the resonance frequency resulting in $\chi_g = 1$. Finally, the thermal generation rate is

$$\Gamma_{th} = \frac{N_{th}}{2}\left(\frac{1}{\tau_{max}} + \frac{1}{\tau_{th}}\right). \tag{3.37}$$

where $N_{th} = n_{th} V$ is the number of thermally excited quasiparticles in the active volume. τ_{max} is the experimentally observed maximum lifetime [108]. τ_{th} is the lifetime when only thermal quasiparticles are present.

The recombination rate is described by the expression

$$\Gamma_{rec} = \frac{N_{qp}}{2}(\frac{1}{\tau_{max}} + \frac{1}{\tau_{qp}}). \tag{3.38}$$

Where $N_{qp} = n_{qp} V$ is the total number of quasiparticles in the active volume and τ_{qp} is the quasiparticle lifetime. The quasiparticle lifetimes τ_{th} and τ_{qp} have shown to be well described by the following relations:

$$\tau_{qp} = \frac{\tau_{max}}{1 + \frac{n_{qp}}{n^*}}, \tag{3.39}$$

$$\tau_{th} = \frac{\tau_{max}}{1 + \frac{n_{th}}{n^*}}. \tag{3.40}$$

Where n^* is the crossover density at which the observed quasiparticle lifetime saturates to τ_{max} [108]. In the high n_{qp} limit n^* can be theoretically determined using the following equation

$$n^* = \frac{N_0 \tau_0 (k_B T_c)^3}{2\Delta_0^2 \tau_{max}}, \tag{3.41}$$

where τ_0 is the electron-phonon interaction time[42]. Solving for n_{qp} from Eq 3.34 at steady state we get,

$$n_{qp} = \sqrt{(n_{th} + n^*)^2 + 2(\Gamma_{opt} + \Gamma_a)\tau_{max} n^*/V} - n^*. \tag{3.42}$$

Therefore a perturbation in the quasiparticle population δN_{qp} due to a perturbation in the absorbed power δP_{abs} is found by the following derivation [80]

$$\delta N_{qp} = \frac{\partial N_{qp}}{\partial P_{abs}} \delta P_{abs} = \frac{\eta_{pb} \tau_{qp}}{\Delta_0} \delta P_{abs}. \tag{3.43}$$

This equation along with Eq. 3.22, 3.23, 3.30 and 3.31 will allow us to derive the responsivity of KIDs, R_x the fractional frequency responsivity and R_{1/Q_i} the loss responsivity as follows,

$$R_x = \frac{\delta x}{\delta P_{abs}} = \frac{\alpha S_2(\omega) \eta_{pb} \tau_{qp}}{4 N_0 \Delta_0^2 V} \tag{3.44}$$

$$R_{1/Q_i} = \frac{\delta Q_i^{-1}}{\delta P_{abs}} = \frac{\alpha S_1(\omega) \eta_{pb} \tau_{qp}}{2 N_0 \Delta_0^2 V}. \tag{3.45}$$

3.2.2 Estimating R_x

In Ch. 5 and 7 it will be important to experimentally estimate R_x to calculate the empirical NEPs of the KIDs. To estimate R_x we measure the resonance fractional frequency shift as a function of absorbed optical power. There are two different models that can be used to fit for and estimate R_x.

Model 1 suggests that the responsivity is constant with absorbed optical power. This model is derived from Eq. 3.44 as follows,

$$\delta x = R_x \delta P_{abs} \Rightarrow x = \int R_x \delta P_{abs} \Rightarrow x = R_x P_{abs} + C. \tag{3.46}$$

This model suggest the the fractional frequency shift changes linearly with absorbed power. The responsivity (R_x) can be found by doing a linear fit to the fractional frequency response as a function of absorbed power.

Model 2[1] suggests that the responsivity changes with absorbed power but is not linear. Model 2 is derived by taking Eq. 3.44 and substituting τ_{qp} with Eq. 3.39. Then substituting n_{qp} in Eq. 3.39 with Eq. 3.42 which simplifies to

$$\frac{\delta x}{\delta P_{abs}} = \frac{\alpha S_2(\omega)\eta_{pb}\tau_{max}}{4N_0\Delta_0^2 V}\left[\left(1+\frac{n_{th}}{n^*}\right)^2 + \frac{2(\Gamma_{opt}+\Gamma_a)\tau_{max}}{n^* V}\right]^{-1/2}. \tag{3.47}$$

Under the assumption that the quasiparticle generation due to absorbed microwave power can be neglected Eq. 3.47 can be rewritten as,

$$\begin{aligned} \frac{\delta x}{\delta P_{abs}} &= \frac{\alpha S_2(\omega)\eta_{pb}\tau_{max}}{4N_0\Delta_0^2 V}\left[\left(1+\frac{n_{th}}{n^*}\right)^2 + \frac{2\eta_{pb}P_{abs}\tau_{max}}{\Delta_0 n^* V}\right]^{-1/2} \\ &= \frac{\alpha S_2(\omega)\eta_{pb}\tau_{max}}{4N_0\Delta_0^2 V}\left(1+\frac{n_{th}}{n^*}\right)^{-1}\left[1+\frac{2\eta_{pb}P_{abs}\tau_{max}}{\Delta_0 n^* V\left(1+\frac{n_{th}}{n^*}\right)^2}\right]^{-1/2} \\ &= \frac{R_{x,0}}{\sqrt{1+\frac{P_{abs}}{P_0}}} \end{aligned} \tag{3.48}$$

[1] Steven Hailey-Dunsheath introduced this model to me and helped me derive it.

where

$$R_{x,0} = \frac{\alpha S_2(\omega)\eta_{pb}\tau_{max}}{4N_0\Delta_0^2 V}\left(1 + \frac{n_{th}}{n^*}\right)^{-1} \tag{3.49}$$

$$P_0 = \frac{\Delta_0 n^* V}{2\eta_{pb}\tau_{max}}\left(1 + \frac{n_{th}}{n^*}\right)^2. \tag{3.50}$$

Now the simplified form of Eq. 3.48 can be integrated to obtain a model for the fractional frequency shift as a function of absorbed power.

$$\delta x = \frac{R_{x,0}}{\sqrt{1 + \frac{P_{abs}}{P_0}}}\delta P_{abs} \Rightarrow x = \int \frac{A}{\sqrt{1 + \frac{P_{abs}}{P_0}}}\delta P_{abs} \tag{3.51}$$

$$x = 2R_{x,0}P_0\sqrt{1 + \frac{P_{abs}}{P_0}} + C, \tag{3.52}$$

where C is a constant that arises from integration, $R_{x,0}$ is the responsivity in the limit that the absorbed optical power goes to zero and P_0 is constant with absorbed optical power. This yields a model with a three parameter fit for $R_{x,0}$, P_0, and C. From Eq. 3.48 we obtain the expression for responsivity,

$$R_x = \frac{R_{x,0}}{\sqrt{1 + \frac{P_{abs}}{P_0}}}. \tag{3.53}$$

The estimated parameters from the fit can be plugged into this equation to obtain R_x as a function of absorbed power. In this model R_x, is not constant because τ_{qp} is expected to change with absorbed power. These two models will be compared in Ch. 5.

3.3 KID Noise Sources & Sensitivity Model

This section presents a kinetic inductance detector (KID) sensitivity model, primarily constructed from Jonas Zmuidzinas's publication, *Superconducting Microresonators: Physics and Applications* [108]. The sensitivity of a KID is quantified by the noise-equivalent-power (NEP), which measures the noise generated by some source. It is defined as the power incident on the detector that gives a signal-to-noise ratio of one over a bandwidth of 1 Hz. Below I will highlight the theoretical NEPs for noise sources due to photon/shot noise from optical power, generation and recombination of quasiparticles, amplifier noise, and two-level-system (TLS) noise. The derivation for each theoretical NEP is presented in [108].

3.3.1 Photon Noise

The radiation power received by the detector is not constant over time due to the random arrival rate of photons. This photon-noise is described by the following NEP

$$NEP_{opt}^2 = 2\eta_{opt} P_{inc} h\nu(1 + n_o), \tag{3.54}$$

where $\hbar$ is Plank's constant, ν is the incident photon frequency, and n_o is the photon occupation number. The first term, $2\eta_{opt} P_{opt} \hbar\nu$, represents the photon shot noise and the second term, $2\eta_{opt} P_{opt} \hbar\nu n_o$, is the Poisson statistics correction due to photon bunching for a single mode [24, 108]. At short wavelengths (optical or near-infrared) the photon counts follow a Poisson distribution. However at longer wavelengths at which $h\nu \ll k_B T$ photons are strongly "bunched" and $n_o \gg 1$ [108].

3.3.2 Generation-Recombination Noise

As mentioned above, a source of noise in KIDs is due to the generation and recombination of quasiparticles. Therefore, these NEPs were derived using the generation rates presented in Sec.3.2. The NEP contribution of quasiparticle generation due to thermal fluctuations is

$$NEP_{therm-gen}^2 = \frac{4\Gamma_{th}\Delta_0^2}{\eta_{pb}^2} = \frac{2N_{th}\Delta_0^2}{\eta_{pb}^2}\left(\frac{1}{\tau_{max}} + \frac{1}{\tau_{th}}\right). \tag{3.55}$$

The NEP contribution of quasiparticle generation due to the absorption of readout photons is

$$NEP_{micro-gen}^2 = \frac{4\Gamma_a\Delta_0^2}{\eta_{pb}^2} = \frac{4\eta_a\chi_{qp}\Delta_0 P_a}{\eta_{pb}^2}. \tag{3.56}$$

Lastly, the NEP contribution due to quasiparticle recombination is

$$NEP_{rec}^2 = \frac{4\Gamma_{rec}\Delta_0^2}{\eta_{pb}^2} = \frac{2N_{qp}\Delta_0^2}{\eta_{pb}^2}\left(\frac{1}{\tau_{max}} + \frac{1}{\tau_{qp}}\right). \tag{3.57}$$

The factors of four in each equation is a combination from a factor of two that takes into account that quasiparticles appear and disappear in pairs, and another factor two that accounts for the noise in positive and negative frequencies (single-sided spectra) [80, 108].

3.3.3 Amplifier Noise

Another source of noise in KIDs is the amplifier noise. In this case the NEP is different for the dissipation ($1/Q_i$) and frequency (x) directions.

$$NEP_{amp,diss}^2 = \left(\frac{4N_{qp}\Delta_0}{\eta_{pb}\chi_c\chi_{qp}\tau_{qp}}\right)^2 \frac{k_B T_a}{P_g}, \tag{3.58}$$

$$NEP_{amp,freq}^2 = \left(\frac{4N_{qp}\Delta_0}{\beta\eta_{pb}\chi_c\chi_{qp}\tau_{qp}}\right)^2 \frac{k_B T_a}{P_g}, \tag{3.59}$$

where T_a is the amplifier temperature and β is the ratio of Eq. 3.25 to Eq. 3.24 [108].

3.3.4 Two Level System (TLS) Noise

Two level system noise arises from the disordered structure of amorphous materials where one atom or a group of atoms can tunnel between two potential energy minima [80]. The atoms have an electric dipole moment which makes them electrically active each time they tunnel. These dipole moments can couple to electric fields, and fluctuate the dielectric constant of the material. Evidence of TLSs have been found in KID noise measurements [80, 36]. For KIDs the material hosting TLSs is the substrate (Si). The electric fields from the capacitor of the KID couples to the dipoles of the TLS. Since the dielectric constant of the material is fluctuating the capacitance is altered which changes the resonant frequency of the KID while the quality factor remains mostly unchanged. Therefore, it is only seen in the frequency domain. Evidence of TLS noise can be detected from the noise power spectral densities (PSDs) and is referred to as S_{TLS} [108]. PSDs are presented and discussed in Sec.4.2. S_{TLS}, is estimated from KID noise measurements and further explained in Sec.5.3.4.

The NEP contribution due to TLS noise is:

$$NEP_{TLS}^2 = \frac{2S_{TLS}}{R_x^2} = 2\left(\frac{4N_0\Delta_0^2 V}{\alpha\eta_{pb}S_2(\omega)\tau_{qp}}\right)^2 S_{TLS} \tag{3.60}$$

As the temperature is increased, TLS noise should decrease and as the driving power increases TLS noise should also decrease, because the two-level systems become saturated in the upper state [108].

3.3.5 Total NEP

The total NEP is found by adding all the contributing NEPs in quadrature. This allows to theoretically predict the NEPs of KIDs and compare it to the empirical NEPs determines from measurements, as will be shown in Ch. 5 and Ch. 7.

$$NEP_{diss}^2 = NEP_{opt}^2 + NEP_{therm-gen}^2 + NEP_{micro-gen}^2 + NEP_{rec}^2 + NEP_{amp,diss}^2 \tag{3.61}$$

$$NEP_{freq}^2 = NEP_{opt}^2 + NEP_{therm-gen}^2 + NEP_{micro-gen}^2 + NEP_{rec}^2 + NEP_{amp,freq}^2 + NEP_{TLS}^2 \tag{3.62}$$

3.4 Sensitivity Code Iterator

In practice the theoretical NEP is usually calculated with the assumption that $\eta_a \ll 1$ meaning quasiparticle generation due to readout photons is negligible or the assumption that $\chi_{qp} = \frac{Q_i}{Q_{qp}} = 1$, meaning that the total internal quality factor of the resonator (Q_i) is completely due to the dissipation from quasiparticles (Q_{qp}). For the former, this means that there is no contribution from $NEP_{micro-gen}$ and that the quasiparticle density in Eq. 3.42 has no dependence on the generation rate due to absorbed readout power, Γ_a. For the latter, however, there may be internal dissipation losses due to other factors which can degrade Q_i. I discovered that if we do account for quasiparticle generation due to readout photons and do not assume $\chi_{qp} = 1$ there arise unknown parameters which make it difficult to predict the total NEP. This issue arises when calculating n_{qp}, which is necessary for calculating NEP_{rec}. In order to calculate n_{qp} you need to calculate Γ_a, which depends on χ_{qp}, which depends on Q_{qp}, which depends on n_{qp} (the unknown parameter to begin with). The relation between Q_{qp} and n_{qp} is shown in the following expression [108]

$$Q_{qp} = \frac{2N_0\Delta_0 V}{\alpha S_1(\omega)N_{qp}}. \tag{3.63}$$

Since $N_{qp} = n_{qp}V$, Q_{qp} depends on n_{qp} which is the parameter we began with. Without Q_{qp} we cannot theoretically calculate n_{qp} and vice versa. A diagram displaying this interdependence is shown in Fig. 3.1. To address this one can create an iterator with a threshold for convergence on one of the parameters being calculated. In the iterator I developed I set a threshold on n_{qp}. I start with an initial guess for n_{qp} from which the iterator solves for Q_{qp} to calculate χ_{qp}. It then calculates Γ_a from χ_{qp}. Then Γ_a is used to calculate n_{qp}. The iterator then checks whether the initial guess for n_{qp} is within 0.1% of the calculated n_{qp}. If it is not a new guess for n_{qp} is generated. The iterator cycles through these steps until the guess for n_{qp} is within 0.1% of the calculated n_{qp}. Once the correct values are found they are used to calculate the theoretical NEPs of the sensitivity model. A diagram displaying the iterative process is shown in Fig. 3.2. This method will be used to calculate the theoretical NEPs discussed in Ch. 5, Ch. 6, and Ch.7.

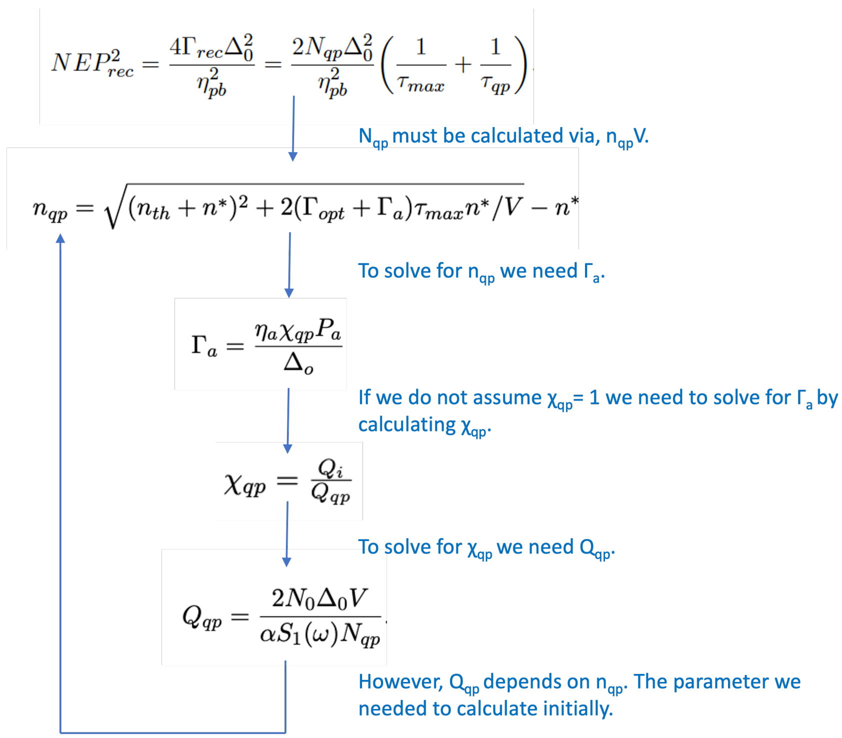

Figure 3.1: A diagram displaying the interdependence of parameters that arises when we do account for quasiparticle generation due to readout photons and do not assume $\chi_{qp} = 1$ to calculate to calculate.

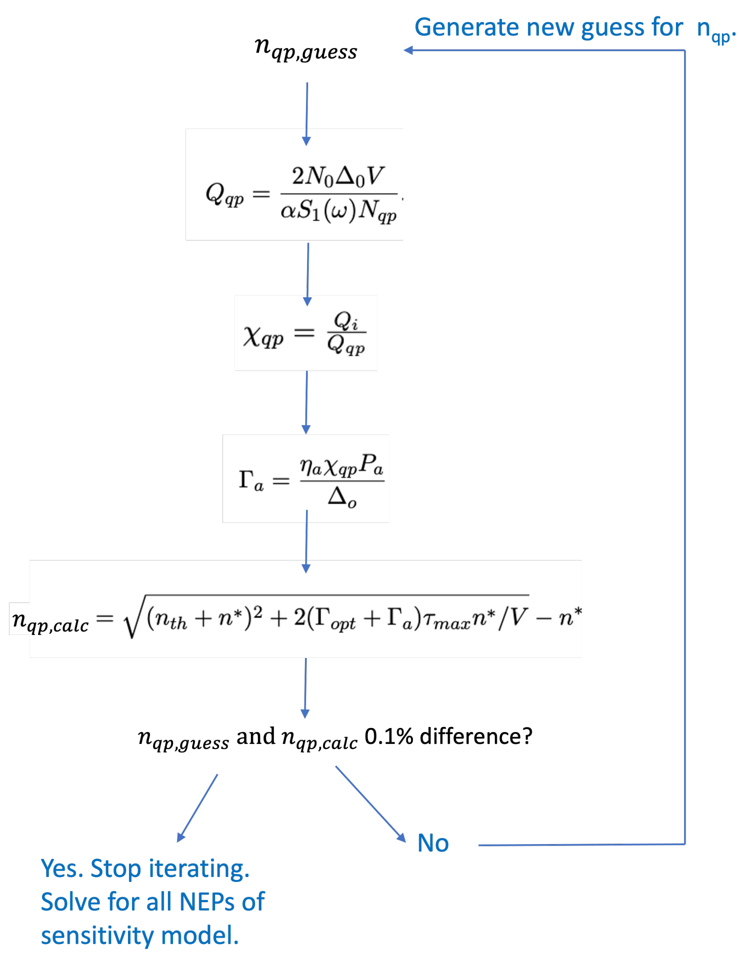

Figure 3.2: A diagram displaying the iterative process to calculate n_{qp} for the sensitivity model.

Chapter 4

Measurement Methods for KID Characterization

In this thesis two different measurement methods are employed to characterize and measure the dark and optical response of KIDs. One method is using a vector network analyzer (VNA). With a VNA we can measure S_{21}, the forward transmission scattering parameter. This measures the power transmitted through the KID and with it we can keep track of changes in the resonant frequency at different bath temperature and optical loads. The other method is single-tone measurements of KIDs for noise analysis.

In this chapter I will present a model used to fit to S_{21} to estimate f_r and the quality factors of the KIDs. This model also fits for other parameters that are further discussed below. I also present how single-tone noise measurements are made, how they are converted to power spectral densities, and how they are used to determine the NEP of a KID. These methods will be used to characterize the prototype KID arrays presented in chapters 5, 6, and 7.

4.1 Scattering Parameter Fit (S_{21}): Estimating f_r and Quality Factors

Fig. 4.1 *Top*, shows an equivalent circuit diagram for the KID resonator and a simple readout schematic [80]. The resonator is represented by an RLC circuit capacitively coupled (C_c) to a feedline [80, 108]. A microwave signal generator transmits many signals through a coaxial cable to the feedline, past the resonator, and is amplified with an amplifier. When the signal is tuned near f_r of the KID, the KID absorbs the energy of the signal at that frequency. This absorption is detected by measuring S_{21}, which is the ratio of the output signal (V_{out}) to the input signal (V_{in}).

$$\frac{V_{out}}{V_{in}} = S_{21}. \tag{4.1}$$

S_{21}, is the complex transmission that represents the scattering parameter for the two-port system. In the complex plane S_{21} follows a circular trajectory as a function of frequency (Fig. 4.1 *Bottom*). The magnitude ($|S_{21}|$) has a Lorentzian profile (ref fig). The transmission through an ideal resonator as a function of frequency is best described by,

$$S_{21} = 1 - \frac{1}{1+2jy}\frac{Q_r}{Q_c}. \tag{4.2}$$

Where Q_r, is the total quality factor of the resonator, Q_c is the coupling quality factor, and $y = Q_r x$. $x = \frac{f_g - f_r}{f_r}$, is the fractional detuning of the readout frequency (f_g) relative to the resonator's resonant frequency (f_r)[80, 35, 108, 94]. Q_c, quantifies the coupling strength of the resonator to the feedline. Another important quality factor not directly introduced is Q_i. Q_i, is the internal quality factor of the resonator. It quantifies all losses in the resonator due to all other processes, such as the resistivity of the superconducting film and the quasiparticle dissipation. Q_i and Q_c add reciprocally,

$$\frac{1}{Q_r} = \frac{1}{Q_c} + \frac{1}{Q_i}. \tag{4.3}$$

Therefore, Q_i can be determined from Q_c and Q_r. Eq. 4.2 represents an ideal linear resonator. However, when the resonator is driven at a higher signal generator power it becomes nonlinear. This is caused by a nonlinear kinetic inductance effect. Another asymmetry is introduced by a mismatch between the input and output transmission line impedance. These will be briefly discussed in the following two sections along with the necessary modifications to Eq. 4.2.

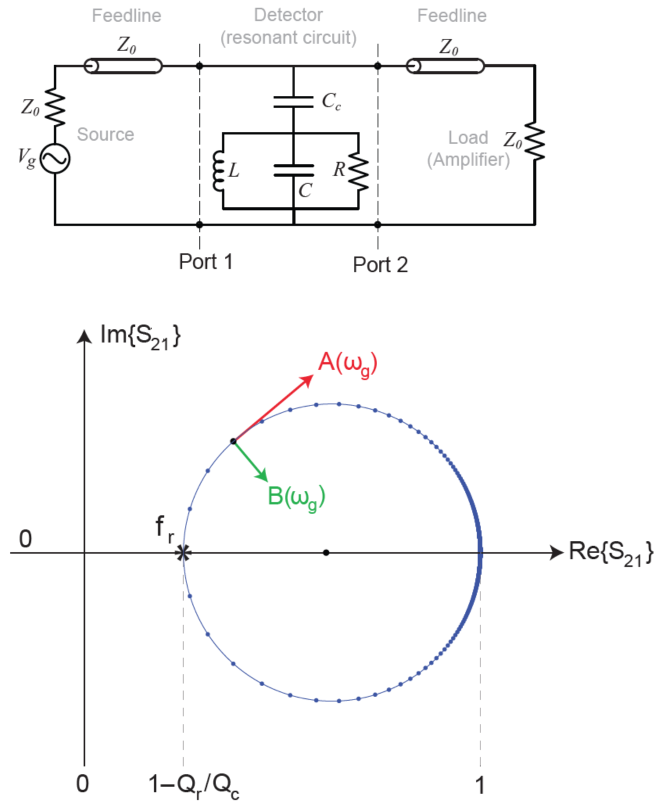

Figure 4.1: *Top*: Equivalent circuit diagram of a superconducting resonator coupled capacitively to a feedline. *Bottom*: Complex transmission, S_{21}, as a function of frequency. f_r, is the resonance frequency. The dots along the circle represent fixed frequency steps. $A(w_g)$ and $B(w_g)$ are the tangent and perpendicular complex vectors of the resonance loop for a fixed generator frequency ($w_g = 2\pi f_g$), respectively. $A(w_g)$ is referred to as the frequency direction, and $B(w_g)$ is referred to as the dissipation direction. Figures from Noroozian Thesis, 2012[80].

4.1.1 Nonlinear Kinetic Inductance

The mechanism behind a KID's nonlinear response is a nonlinear kinetic inductance. In this regime the frequency and/or quality factor depends on the drive power. Fig. 4.1.1 *Left*, shows how the resonator's response becomes nonlinear as the drive power increases. The black line represents a linear resonator. The other lines show how the resonator would become more and more nonlinear as the drive power increases. The derivation that incorporates the nonlinear kinetic inductance into Eq. 4.2 in this section is based on the derivation by Swenson et al. and Siegl's re-derivation

[97, 94]. The kinetic inductance (L_{ki})of a superconducting strip in terms of current is,

$$L_{ki}(I) = L_{ki}(I = 0)(1 + \frac{I^2}{I_*^2} + ...). \tag{4.4}$$

I_*, is a constant that sets the scale of the non-linearity. $L_{ki}(I = 0)$, is the kinetic inductance in the low power, linear limit. Now, let $f_{r,0}$, represent the frequency in the low power limit and $\Delta f_r = f_r - f_{r,0}$ represent the frequency shift due to non-linearity. From Eq.3.30, derived later in the thesis, the following relation is formed

$$\Delta x = \frac{\Delta f_r}{f_{r,0}} = -\frac{\alpha}{2}\frac{\delta L_{ki}}{L} = -\frac{\alpha}{2}\frac{I^2}{I_*^2} = -\frac{E}{E_*}. \tag{4.5}$$

$E = \frac{LI^2}{2}$ is the energy stored in the resonator. $E_* = \frac{LI_*^2}{\alpha}$, is defined as the characteristic energy, related to the non-linearity [97, 108]. This must now be substituted into y of in Eq. 4.2. The fractional detuning from resonance (x) with the fractional frequency shift due to non-linearity is then

$$x = \frac{f_g - f_r}{f_r} \tag{4.6}$$

$$= \frac{f_g - f_{r,0} - \Delta f_r}{f_{r,0} + \Delta f_r} \tag{4.7}$$

$$= \left(\frac{f_g - f_{r,0}}{f_{r,0}} - \frac{\Delta f_r}{f_{r,0}}\right)\left(1 + \frac{\Delta f_r}{f_{r,0}}\right)^{-1} \tag{4.8}$$

$$= (x_0 - \Delta x)(1 - \Delta x) \tag{4.9}$$

$$= x_0 - \Delta x. \tag{4.10}$$

Where x_0, is the detuning in the low power limit and Δx is the nonlinear frequency shift. In the last line only the first order terms are kept, since we are operating where $x_0 \ll 1$ and $\Delta x \ll 1$.

Next, an expression is needed to describe the stored energy in the resonator given a generator drive power (P_g) and frequency. The drive power can either be reflected back to the generator, transmitted past the resonator or absorbed by the resonator. Through conservation of power the absorbed power is then,

$$P_{diss} = P_g[1 - |S_{11}|^2 - |S_{21}|^2]. \tag{4.11}$$

S_{11} is the reflection coefficient and represents the amount of power reflected back to the generator. The reflection coefficient is related to the transmission by $S_{11} = 1 - S_{21}$. Eq. 4.2, is substituted into this relation to get,

$$S_{11} = S_{21} - 1 = -\frac{1}{1 + 2jy}\frac{Q_r}{Q_c} \tag{4.12}$$

Eqs. 4.2 and 4.12 are substituted into Eq. 4.13 to yield,

$$P_{diss} = \frac{2Q_r^2}{Q_i Q_c}\frac{1}{1 + 4y^2}P_g \tag{4.13}$$

The other necessary expression to calculate the stored energy in the resonator given a drive power, is the standard definition for the internal quality factor of the resonator [97, 94],

$$Q_i = \frac{E}{P_{diss}/2\pi f_r} \Rightarrow E = \frac{P_{diss}Q_i}{2\pi f_r} \tag{4.14}$$

The stored energy in a resonator given a certain generator power, can now be written by substituting Eq. 4.13 into the equation above,

$$E = \frac{2Q_r^2}{Q_c}\frac{1}{1 + 4y^2}\frac{P_g}{2\pi f_r}. \tag{4.15}$$

Taking the fractional frequency term in Eq. 4.5 and Eq. 4.10 we arrive at

$$x_0 = x - \frac{2Q_r^2}{Q_c}\frac{1}{1 + 4y^2}\frac{P_g}{2\pi f_r E_*}. \tag{4.16}$$

This is an implicit equation for the power-shifted detuning as a function of drive power. To simplify the expression we introduce the variable $y_0 = Q_r x_0$ and a nonlinear parameter,

$$a = \frac{2Q_r^3}{Q_c}\frac{P_g}{2\pi f_r E_*}. \tag{4.17}$$

The final simplified equation is then ,

$$y_0 = y - \frac{a}{1+4y^2}. \tag{4.18}$$

Rearranged this becomes a cubic equation for the normalized detuning y. Solving for the roots of the equation we see that it reaches a critical value at $a_{bif} = 4\sqrt{3}/9 \approx 0.77$. For $a \leq a_{bif}$ there is only one real solution for y_0. For $a > a_{bif}$ there is a range of y_0 with three real solutions, which correspond to three possible values for the resonant frequency and stored energy. Only two of these states are stable and correspond to the largest and smallest stored energies. Therefore above a_{bif}, we say the resonator has undergone bifurcation. The nonlinear y yielded is used in Eq. 4.2 to fit a detector when it is close to bifurcation.

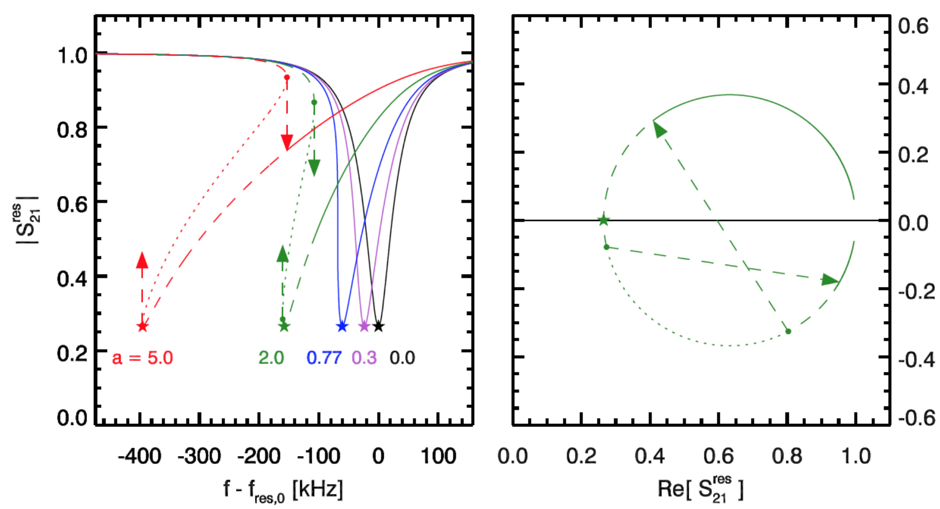

Figure 4.2: *Left*: $|S_{21}|$, for nonlinearity parameter a = 0.0, 0.3, 0.77, 2.0, and 3.0. $a_{bif} = 0.77$, is where the resonator is said to have reached bifurcation. *Right*: Complex plane for S_{21} with $a = 2.0$. The dashed lines represent regions of bifurcation. Figures from Siegel Thesis, 2016[94].

4.1.2 Impedance Mismatch

Another modification required to Eq.4.2 arises from an impedance mismatch in the output and input. This leads to an asymmetry in the resonance line profile, even at low powers. The mismatch can arise from having an amplifier at the readout output but not the input. Khalil et al. showed that this mismatch introduces an imaginary component to the coupling quality factor [54].

$$\frac{1}{\hat{Q}_c} = \frac{1}{|\hat{Q}_c|}e^{j\phi} = \mathrm{Re}\left\{\frac{1}{\hat{Q}_c}\right\} + \mathrm{Im}\left\{\frac{1}{\hat{Q}_c}\right\} \tag{4.19}$$

This results in the following complex transmission through a resonator,

$$S_{21} = 1 - \frac{1}{1+2jy}\frac{Q_r}{|\hat{Q}_c|}e^{j\phi} \tag{4.20}$$

$$S_{21} = 1 - \frac{1}{1+2jy}\frac{Q_r}{Q_c cos\phi}e^{j\phi} \tag{4.21}$$

where we have used

$$\frac{1}{Q_c} \equiv \mathrm{Re}\left\{\frac{1}{\hat{Q}_c}\right\} = \frac{cos\phi}{|\hat{Q}_c|}. \tag{4.22}$$

$\mathrm{Re}\{\frac{1}{\hat{Q}_c}\}$ is used to ensure Q_c is still the coupling quality factor.

4.1.3 The final form of S_{21}

The final form of S_{21} also needs to include the contributions from gain in the readout and any cable delay in the transmission. With these contributions the final complex form for the transmission is,

$$S_{21} = (I_0 + jQ_0)e^{-j2\pi(f-f_r)\tau(f)}\left[1 - \frac{1}{1+2jy}\frac{Q_r}{Q_c cos\phi}e^{j\phi}\right] \tag{4.23}$$

.

I_0 and Q_0 are normalization factors that describe the gain of the system. $\tau(f)$, is a phase shift with frequency due to cable delay. This final equation is fit to determine the parameters of interest f_r, Q_r, Q_c, Q_i, and a_{bif} [104].

4.2 Single-Tone KID Noise Measurements

In this section I will discuss the single-tone KID readout setup used for noise analysis of the KIDs. This readout set up uses room temperature and cryogenic electronics to collect data on one KID from an array at a time. Fig. 4.3, shows a block diagram of the single-tone readout setup. A signal generator outputs a single microwave drive tone of frequency, f. The signal is split by an RF splitter. One line, sends the signal through a variable attenuator. The variable attenuator attenuates the signal power by the desired amount. The attenuated signal is sent into the cryostat through coaxial cables to the KID array to excite the desired KID. It is then amplified with a cryogenic low noise amplifier and amplified again outside of the cryostat with room temperature amplifiers. The amplified, modulated output signal is fed into the RF port of an IQ demodulator. The second line coming from the splitter sends the signal to the local oscillator (LO) port of the IQ demodulator. The RF signal is multiplied by the LO signal for the I-channel (in-phase) and multiplied by the LO signal 90 degrees out of phase for the Q-channel (out-of-phase) of the IQ demodulator. This results in I and Q wave-forms. Each waveform is sent through a low pass filter to remove high frequency mixing products from the multiplication, and then amplified. An analog-to-digital converter (ADC) digitizes the I and Q signals for analysis.

Fig. 4.4, shows the result of plotting I and Q. The complex form of the I and Q is, $S_{21} = I(f) + jQ(f)$, and has a magnitude, $|S_{21}| = \sqrt{I(f)^2 + Q(f)^2}$. The magnitude is plotted in Fig. 4.4 *Left*, and shows the resonant feature that is typically seen when looking at the forward scattering parameter as a function of frequency for a resonator. Fig. 4.4 *Right*, shows a plot of $Q(f)$ vs. $I(f)$. This results in a resonance circle (or IQ loop), where each dot along the perimeter of the circle represents the frequency of the bandwidth that was swept across around the resonant frequency, f_r. The resonant frequency is located at the maximal rate of phase change around the resonance circle. Therefore, the resonance is located at the point where the spacing reaches a maximum along the circle. The direction tangent to the circle (red arrow) is referred to as the frequency (or phase) direction because the frequency changes in that direction. The direction normal to the circle (green arrow) is referred to as the dissipation (or amplitude direction) direction because the radius of the circle is related to the depth of the resonance feature in $|S_{21}|$.

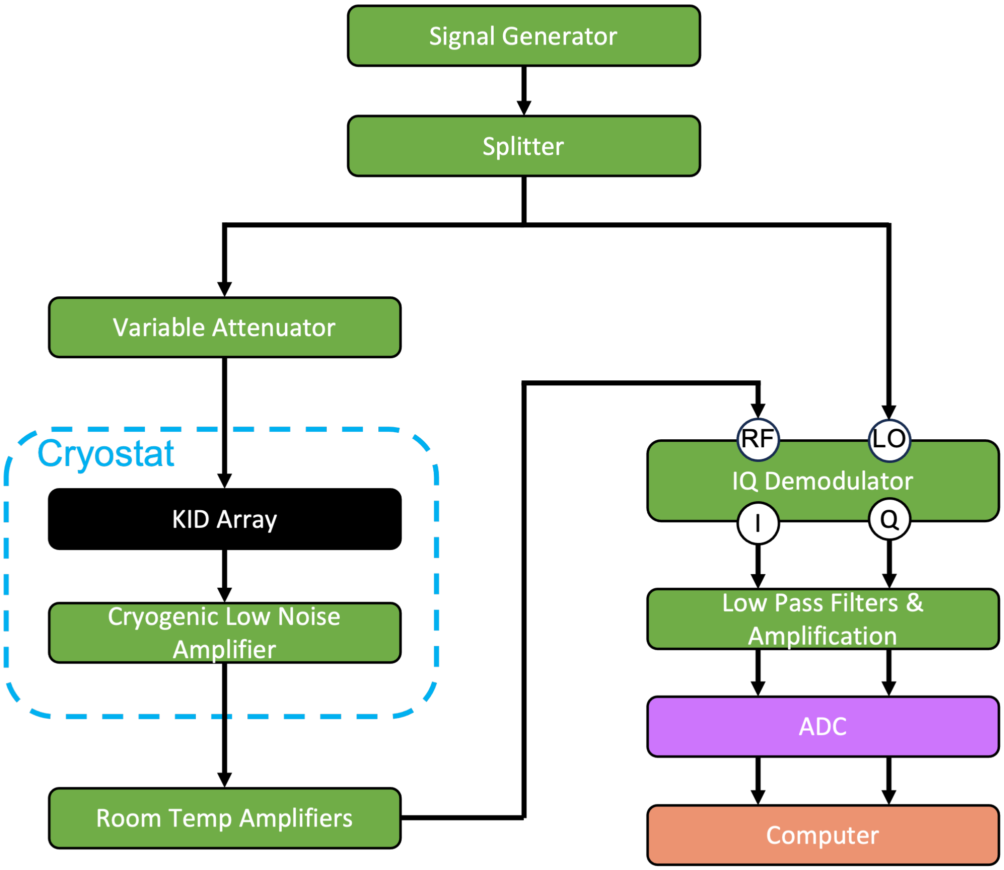

Figure 4.3: Block diagram of the single-tone readout system. A signal generator generates a microwave tone of frequency, f. The signal tone is split in two by a splitter. One line is unchanged and fed into the LO port of an IQ demodulator. The other line is sent through a variable attenuator, into the cryostat to the KID array, amplified cryogenically, then amplified again outside of the crysotat. This signal id fed to the RF port of the IQ demodulator. The RF and LO signals are mixed to form I and Q wave-forms. The wave-forms are sent through low pass filters, amplified, and sent to an ADC for data analysis.

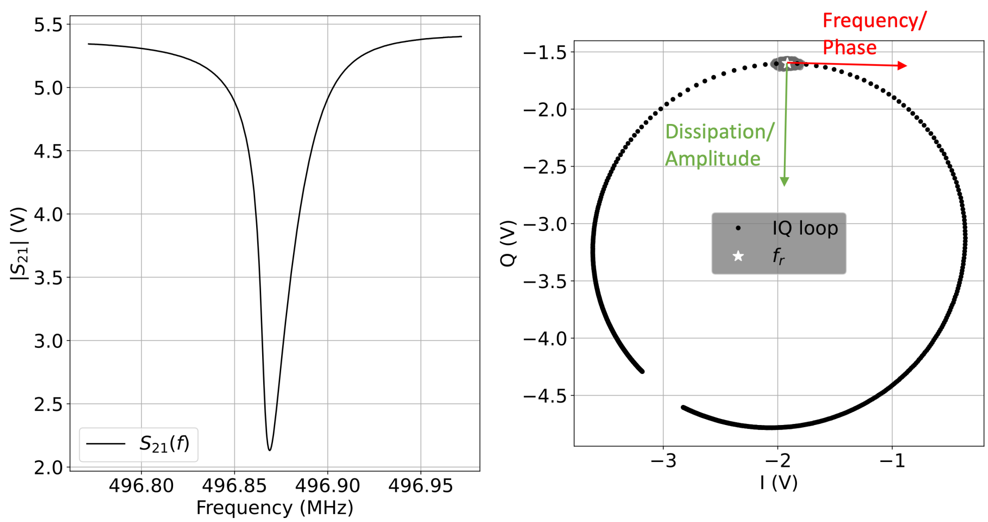

Figure 4.4: *Left*) Plot of the magnitude, $|S_{21}| = \sqrt{I(f)^2 + Q(f)^2}$, vs. frequency. *Right*) Plot of $Q(f)$ vs. $I(f)$. This results in a resonance circle (or IQ loop), where each dot along the perimeter of the circle represents the frequency of the bandwidth that was swept across around the resonant frequency, f_r (white star). The direction tangent to the circle (red arrow) is referred to as the frequency (or phase) direction because the frequency changes in that direction. The direction normal to the circle (green arrow) is referred to as the dissipation (or amplitude direction) direction because the radius of the circle is related to the depth of the resonance feature in $|S_{21}|$. On-resonance noise stream points ($I(t)$, $Q(t)$) are shown as a gray ellipse around the resonance.

4.2.1 Conversion of $I(t)$ & $Q(t)$ Noise Streams to PSDs (S_{xx})

For the work in this thesis the data we are interested in from single tone measurements are the $I(t)$ & $Q(t)$ noise streams on resonance. The noise stream allows us to calculate the power spectral density (PSD) and characterize the noise of a single KID on resonance. The following steps are taken to get $I(t)$ & $Q(t)$ on resonance:

(1) Take a finely sampled sweep of $I(f)$ and $Q(f)$ at resonance with a bandwidth that is about 4-5 times the full width half max (FWHM) of the resonance.

(2) Plot $Q(f)$ vs. $I(f)$, and determine the resonant frequency by finding the point where the maximum spacing between points along the IQ loop occurs.

(3) Then the signal generator is programmed to provide a probe tone at the resonant frequency determined in step 2 and stream $I(t)$ and $Q(t)$ for a total time, T_{stream}.

(4) We use $Q(f)$, $I(f)$, f_r, $I(t)$, and $Q(t)$ to create PSDs of the streamed data.

The right plot in Fig. 4.4, shows a plot of the IQ loop with the noise stream points ($I(t)$, $Q(t)$) (gray ellipse). Since the noise stream was taken on resonance they form random noise around the resonance in the IQ plane. To obtain the PSDs of the noise the Fourier transform of $I(t)$ and $Q(t)$ are taken and broken up into their frequency and dissipation directions. The total noise in either direction is then found by adding the components in their corresponding direction. The following steps are taken to obtain the one-sided and cross power spectral densities of $I(t)$ and $Q(t)$ and obtain the frequency and dissipation PSDs:

(1) Calculate the Fourier transform of $I(t)$ and $Q(t)$. This is done using Python's Scipy fast Fourier transform (FFT) package. With this package we take the FFT of $I(t)$ and $Q(t)$ and divide it by the total number of samples, N.

$$FT(I(t)) = \frac{FFT(I(t))}{N} \tag{4.24}$$

$$FT(Q(t)) = \frac{FFT(Q(t))}{N} \tag{4.25}$$

(2) Next, we compute the one-sided $FT(I(t))$ and $FT(Q(t))$ power spectra (PS) and their one-sided cross power spectra, which are in units of V^2. For one-sided spectra only the first half of the values in $FT(I(t))$ and $FT(Q(t))$ are used.

$$PS_I = |FT(I(t))|^2 \tag{4.26}$$

$$PS_Q = |FT(Q(t))|^2 \tag{4.27}$$

$$PS_{IQ} = |FT(I(t))FT(Q(t))^*|^2 \tag{4.28}$$

The cross power spectra is calculated by multiplying $FT(I(t))$ by the complex conjugate of $FT(Q(t))$, taking the absolute value and squaring it [78]. Cross-spectral analysis is used to extract the correlated signal from two time series [78].

(3) Now, divide the power spectra by df, the spacing between points in the noise stream in units of frequency. $df = f_{sr} * N$, where f_{sr}, is the sampling rate of the noise stream. This puts the power spectra in PSD units of V^2/Hz. The PSDs can then be written as,

$$S_I = \frac{PS_I}{df},\ S_Q = \frac{PS_Q}{df},\ S_{IQ} = \frac{PS_{IQ}}{df}. \tag{4.29}$$

(4) We are interested in the frequency and dissipation directions of the noise, so we need to separate the noise streams for $I(t)$ and $Q(t)$ into their frequency and dissipation components. To do this we must rotate the noise by an angle ϕ_x with respect to the IQ basis. We do this by taking the derivative of the following vector-valued-function, $\vec{V}(f) = I(f)\hat{I} + Q(f)\hat{Q}$, to

find the slopes of I and Q near resonance, then finding the angle between the two slopes[34]:

$$\begin{aligned}\frac{d\vec{V}}{df} &= \frac{dI}{df}\hat{I} + \frac{dQ}{df}\hat{Q} \\ &= m_I\hat{I} + m_Q\hat{Q}.\end{aligned} \tag{4.30}$$

$$\theta_{IQ} = \text{acrtan}\left(\frac{m_Q}{m_I}\right). \tag{4.31}$$

$$\phi_x = \theta_{IQ} + \frac{\pi}{2}. \tag{4.32}$$

m_Q and m_I are the slopes of lines $Q(f)$ and $I(f)$, respectively. The slopes, change linearly with frequency near resonance and are found by doing a linear fit on a few data points of I and Q near resonance. Now, we can rotate the noise into the frequency ($Freq(f)$) and dissipation ($Diss(f)$) basis. This is done by applying the following linear transformation[94]

$$\begin{bmatrix} Diss(f) \\ Freq(f) \end{bmatrix} = \begin{bmatrix} \cos\phi_x & \sin\phi_x \\ \text{-}\sin\phi_x & \cos\phi_x \end{bmatrix} \times \begin{bmatrix} I(f) \\ Q(f) \end{bmatrix}. \tag{4.33}$$

After cross multiplying, we can apply steps 1-3 to derive the following PSDs in the frequency (S_{freq}) and dissipation (S_{diss}) directions:

$$S_{freq} = S_I\sin^2\phi_x + S_{IQ}\sin\phi_x\cos\phi_x + S_Q\cos^2\phi_x \tag{4.34}$$

$$S_{diss} = S_I\cos^2\phi_x + S_{IQ}\sin\phi_x\cos\phi_x + S_Q\sin^2\phi_x \tag{4.35}$$

Once steps 1-3 have been done all that is needed is to determine ϕ_x. Then the values from Eqs. 4.29 and 4.32 can be directly plugged into Eqs. 4.34 and 4.35.

(5) Lastly, in our system we measure shifts in fractional frequency space, not shifts in voltage. Therefore, we need to convert from units of V^2/Hz to PSDs in normalized frequency shift units, $x = \Delta f/f_r$. These PSDs are identified by the following notation, S_{xx}, and have units of 1/Hz. The conversion starts by once again taking the derivative of $\vec{V}(f) = I(f)\hat{I} + Q(f)\hat{Q}$ to find the slope near resonance, and squaring it to end up with units of V^2/Hz^2. Next, the value calculated from $\left|\frac{d\vec{V}}{df}\right|^2$ is multiplied by f_r^2. The PSDs are divided by $\left|\frac{d\vec{V}}{df}\right|^2 f_r^2$, leaving the resulting PSDs in units of 1/Hz.

$$S_{xx,freq} = \frac{S_{freq}}{\left|\frac{d\vec{V}}{df}\right|^2 f_r^2} \tag{4.36}$$

$$S_{xx,diss} = \frac{S_{diss}}{\left|\frac{d\vec{V}}{df}\right|^2 f_r^2} \tag{4.37}$$

Fig. 4.5, shows an example of on-resonance and off-resonance $S_{xx,freq}$ and $S_{xx,diss}$ PSDs from Adalyn Fyhrie's thesis [34]. When the noise is taken off-resonance we can gauge the contribution of the system noise. The system noise includes electronic noise, such as amplifier noise. When noise is taken on-resonance there is an excess noise in the frequency direction that arises from the detector noise. The same is not seen with the on-resonance dissipation noise. Therefore, the detector noise is mostly limited to the frequency direction and other noise contributions from electronics such as amplifiers can be determined from the dissipation direction. When discussing noise measurements the terms frequency/phase and dissipation/amplitude will be used interchangeably throughout the thesis. Noise measurements are needed to determine the sensitivity of the KIDs, since the NEP = $\sqrt{S_{xx}}/R$. From the noise we can also characterize the TLS noise of the device, the white noise from thermally and/or optically generated quasiparticles, and estimate a quasiparticle lifetime. Noise characterization will be discussed in further detail in Sec. 5.3.

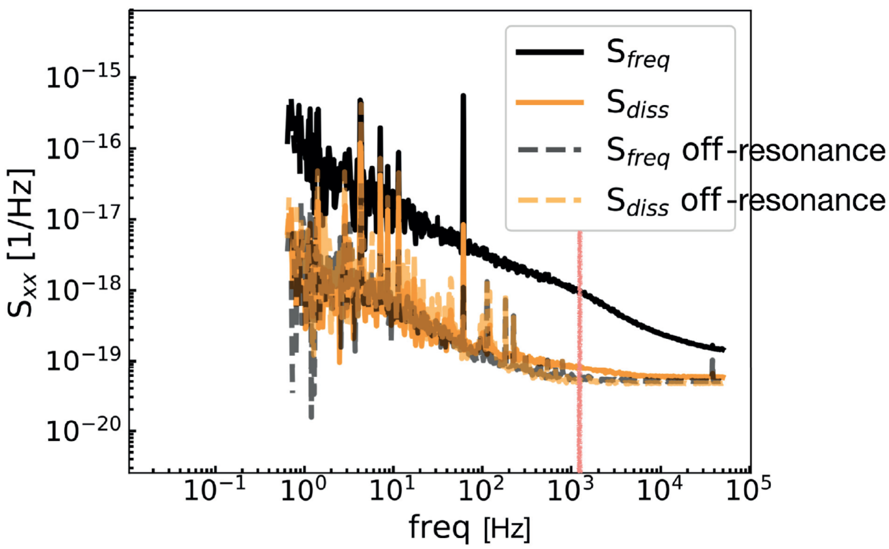

Figure 4.5: Example of on and off resonance noise PSDs. The dashed lines are off resonance and the solid lines are on resonance. Black lines are noise in the frequency (phase) directions. Orange lines are noise in the dissipation (amplitude) direction. The detector noise roll off in the frequency direction is marked with a vertical pink line [34].

Chapter 5

TiN KIDs for BEGINS

In this chapter I will focus on the design and characterization of a 25 μm BEGINS KID prototype array, the shortest wavelength covered by BEGINS. I will present the KID resonator type, superconducting material, array schematic, and the optical coupling scheme chosen for the BEGINS KIDs. I will discuss the dark and optical measurements made on a prototype BEGINS array, their results and difficulties faced due to constraints on the prototype array design. Lastly, I will discuss the plan for future work on BEGIN KIDs for 25 μm. The work towards this research was split up as follows: Peter Day designed the prototype array, the prototype array was fabricated at JPL by Henry Leduc, dark measurements were made at JPL and the analysis was done by me, optical measurements were made by me at GSFC and the analysis was done by me. The ultimate goal of this chapter is to determine if the BEGINS NEP requirement at 25 μm of 2×10^{-16} W/$\sqrt{\text{Hz}}$ is achievable in our optical lab setup.

The goals and purpose of the dark measurements discussed in this chapter are to determine the KID arrays f_r, T_c, α, Q_i, Q_c, and array yield. This is important for the following reasons:

(1) If these values deviate significantly from the expected design or predicted values there is an issue with the fabrication and/or material that must be investigated and addressed.

(2) The responsitivies and sensitivities of the KIDs have a dependence on T_c, α. Therefore estimating these values will help us understand what may be limiting the NEP if we do not meet the requirement at 25 μm.

The goals and purpose of the optical measurements discussed in this chapter are to determine the KID arrays noise PSDs (S_{xx}), τ_{qp}, and empirical NEPs. This is important for the following reasons:

(1) The noise PSDs are needed to calculate the empirical NEPs. From them we confirm that the noise in the frequency direction is dominated by detector noise sources and not the readout system or the low noise amplifier (LNA). This is done by comparing the frequency direction noise PSDs to the dissipation direction noise PSDs.

(2) The responsitivies and sensitivities of the KIDs have a dependence on τ_{qp} and TLS noise (S_{TLS}). Both of which are extracted from fits to the noise PSDs in the frequency direction. This is further explained in Sec. 5.3.4. If τ_{qp} is too short or S_{TLS} is too high we may not meet the BEGINS NEP requirement.

(3) Compare responsivity models (Model 1 and Model 2) explained in Sec. 3.2.2 to determine which best fit fractional frequency measurements.

(4) Test the sensitivity model by comparing the empirical NEP in the frequency direction.

The ultimate goal of this work is to determine if the BEGINS NEP requirement at 25 μm of 2×10^{-16} W/$\sqrt{\text{Hz}}$ is achievable in lab.

5.1 BEGINS KIDs Design

The resonator type chosen for the BEGINS KIDs was a lumped-element KID (LEKID), or a lumped-element resonator. In this design the resonator contains a discrete inductor and capacitor on a silicon (Si) substrate. A schematic of the BEGINS LEKID is shown in Fig. 5.1. The inductive portion is comprised of a meander in a circular envelope with a diameter of 100 μm. The capacitor style chosen was a parallel plate capacitor (PPC). The base layer of the resonator is made of 50 nm thick sub-stoichiometric titanium nitride (TiN) with Tc adjusted in the range 1 - 1.5K. This layer will stay fixed across the whole fabricated array. This layer is shown in the schematic as the purple portion that makes up the inductor and the bottom electrodes of the PPC. The inductor is connected to the base electrodes at the top and bottom of the circular envelope. The top electrode of the capacitor is made of patterned 200-300 nm thick niobium (Nb) which is also used as the readout line. 150 nm thick amorphous silicon (aSi) is used as the dielectric layer between the top and bottom electrodes. The capacitors are two PPCs in series and split into two parts. The left side of the capacitor is fixed and sets the minimum capacitance for the array. The right side has a variable Nb top electrode with a maximum length of 250 μm. The resonant frequencies across the prototype array are set by the length of the top electrode. The designed BEGINS prototype array for testing has 192 KIDs with an expected frequency span from 154-509 MHz.

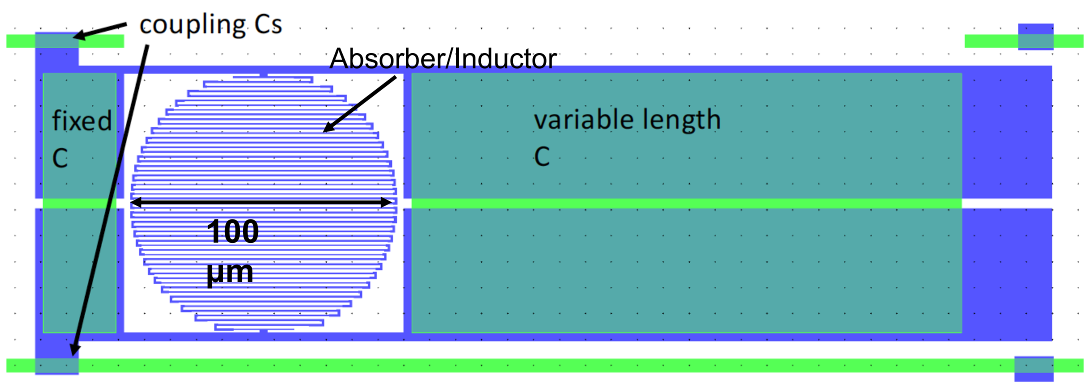

Figure 5.1: Schematic of a BEGINS TiN KID pixel for λ= 25 μm. Purple: 50 nm TiN. The inductor and capacitor base electrodes are comprised of TiN. Green: 200-300 nm Niobium (Nb). The capacitor top electrode and coupling feedlines are compromised of Nb. 150 nm thick amorphous Silicon (aSi) is placed between the capacitor electrodes. This design was created by Peter Day and fabricated by Rick Leduc at JPL.

TiN was chosen as the superconducting material for a few reasons. TiN has been shown to have low microwave loss with high Q_i's on the order of $\sim 1 \times 10^7$[101]. TiN KIDs have been reported to have quasiparticle lifetimes on the order of 200-300 μs [25]. Both higher Q_i and longer quasiparticle lifetimes lead to a high responsivity KID. TiN has also shown to have a higher surface resistance when compared to aluminum or niobium, which makes it easier to use the inductor as a good far-IR absorber to couple to a microlens[80].

A PPC was chosen over other capacitor geometries to decrease TLS noise, because the high

E-field section of the resonator is located in the capacitor [16, 36, 80]. For a PPC most of the E-field is confined within the parallel walls, so there will be less area across the resonator with E-fields at metal/dielectric interfaces for TLSs to be generated and create noise. A decrease in the TLS noise with PPCs has not been thoroughly investigated in the literature, so I compare our results to those found in the literature for IDCs. Another advantage is PPCs enable smaller pixels when compared to IDCs which enables a compact instrument. This is well depicted in Fig. 5.2 from work done by done by Samir Beldi, et al [8]. The figure shows an IDC KID (Left) and a PPC KID (Right) made with the same inductive meander and designed to have the same resonant frequency of 942 MHz. The pixel size was reduced by a factor of 26 with a PPC.

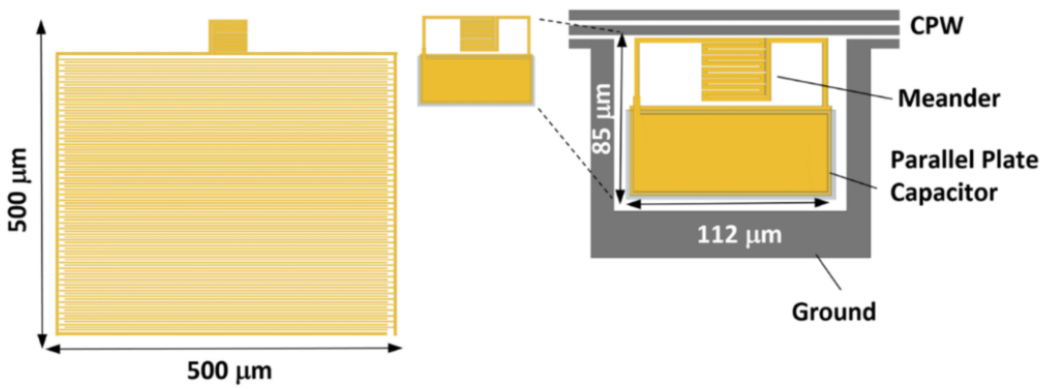

Figure 5.2: *Left*: Sketch of IDC LEKID. *Right*: Sketch of PPC LEKID. Both LEKIDs are designed to have a resonant frequency of 942 MHz. The PPC allows for the pixel to be reduced by a factor of 26.[8]

5.1.1 BEGINS KIDs Optical Coupling Scheme

For this prototype array we chose to use a Fresnel-zone plate (FZP) lens array to couple radiation to the BEGINS KID inductors. FZP lenses were attractive because they are single layer planar structures that are easily patterned onto the back-side of the KID substrate which provided a fast path to optical measurements. FZP lenses use diffraction and interference to focus light onto a sample. They consist of concentric annular rings that alternate between transparent and opaque. In our FZP lenses the opaque zones are made of 100 nm gold. When a plane wave is normally incident on the FZP the light that passes through reaches the focal point with phases that differ by less than one half-period. The superposition of the portions result in an intensity at the chosen axial point [105]. The following equation is used to determine the radii of the concentric rings

$$r_n = \sqrt{nf\lambda_0 + \frac{n^2\lambda_0^2}{4}}, \tag{5.1}$$

where n is the integer representing the concentric ring, f is the focal length, and λ_0 is the wavelength of light that the FZP is focusing [105]. The focal length of our FZP lenses is the thickness of the Si wafer used for our prototype array (625 μm). 17 out of the 192 KIDs are not coupled to a FZP lens, instead they are blocked with gold to prevent illumination to compare the response between illuminated and non-illuminated KIDs. Flight KID arrays will be equipped with microlens arrays.

Fig. 5.3 shows the FZP ring dimensions and a plot of the expected encircled energy (EE) efficiency. The light blue regions are the two transparent zones and the orange region is the gold opaque zone. The numerical integration of the efficiency was done by Nicholas Cothard. We are interested in the EE efficiency for a radius of 50 μm, the radius of the BEGINS KIDs inductors. The results show that for a 50 μm radius the EE efficiency is 35%. We must also take into account the power loss from reflections off the metal surface. This is accounted for by calculating the fraction of the total FZP lens area that is transparent, $(R_2^2 - R_1^2 + R_0^2)/R_2^2 = 0.67$. The final expected FZP efficiency is $FZP_{eff} = .35 \cdot .67 = .23$ (23%), and is used to calculate the blackbody power incident on the inductors in the optical performance section, Sec. 5.3.

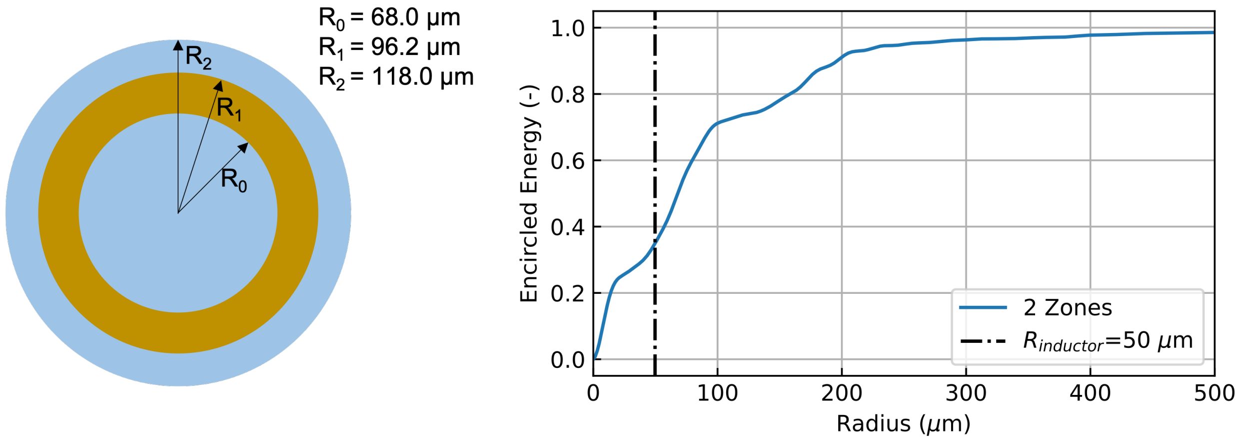

Figure 5.3: *Left)* FZP ring dimensions and a plot of the expected encircled energy (EE) efficiency. The light blue regions are the two transparent zones and the orange region is the gold opaque zone. *Right*: Numerical integration of the FZP encircled energy (EE) efficiency for two transparent zones, done by Nicholas Cothard. The EE efficiency at the inductor radius of 50 μm is 0.35.

5.2 Dark Measurements

In this section I will describe the results of dark measurements made on the BEGINS KID prototype array to determine the array yield, resonant frequencies, quality factors, T_c, and α. These measurements were made in a cryogenic test bed in our lab at GSFC by me and Peter Day's lab at JPL. Analysis was performed by me.

5.2.1 Low Temperature Resonant Frequencies and Quality Factors

The resonant frequencies and quality factors Q_r, Q_i, and Q_c were determined by measuring S_{21} of the prototype array with a VNA. This measurement was made at GSFC. The resonant frequencies and quality factors were estimated using the fitting routine explained in Sec. 4.1. Fig. 5.4 shows the full S_{21} sweep of the prototype array. The standing wave across the sweep is likely due to impedance mismatches between electrical readout components and the roll-off at 300 MHz is due to a room-temp amplifier.

The targeted design frequency span ranged from 154-509 MHz, with a bandwidth of 355 MHz.

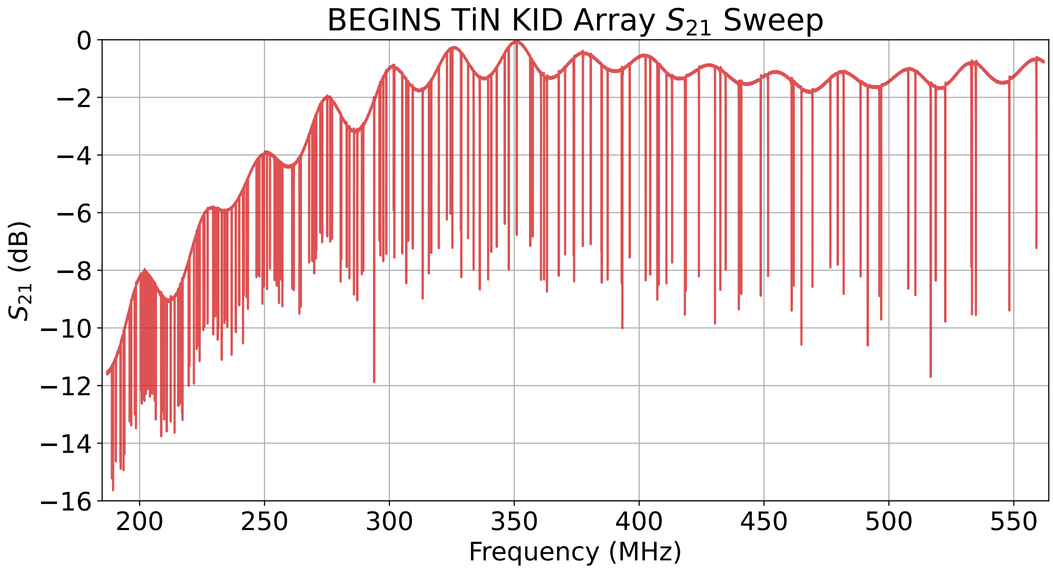

Figure 5.4: BEGINS KIDs prototype array VNA S21 Sweep. The measured frequency span ranged from 189-560 MHz, giving a bandwidth of 371. The prototype array was expected to have 192 resonators. However, only 181 resonators were identified, giving a yield of 94.3%. The standing wave shown across the sweep is likely due to impedance mismatches between electrical readout components and the roll-off at 300 MHz is due to a room-temp amplifier.

The measured frequency span ranged from 189-560 MHz, giving a bandwidth of 371 which differs from the design bandwidth by 4.5%. The difference in the design to the measured frequency span will arise from differences in the fabricated versus design capacitors and inductors of the KID. The measurements yielded 181 out of 192 resonators, providing a yield of 94.3%. Of the 181 resonators identified 175 were non-collided resonators. Since the resonators are densely packed within a certain frequency span variations in the film thickness or KID geometry such as top electrode capacitor lengths, aSi thickness, and the inductor meander geometry will cause resonators near each other in frequency space to shift and collide.

Fig. 5.5 shows the estimated quality factors Q_r, Q_i, and Q_c. Both Q_r and Q_c have a bimodal distribution. If Q_c is bimodal Q_r will be as well, because Q_r and Q_c are positively correlated, as shown in Fig. 5.6. The array is designed such that $Q_c = 1 \times 10^5$ and is constant for all detectors. Q_c varies from 3×10^4 to 1×10^5, with an average $Q_c = 7 \times 10^4$. The bimodal distribution in

Q_c may be due to possible variations across the prototype array film thickness, substrate thickness between the PPC walls or KID geometry. However, we were not able to confirm this. This will not affect the empirical NEPs. Q_i, has a more normal distribution-like shape with an average of $6 \times 10^4 \pm 5 \times 10^3$. From these values the coupling efficiency to the feedline is $\chi_c = 0.99$. This values near unity to maximizes the response of the resonator.

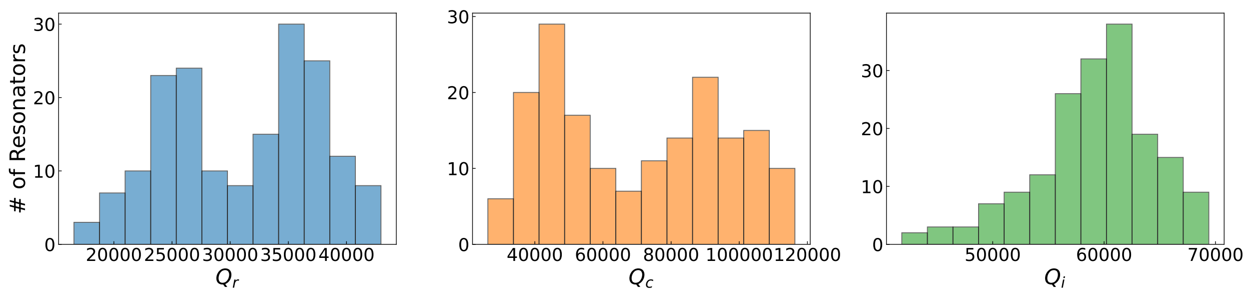

Figure 5.5: Histograms of Q_r, Q_c, and Q_i of the BEGINS KID prototype array. Q_r varies from 1.7×10^4 to 4.3×10^4 and Q_c from 2.6×10^4 to 1.2×10^5. Q_i, has a more normal distribution-like shape with an average of $5.9 \times 10^4 \pm 5.4 \times 10^3$.

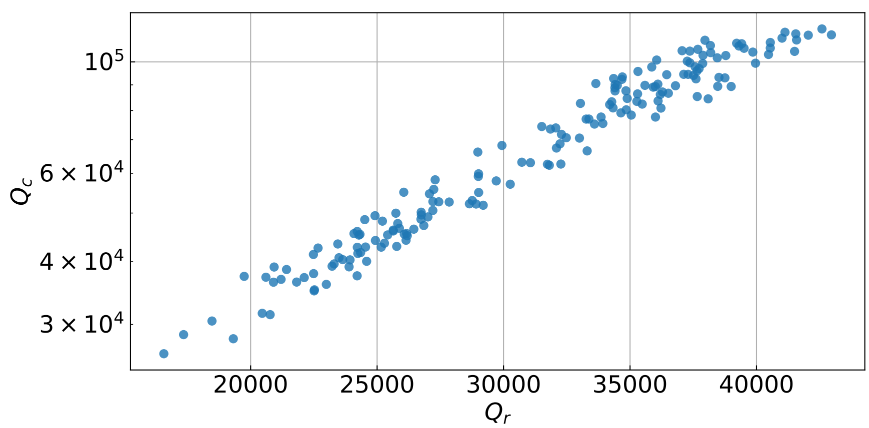

Figure 5.6: Plot showing that the fit parameters Q_r and Q_c are positively correlated.

5.2.2 T_c and α Measurements

A bath temperature sweep measurement was made by Peter Day at JPL and I performed the analysis. The temperature sweep response was recorded for 4 resonators with resonant frequencies of 223.4, 275.04, 464.81, and 530.73 MHz. Fig. 5.7 shows the response of the resonator with a resonant frequency at 223.4 MHz from 300-600 mK. As the temperature increases the number of thermal quasiparticles increases leading to a decrease in the resonant frequency and quality factor of the resonator. The top plot in Fig. 5.8 shows the fractional frequency shift response versus bath temperature of all four resonators which have a similar response. T_c and α of the KIDs were estimated by applying the model described in Sec. 3.1.2 and using a χ^2 minimization fitting method with α and Δ_0 as the free parameters. The left bottom plot in Fig. 5.8 shows the results for the best fit of the resonator, $f_r = 223.44$ MHz. The fit yielded $\alpha = 0.22$ and $\Delta_0 = 2.16 \times 10^{-4}$ eV, which corresponds to a $T_c = 1.42$ K. Fit results for all resonators are displayed in table 5.1, where the average $T_c = 1.43$ K and $\alpha = 0.23$. The expected T_c of the prototype array was between 1-1.5 K, so the estimated T_c is a reasonable value. However, since we were not able to make a four-wire resistance measurement we could not verify T_c. The low estimate for α is unusual since TiN is known to have a high α in the literature [47]. These results could be erroneous if our estimate for T_c is incorrect. Detectors with these T_c and α parameters may still meet requirements for BEGINS NEPs which will be discussed further below.

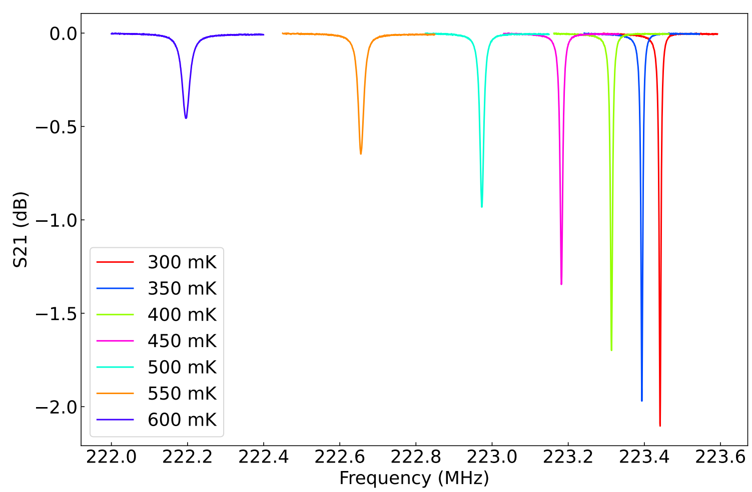

Figure 5.7: Temperature dependence of a resonator at 223.44 MHz from a fabricated BEGINS TiN KIDs prototype array. The resonator shows the expected response of shifting to lower frequencies and decreasing quality factor, as the temperature increases from 300 mK to 600 mK.

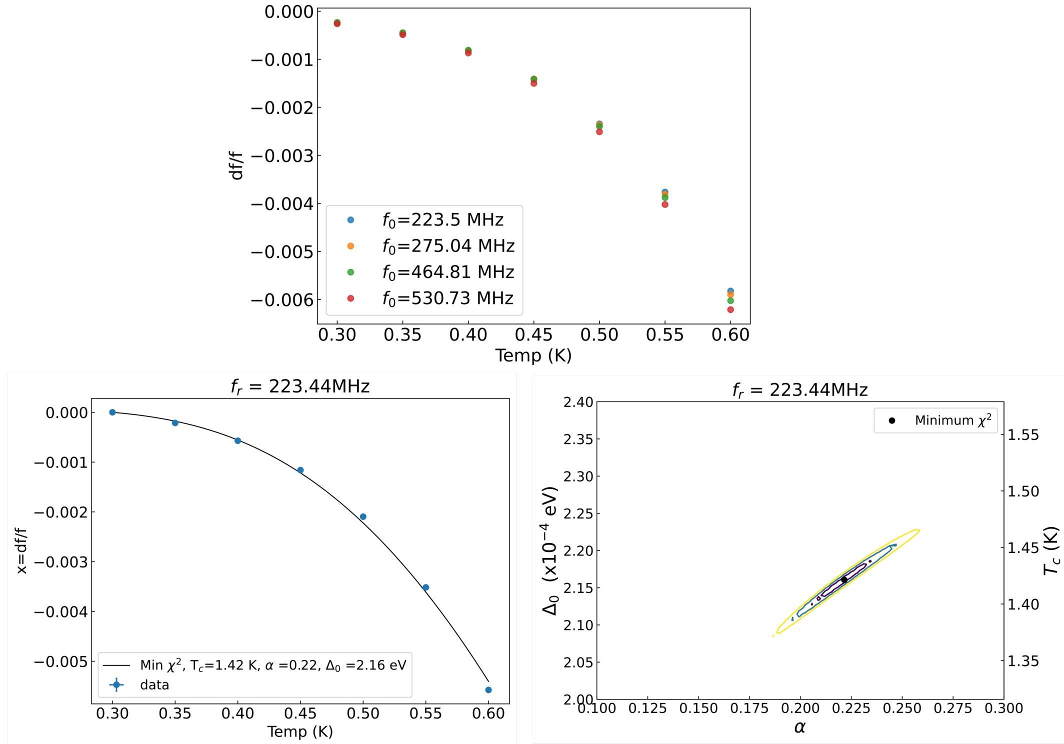

Figure 5.8: *Top*: The fractional frequency response (x) as a function of bath temperature from 300 mK to 600 mK for four resonators from the BEGINS KID prototype array. We see an over all shift of $\sim 6 \times 10^{-3}$ at 600 mK. *Bottom Left*: Blue Dots: Fractional frequency response of resonator with $f_r = 223.4MHz$. Black line: Best fit to model using minimum χ^2 method. *Bottom Right)* $\Delta\chi^2$ contour plots of 1σ, 2σ, 3σ uncertainty in the parameters.

f_r (MHz)	α	Δ_0 ($\times 10^{-4}$ eV)	T_c (K)
223.44	0.22	2.16	1.42
274.97	0.23	2.17	1.43
464.7	0.24	2.19	1.44
530.59	0.23	2.16	1.42

Table 5.1: Minimum χ^2 fit results for all four resonators chosen from the BEGINS KID prototype array. The fit estimated the parameters α and Δ_0. T_c, is then calculated using the relation from BCS theory, $\Delta_0 = 1.764 k_B T_C$.

5.3 BEGINS KIDs Optical Performance

Optical test on the prototype array were performed in our cryogenic test bed at GSFC. The tests were performed with a cryogenic blackbody at temperatures of 6, 40, 60, 80, 90, and 100 K.

The prototype array was kept at a bath temperature of 326 mK. We were not able to test it at the BEGINS operating bath temperature of 300 mK, because the optical load of the blackbody at 100 K increased the temperature of our 300 mK stage to $\sim$ 324 mK. The elevated bath temperature will lead to an increase in G-R noise that may increase the empirical NEP at lower loading where it is not photon noise dominated. The KID array was placed in a package such that the blackbody radiation would be focused onto the KID inductors by the Fresnel-zone plate lenses and filter stacks provided by Cardiff University were used to define the bandpass at 25 μm.

Two different types of measurements were made. We recorded S_{21} sweeps with a VNA at each blackbody temperature to measure the fractional frequency response of the detectors relative to the lowest blackbody power (6 K). The second set of measurements were single tone measurements of 12 different resonators. The single tone measurements allow us to measure S_{xx} as a function of optical power. The empirical NEPs of the 12 resonators are determined by the responsivity calculated from the fractional frequency response and S_{xx} as a function of optical power.

5.3.1 Optical Measurements Set Up

The complete experimental set up for the optical measurements is shown in Fig. 5.9. The left figure shows a schematic of the cross-sectional view of the assembly and the right figure shows a physical image. The cryogenic blackbody is attached to the 4 K stage of our cryostat by four stainless steel legs. It is made of four aluminum walls with a 500 μm aperture facing the FZP lenses. Within the walls is a copper tile with a black absorptive material attached facing the aperture. On the top side of the copper tile is a 100 Ω resistor used to heat the blackbody with DC wiring. We control the amount of power applied to the resistor using a python script. The mount is attached to an aluminum frame using G10 struts. G10 was used as part of the frame because it is a good thermal insulator, has a low thermal expansion coefficient, and allows us to keep the overall mass low. This is important because the larger the mass the longer it will take to heat up or cool down the blackbody. A copper tile was used for its high thermal conductivity allowing it to heat the black absorptive material. The copper tile was also kept small to decrease the mass.

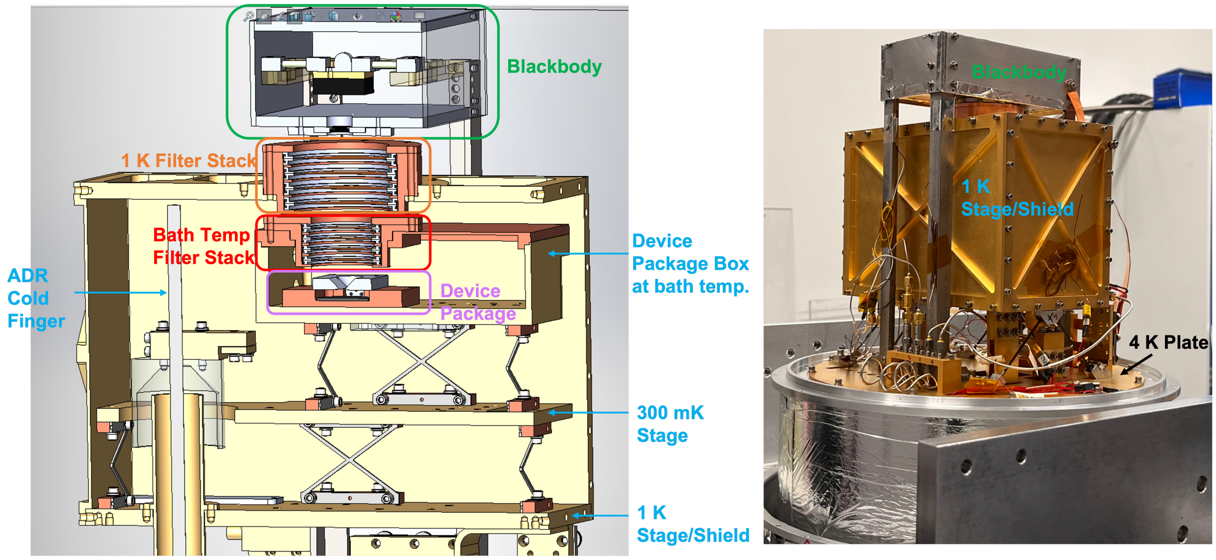

Figure 5.9: Cryogenic optical measurement experimental set up. The cryogenic blackbody is attached to the 4 K stage of our cryostat by four stainless steel legs. It is made of four Al walls with a 500 μm aperture facing the Fresnel zone plate lenses. Within the walls is a copper tile with a black absorptive material attached facing the aperture. On the top side of the copper mount is a 100 Ω resistor used to heat the blackbody with DC wiring. We control the amount of power applied to the resistor using a python script. The mount is attached to an aluminum frame using G10 struts. The structure within the aluminum walls was constructed by Nicholas Cothard.

Below the blackbody is the first filter stack (1K Filter Stack), which is thermally coupled to the 1 K stage of the set up. The second filter stack (Bath Temp Filter Stack) is attached to the box that is kept at the same temperature as the detector array. The filter stacks have identical bandpasses, and are made of metal mesh deposited on a polypropylene substrate. Both stacks consist of four filters that create a bandpass centered at 25 μm with a bandwidth from $\sim$ 22-28 μm. The four filters consist of a 25 μm bandpass, 300 icm high-pass filter, 600 icm low-pass filter and a 1050 icm low-pass filter. The transmission of each of these is shown in Fig. 5.10. The transmission of the filter stacks in series is used to calculate the total power incident on the detectors by the blackbody in section 5.3.2.

Fig. 5.11 shows the KID array packaging. It is made of gold-plated, oxygen-free high conductivity (OFHC) copper. OFHC copper is the purest copper available with levels of oxygen as low

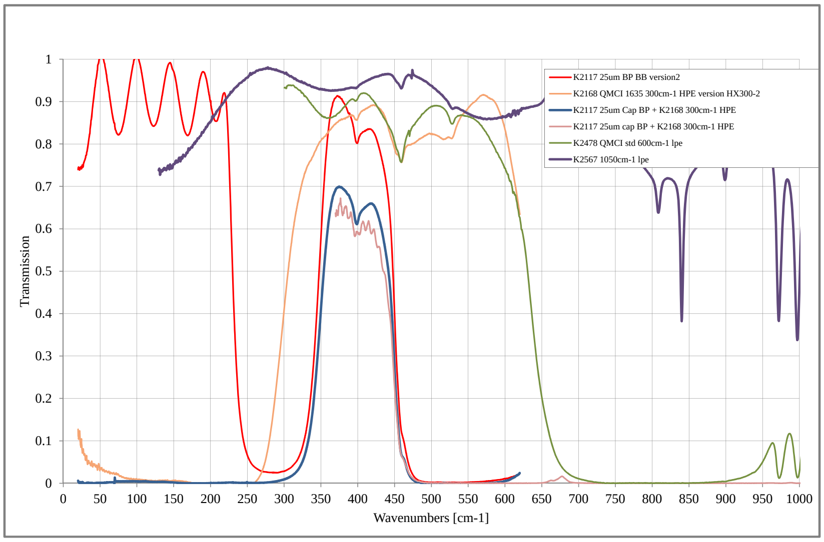

Figure 5.10: The transmission of the filters used in the optical experimental set up. The filters are made of metal mesh deposited on a polypropylene substrate. Both stacks consist of four filters that create a bandpass centered at 25 μm with a bandwidth from $\sim$ 22-28 μm. The four filters are a 25 μm bandpass, 300 icm high-pass filter, 600 icm low-pass filter and a 1050 icm low-pass filter.

as 0.001 %. It allows the inherent properties of copper to be enhanced by decreasing the amount of impurities in regular copper. It has a high thermal conductivity that allows the prototype array to be cooled down to the desired temperatures. The prototype array is attached to the lid of the package (Top), as shown in the cross-sectional view of the package. The KIDs face the bottom section of the package, which has a rectangular inset to ensure the prototype array does not touch the package. At the bottom of the package is a black disk made of metal velvet, a wide-band (extreme UV to far-IR), absorbing aluminum foil with 99.9% specular absorptance [1] , which is used to absorb stray light. The top of the package has a v-shaped opening made to expose the FZP lens array to the blackbody. To ensure stray light was not reflected into the lenses black epoxy was placed along the lining of the walls of the opening. Fig. 5.12 shows the images of the physical package containing the prototype BEGINS TiN KID array with the FZP lens array. The prototype

[1] https://acktar.com/product/metal-velvet-2/

array package is mounted into the box shown in Fig. 5.9 Left and has MCX plugs to SMA cables for readout. The box containing the prototype array package is thermally coupled to the 300 mK stage using a copper film and has a 100 Ω resistor and thermometer attached to the bottom on the outside. DC wiring is used to heat the resistor to the desired temperature of 326 mK with a thermo-servo controlled system.

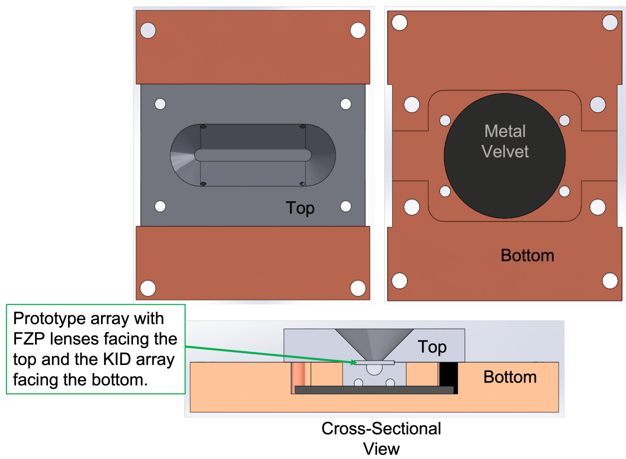

Figure 5.11: CAD drawings of the prototype array package.The prototype array is attached to the lid of the package (Top), as shown in the cross-sectional view of the package. The KIDs face the bottom section of the package. The bottom of the package has a rectangular inset to ensure the prototype array does not touch the package. There is a black disk made of metal velvet attached to the bottom of the package. It is used to absorb stray light and prevent it from being reflected back onto the KID array. The top of the package has a v-shaped opening made to expose the FZP lens array to the blackbody. The package was designed by Peter and the bottom was modified to mount in our test bed.

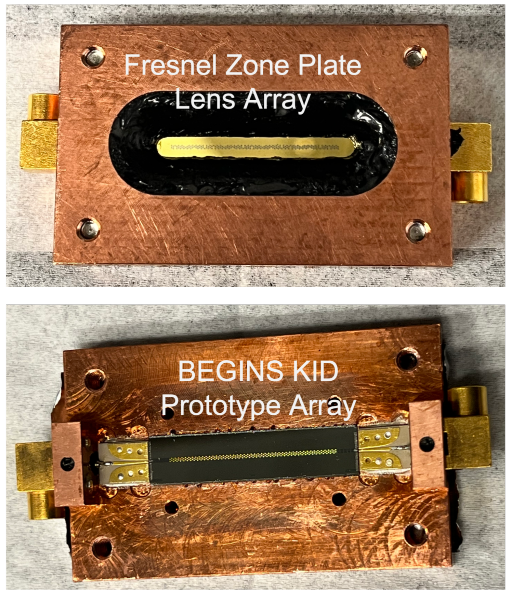

Figure 5.12: Images of the physical package containing the prototype BEGINS TiN KID array with the FZP lens array. To ensure stray light would not be reflected into the lenses black epoxy was placed along the lining of the walls of the opening shown in the top image.

5.3.2 Measurement Results for df/f & R_x

Here I discuss the results of the VNA sweeps I performed to determine the fractional frequency shift of the resonators as a function of blackbody temperature. I will also compare Model 1 and Model 2 responsivity models discussed in Sec. 3.2.2.

Fig. 5.13, shows histograms of the fractional frequency response at T_{BB}= 40, 60, 80, 90, and 100 K, where $df/f = \frac{f_r(T_{bb}) - f_r(T_{bb}=6K)}{f_r(T_{bb}=6K)}$. In the response from 80-100 K there is a distinct group of the same 12 resonators with low response. These resonators may include some of the 17 that were not coupled to FZP lenses. However, this was not confirmed because we did not have a method to spatially map the measured frequencies to the design frequencies on the array. To the left of the low response group is a larger group of resonators with a skewed distribution. If all resonators were absorbing similar amounts of radiation we would expect a normal distribution. In Fig. 5.3 it is evident that about 60 % of the radiation is not focused onto the inductor and it will scatter within the Si substrate and be absorbed by neighboring KIDs. Our hypothesis is that the skewed distribution might be due to stray light reaching detectors from neighboring FZP lenses.

To test this hypothesis we started with separating the skewed distribution at 80 K into two groups a "mid response group" and "high response group" (Fig. 5.13 red histogram). The "mid response group" is made up of the resonators within the response from $\sim -1.0\times10^{-5}$ to -0.50×10^{-5} with a mean response of -0.78×10^{-5}. Note that the the more negative the response the greater the optical response. The remainder of the resonators in the group to the left of the mid response group ($df/f < -1.0 \times 10^{-5}$) make up the high response group. We found that 98 resonators from the mid response group at 80 K were consistent with the mid response groups designated for 90 K and 100 K. From the high response group 53 resonators matched at 80, 90 and 100 K. The low response group contained the same 12 resonators at 80, 90 and 100 K. Therefore only 163 out of the 175 non-colliding resonators were matched to response groups. Resonators that could not be matched were left out of the analysis discussed below.

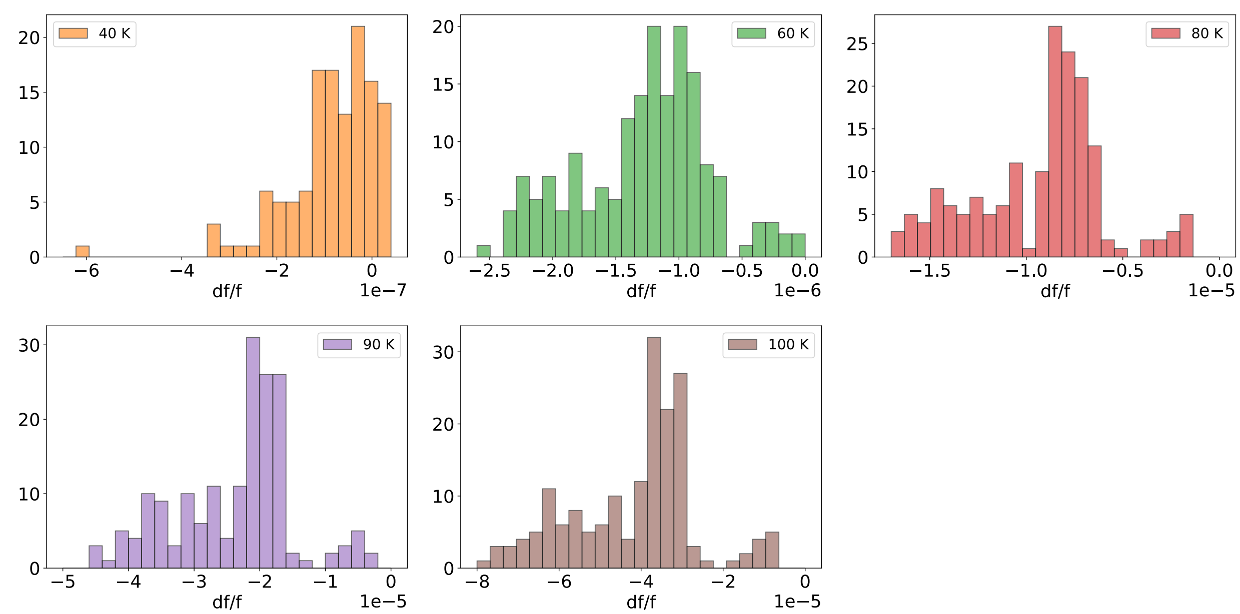

Figure 5.13: Histograms of BEGINS TiN KID array responses (df/f) at blackbody temperatures 40 K, 60 K, 80 K, 90 K, and 100 K. Since there are 17/192 KIDs not coupled to a Fresnel zone plate lens we expect there to be a group of KIDs with low response due to chip heating, stray light or radiation trapped in the Si substrate. This group is seen from 60-100 K. The low response group in 80-100 K have the same 12 resonators.

After confirming the number of resonators in each group were consistent 80, 90 and 100 K we determined if they matched the number of resonators found with a certain number of neighboring FZP lenses. The left figure in Fig. 5.14 shows a section of the FZP pixel layout. A KID can have 2, 3, 4 or 5 neighboring FZP lenses with this type of pattern. The histogram in Fig. 5.14 displays the number of resonators with 2, 3, 4 or 5 neighboring FZP lenses. If the hypothesis is correct a resonator with a larger number of neighbors will absorb more stray light and inflate the response of a resonator. The 17 design resonators not coupled to lenses have either 3 or 5 neighboring resonators. Of the 17, 8/17 have 3 neighbors and 9/17 have 5 neighbors. Given that only 163 of 192 design resonators were matched we can estimate how many of the 17 design resonators not coupled to lenses we would expect to find in the 163. For 17/192 design resonators not coupled to FZP lenses, we expected to find 14/17 resonators in the group of 168. This number is close to the 12 resonators found in the low response group. This method is used on the resonators coupled to lenses as well.

Table 5.2 shows the number of lens-coupled resonators out of the 163 that we expect to have with 2, 3, 4, or 5 neighboring lenses. From these values we inferred which resonators belonged to the mid and high response groups. Assuming that the mid response group is made up of resonators with 2, 3, and 4 neighbors it would contain 99 out of the 163 resonators. This leaves 52 resonators in the high response group, that arise from resonators with five neighbors. These values are very similar to what we see in the data, where there are 98 in the mid response group and 53 in the high response group. This analysis suggests that the mid response group is primarily made up of resonators with three neighbors and the high response group is primarily made up of resonators with five neighbors. Although these numbers agree well we were not able to verify this by spatially mapping the pixels on the array.

We chose a group of resonators from each response group for which to estimate responsivities and calculate empirical NEPs. Four were chosen from the low and high response groups and five were chosen from the mid response group (Table 5.3). In order to remove the effects of stray light from neighboring FZP lenses we subtracted the mean of the low response group from the resonators in the mid and high response groups. We present results for those with and without the mean subtracted.

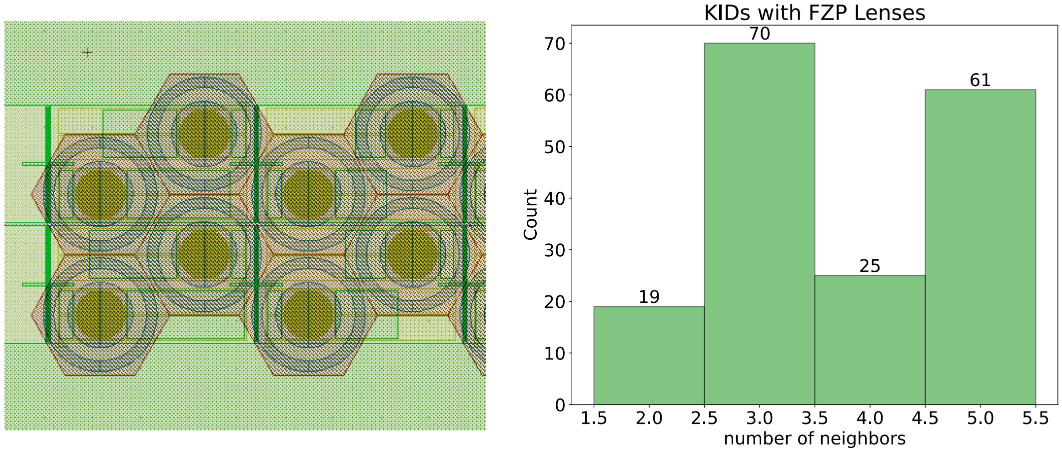

Figure 5.14: *Left*:A section of the FZP pixel layout. *Right*: A a histogram showing how many of the designed number of resonators that are coupled to FZP lenses have either 2, 3, 4 or 5 neighboring FZP lenses.

# of neighbors	# of resonators from design	Estimated # of len-coupled resonators
2	19	17
3	70	60
4	25	22
5	61	52

Table 5.2: First Column: The number of FZP lenses that can be neighboring a KID on the array. Second Column: The number of design resonators that are coupled to lenses that would have "x" amount of neighbors. Third Column: The expected number of resonators from the 168 resonators coupled to lenses that would have "x" amount of neighbors.

Low (MHz)	Mid (MHz)	High (MHz)
280.47	210.84	254.01
313.31	232.85	360.70
370.33	351.02	496.90
464.98	377.48	507.76
	476.58	

Table 5.3: Resonant frequencies chosen from each response group.

5.3.2.1 Responsivities (R_x)

In order to calculate the responsivity of the prototype array we need to determine the amount of blackbody power absorbed ($P_{BB,abs}$) by the detectors. The absorbed power is found by taking the following integral over a given wavelength range

$$P_{BB,abs} = A_{pixel}\Omega\eta_{opt}\eta_{abs}\int_{\lambda_i}^{\lambda_f}\frac{B(\lambda,T)}{2}F_\lambda\,d\lambda, \tag{5.2}$$

where $B(\lambda,T)$ is Planck's law for blackbody radiation,

$$B(\lambda,T) = \frac{2hc^2}{\lambda^5}\frac{1}{e^{hc/(\lambda k_B T_{BB})}-1}, \tag{5.3}$$

and is divided by two, because the inductor efficiently absorbs only one polarization of radiation. The area of the FZP lens is $A_{pixel} = 0.044$ mm^2, Ω is the solid angle subtended by the blackbody onto the FZP lens, F_λ is the transmission of the filter stacks as a function of wavelength, and η_{opt} is composed of different constant optical efficiencies that effect the optical load. The optical efficiencies are listed in Table 5.4. The efficiency at which the detector absorbs optical power is $\eta_{abs} = 0.77$ [2] . The solid angle (Ω) is calculated using the following expression

$$\Omega = \frac{A_{apt}}{L^2}, \tag{5.4}$$

where $A_{apt} = 19.63$ mm^2 is the area of the blackbody aperture and $L = 75.184$ mm is the distance from the blackbody to the prototype array ($\Omega = 3.47\times10^{-3}$). Table 5.5 shows the calculated absorbed blackbody power.

Efficiency description	value
Transmission through Si-vacuum interface at Fresnel zone plate lens	0.7
Fresnel zone plate efficiency (FZP_{eff})	0.23

Table 5.4: The efficiencies that make up η_{opt} for the BEGINS prototype array optical set up.

The 12 detectors' fractional frequency response as a function $P_{BB,abs}$ were fit to both models described in Sec. 3.2. Figures 5.15, 5.16 and 5.17 show the measured fractional frequency response

[2] This was discussed through private communication with Peter Day and electromagnetically simulated

T_{BB} (K)	$P_{BB,abs}$ (pW)
6	1.45×10^{-34}
40	1.63×10^{-4}
60	1.60×10^{-2}
80	0.16
90	0.35
100	0.67

Table 5.5: Cryogenic blackbody optical power absorbed by prototype BEGINS KID array. First column: the blackbody temperature. Second Column: The calculated power absorbed by each KID on the array.

data (blue dots), Model 1 labeled as "Linear Model" fits (red dashed-dotted lines) and Model 2 labeled as "x(P)" (black line) fits to the low, mid and high response resonators, respectively. For all groups the response at 0.16 pW ($T_{BB} = 80$ K) was lower than expected when compared to the trend that the rest of the data followed, so it was excluded from the fits. This may have been due to an unstable blackbody that had not settled to 80 K.

The low response resonators closely follow a linear response with varying optical load, suggesting that the quasiparticle lifetime is not varying significantly with optical power. It is apparent from the mid response and high response groups that the data is better fit by Model 2, than the linear model (Model 1), even at low optical powers (shown in insets). The better fit to Model 2 confirms that the quasiparticle lifetime changes with absorbed optical power. As the absorbed optical power increases the quasiparticle density increases and increases the likelihood of quasiparticles recombining, shortening the quasiparticle lifetime. The estimated parameters ($R_{x,0}$ and P_0) from Model 2 are used to calculate the responsivity as a function of absorbed power, as expressed in Eq. 3.52.

Fig. 5.18 shows the responsivity as a function of absorbed power for the low, mid and high response groups. The responsivity curve exhibits a roll-off at a high absorbed optical power, fit by the parameter P_0. The mid and high response groups roll-off powers are in the range 0.6 to 1.2 pW. The locations of the roll-off powers for the low response group are more variable between detectors. Two of the resonators have a roll-off located at particularly high power, $\sim$ 100 pW, providing further evidence that they belong to the dark group and may be close to the edge of the array. The other two resonators have higher responsivity, but still not as responsive as those in the mid and high response groups. These resonators could be dark or resonators with defects leading to a low response.

The same analysis was performed on the mid and high response groups with the mean of the low response group subtracted from them. Fig. 5.19, shows the mid and high response groups responsivity results for this analysis. As expected, the estimated responsivity is reduced when the low response mean power is subtracted. In Sec. 5.3.5, the responsivities from the original data and the data with the low response mean subtracted will be used to calculate the NEPs of the prototype array.

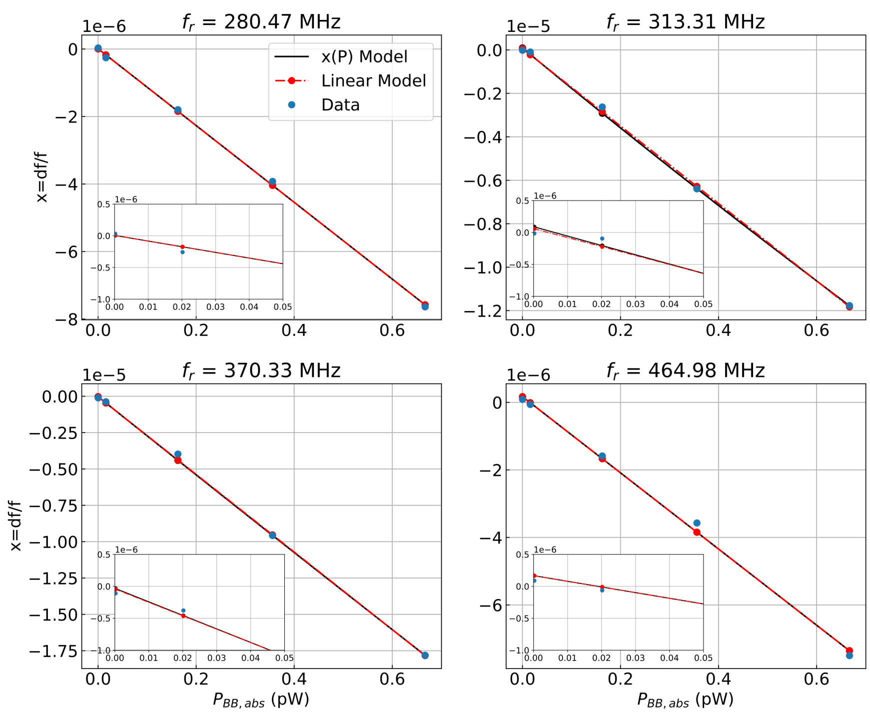

Figure 5.15: Fractional frequency response as a function of power of the low response resonators. Blue Dots: Data. Red Dashed Line: Linear fit to data. Black Line: Model from Eq. 3.52 fit to data.

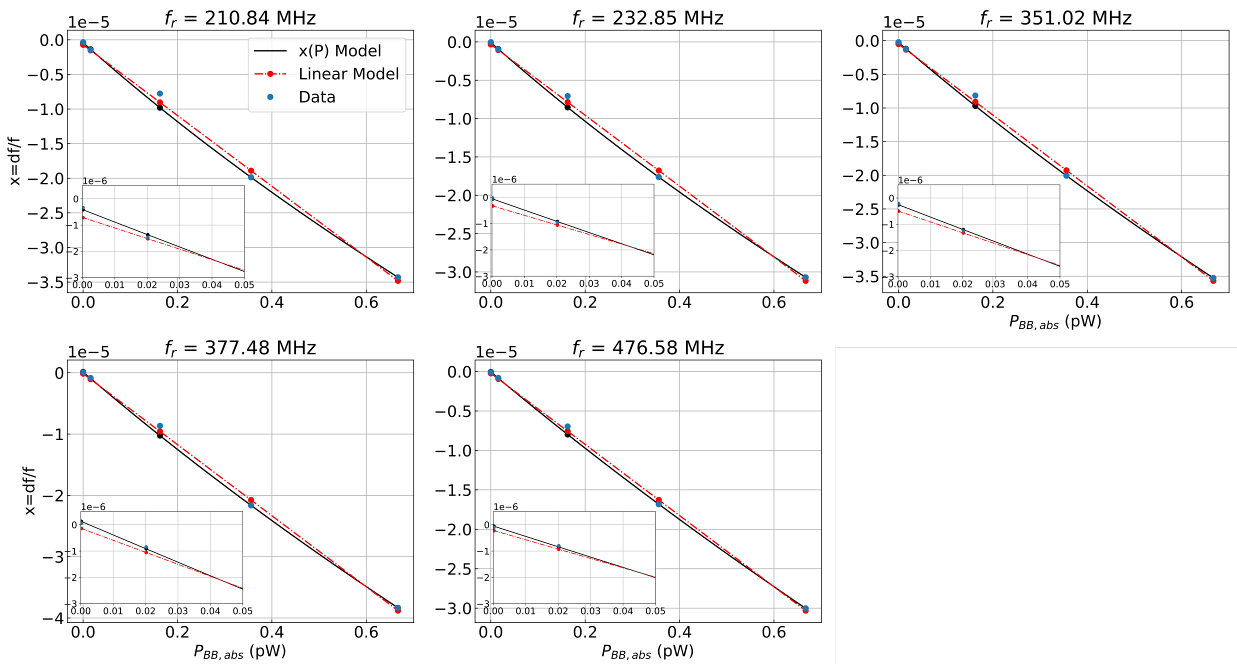

Figure 5.16: Fractional frequency response as a function of power of the mid response resonators. Blue Dots: Data. Red Dashed Line: Linear fit to data. Black Line: Model from Eq. 3.52 fit to data. The model labeled x(P), fits the data better when compared to the linear model.

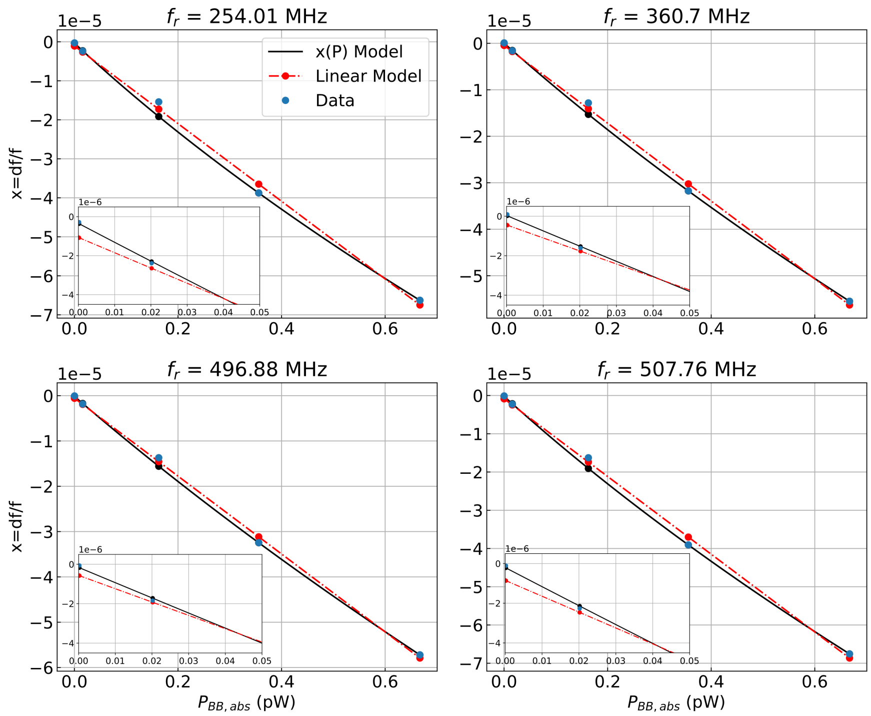

Figure 5.17: Fractional frequency response as a function of power of the High response resonators. Blue Dots: Data. Red Dashed Line: Linear fit to data. Black Line: Model from Eq. 3.52 fit to data. The model labeled x(P), fits the data better when compared to the linear model.

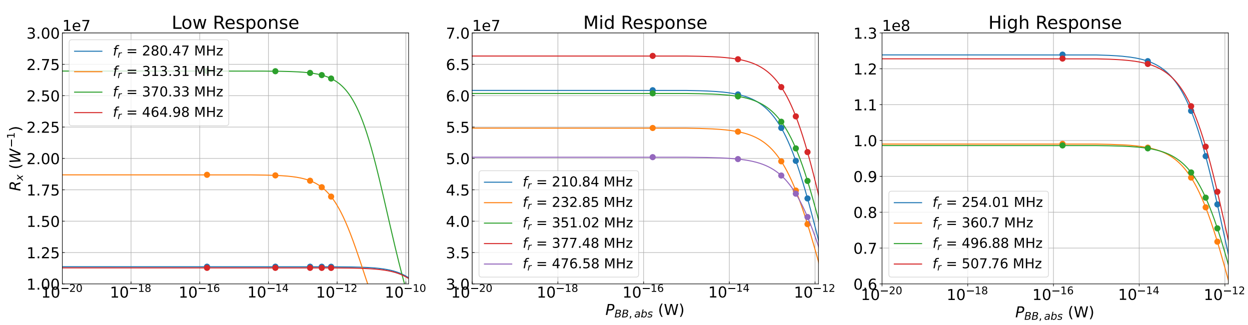

Figure 5.18: *Left*: Responsivity as a function of power for all low response resonators. Across all resonators the low response responsivity varies from $\sim 1.1 \times 10^7 - 2.7 \times 10^7$ W^{-1}. *Middle*: Responsivity as a function of power for all mid response resonators. Across all resonators the mid response responsivity varies from $\sim 4.0 \times 10^7 - 6.6 \times 10^7$ W^{-1}. *Right*: Responsivity as a function of power for all high response resonators. Across all resonators the high response responsivity varies from $\sim 7.2 \times 10^7 - 1.2 \times 10^8$ W^{-1}.

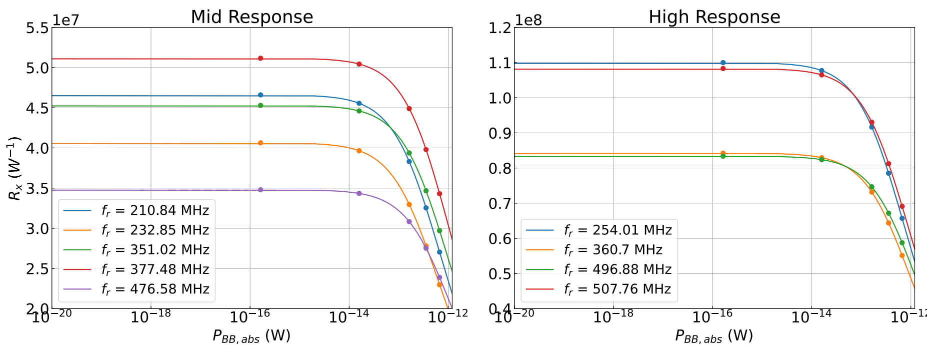

Figure 5.19: Responsivity as a function of power for the mid and high response groups with the mean of the low response group subtracted out. The mid response group now has a responsivity ranging from $\sim 2.3 \times 10^7 - 5.1 \times 10^7 W^{-1}$ and the high response ranges from $\sim 5.5 \times 10^7 - 1.1 \times 10^8 W^{-1}$.

5.3.3 Measurement Results: Noise PSDs S_{xx}

Here I discuss the results of on-resonance single-tone noise measurements of the 12 resonators using the measurement method discussed in Sec. 4.2. The power spectral density (PSDs) of the noise measurements allow us to calculate NEPs, estimate TLS noise (S_{TLS}), white noise (S_{WN}) and τ_{qp} of the KIDs. The PSDs of the three response groups are shown in figures 5.20, 5.21, and 5.22 in S_{xx} units of Hz^{-1}. The PSDs are plotted for each blackbody temperature from 6 to 100 K in the frequency/phase (solid lines) and dissipation/amplitude (dashed lines) directions. The frequency noise corresponds to fluctuations in the resonance frequency and the dissipation noise corresponds to fluctuations in the amplitude of the total quality factor.

All PSDs show 1/f noise in both noise directions with a knee ∼10 Hz. The 1/f noise can result from slow fluctuations in the detector temperature, slow fluctuations in the blackbody temperature or the readout system. However, in the frequency direction the most dominant 1/f noise contribution is TLS noise [104]. The amount of TLS noise in the detectors will determine whether we achieve the NEPs necessary for BEGINS. In both noise directions there is a roll off at at 27 kHz that results from lowpass filters in the readout electronics. The separation in amplitude between the noise directions indicates that the fundamental detector noise sources dominate over readout and low noise amplifier (LNA) noise (discussed in Sec. 4.2). This is important because if the noise is dominated by the system noise we cannot extract the sensitivity of the detector.

The mid and high response PSDs in the frequency direction increase in amplitude and flatten from ∼10 Hz to ∼ 1 kHz with increasing blackbody temperature. This arises from an increase in white noise caused by photon noise and G-R noise and indicates that we are photon-noise limited. The low response group does not appear to be photon-noise limited. The increase in white noise is not evident until 90 K, except for $f_r = 370.33$ MHz which increases in amplitude at 80 K. If the detectors are those blocked from radiation the increase in white noise could be due to absorption of stray light or chip heating. Another important feature in the frequency noise direction is the roll-off at ∼ 1 kHz which is due to the τ_{qp} of the detectors. Short quasiparticle lifetimes can limit the responsivity of the detectors, which is further discussed in Sec. 5.3.4.

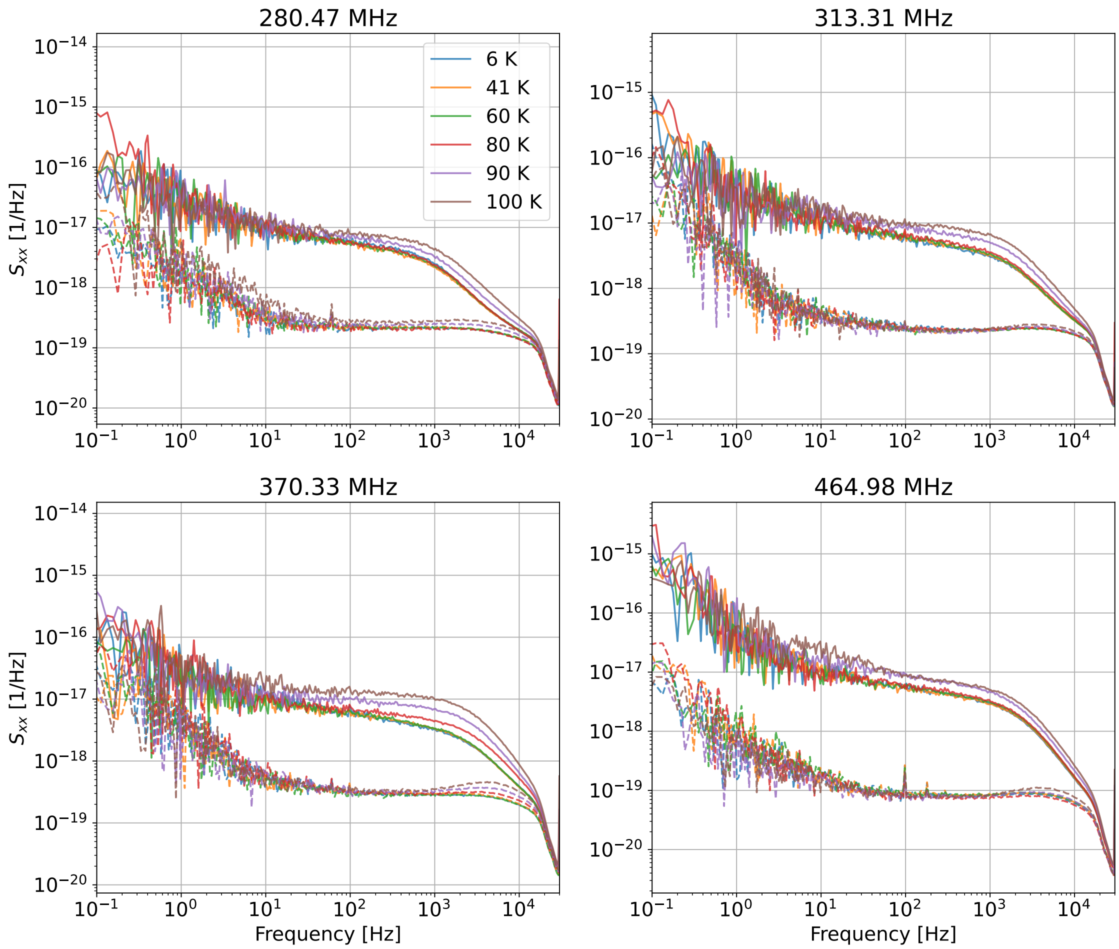

Figure 5.20: PSDs of each low response detector as a function of blackbody temperature from 6 to 100 K. The plots show both the phase (frequency) noise (solid lines) and the amplitude (dissipation) noise (dashed lines).

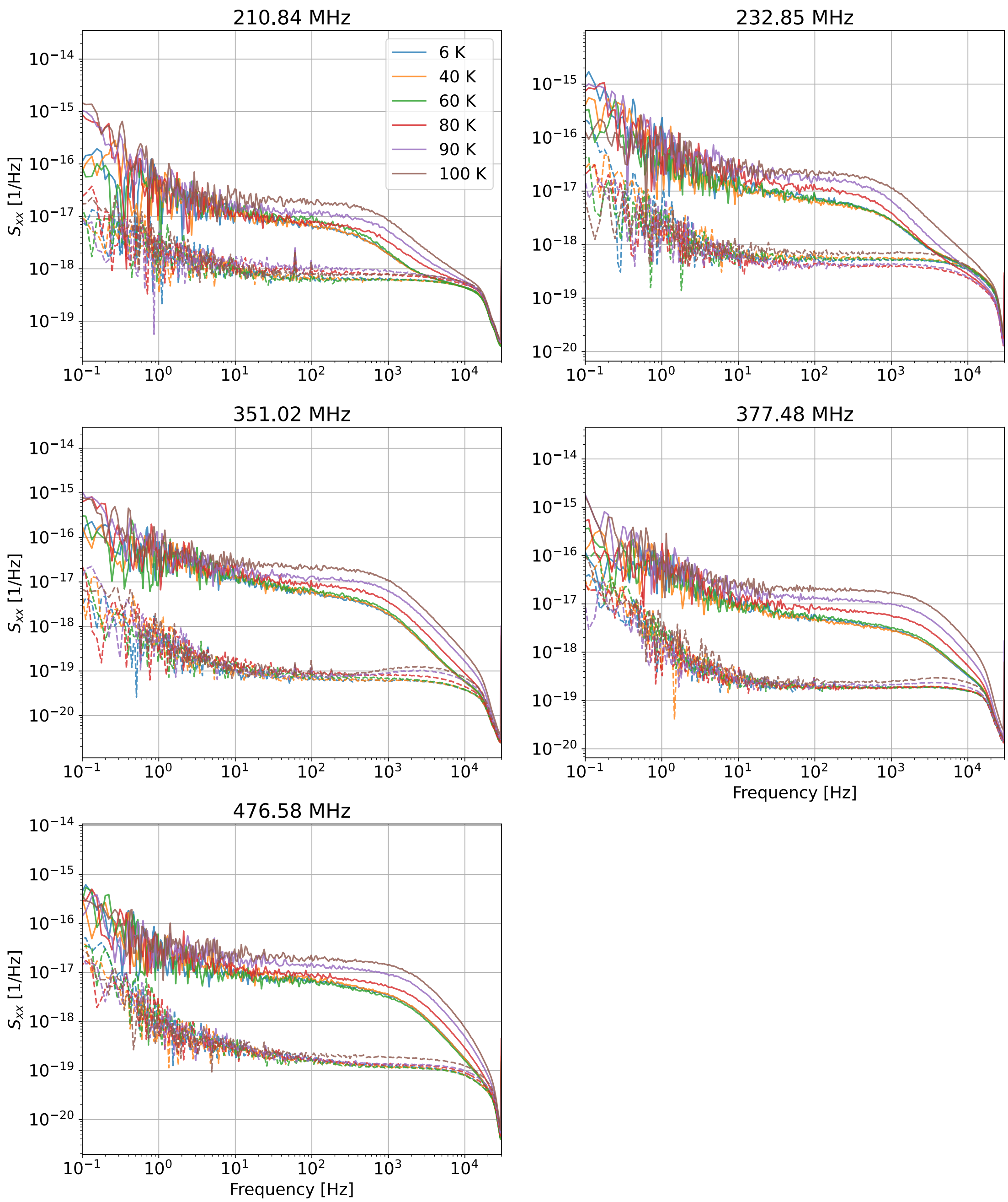

Figure 5.21: PSDs of each mid response detector as a function of blackbody temperature from 6 to 100 K. The plots show both the phase (frequency) noise (solid lines) and the amplitude (dissipation) noise (dashed lines).

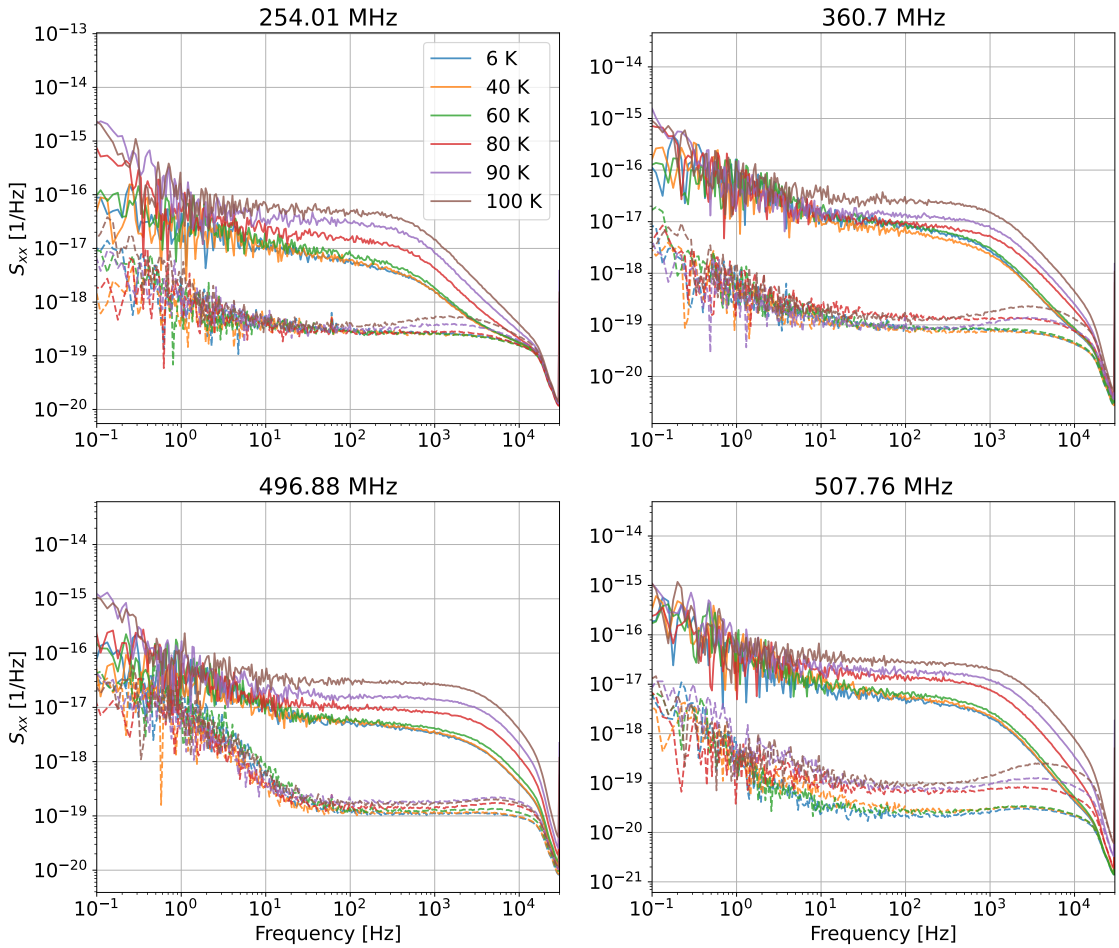

Figure 5.22: PSDs of each high detector as a function of blackbody temperature from 6 to 100 K. The plots show both the phase (frequency) noise (solid lines) and the amplitude (dissipation) noise (dashed lines).

5.3.4 Measurement Results: Fits to Noise PSDs S_{xx}

Here I discuss fits to $S_{xx,freq}$ to estimate τ_{qp}, the TLS noise level (S_{TLS}), and the white noise level (S_{WN}). τ_{qp} and S_{TLS} are particularly important because they affect the responsivity and total NEP. The responsivity is proportional to τ_{qp}, so longer lifetimes lead to a higher responsivity (Eq. 3.44), while higher TLS noise can significantly degrade noise performance. The model used to fit for these parameters is

$$S_{xx} = \frac{S_{WN}}{1 + (2\pi f \tau_{qp})^2} + S_{TLS} f^{-n}. \tag{5.5}$$

The first term is a Lorentzian with a roll-off at τ_{qp} and amplitude that depends on the white noise level. This method for fitting τ_{qp} only works if the quasiparticle lifetime is longer than the resonator ring time, $\tau_{ring} = \frac{Q_r}{\pi f_r}$, which is an intrinsic feature of LC circuits and reflects how long a resonator takes to dissipate energy. In the 12 resonators we measured, τ_{ring} was less than τ_{qp} in all resonators. The second term is used to fit for the 1/f noise level that has been shown to arise from TLS noise in KIDs [81, 57, 36]. 1/f noise from TLS has been shown to increase as 1/f$^{0.5}$ above 10 Hz [35, 80, 85]. For this reason all fits were done above 10 Hz and n was fixed to $n = 0.5$. The PSD fits are shown in figures 5.24, 5.25 and 5.26. The solid lines represent the best fit and the star markers represent the estimated τ_{qp} roll-off frequency. For some resonators the fit fails at frequencies greater than the roll-off frequency, causing the roll-off frequency to be underestimated.

Fig. 5.23, shows all three parameters fits for the low, mid and high response groups as a function of temperature. The solid black lines in the first two rows of plots are the average white noise and TLS noise, respectively. The white noise, which is composed of photon-noise and G-R noise, increases with temperature due to incident photon flux on the detector. G-R noise only increases if the chip heating occurs due to increased optical power. The TLS noise does not follow a clear trend with increasing optical power, and ranges from $\sim 1 \times 10^{-17}$ to 5×10^{-17} Hz^{-1}. TLS noise has been observed to scale with drive power and bath temperature, which are held constant in these measurements [35, 80]. The estimated TLS noise level is comparable to values measured in aluminum and niobium KIDs with IDCs by Z. Pan, et al [85], who studied how TLS noise varies with IDC gap width. At a drive power near the drive power of the BEGINS resonators (>-93 dBm) the TLS noise in their IDC KIDs varied from 1.5×10^{-17} to 4×10^{-17} Hz^{-1}. Our prototype BEGINS resonators with PPCs therefore did not decrease the TLS noise compared to those with IDCs as we predicted, but they are still a promising design choice for KIDs that enable smaller pixels.

The last row in Fig. 5.23 shows the estimated quasiparticle lifetime (τ_{qp}) as a function of blackbody temperature. It varies from 59-171 μs, 53-315 μs, and 38-315 μs in the low, mid and high response groups, respectively. The τ_{qp} for different TiN KIDs in the literature has been estimated to range from 10-300 μs [25, 58, 104]. P. Diener et al. also observed surprisingly long quasiparticle lifetimes in a few of the TiN KIDs they characterized, up to 5.6 ms [25]. They conjectured that the large variation in τ_{qp} may have arisen from the dependence of superconducting properties with TiN stoichiometry. Although the variations in the lifetimes in our prototype array are not as drastic, this same mechanism may be responsible. In any case, we cannot depend on longer τ_{qp} to increase the responsivity to meet the BEGINS sensitivity requirements.

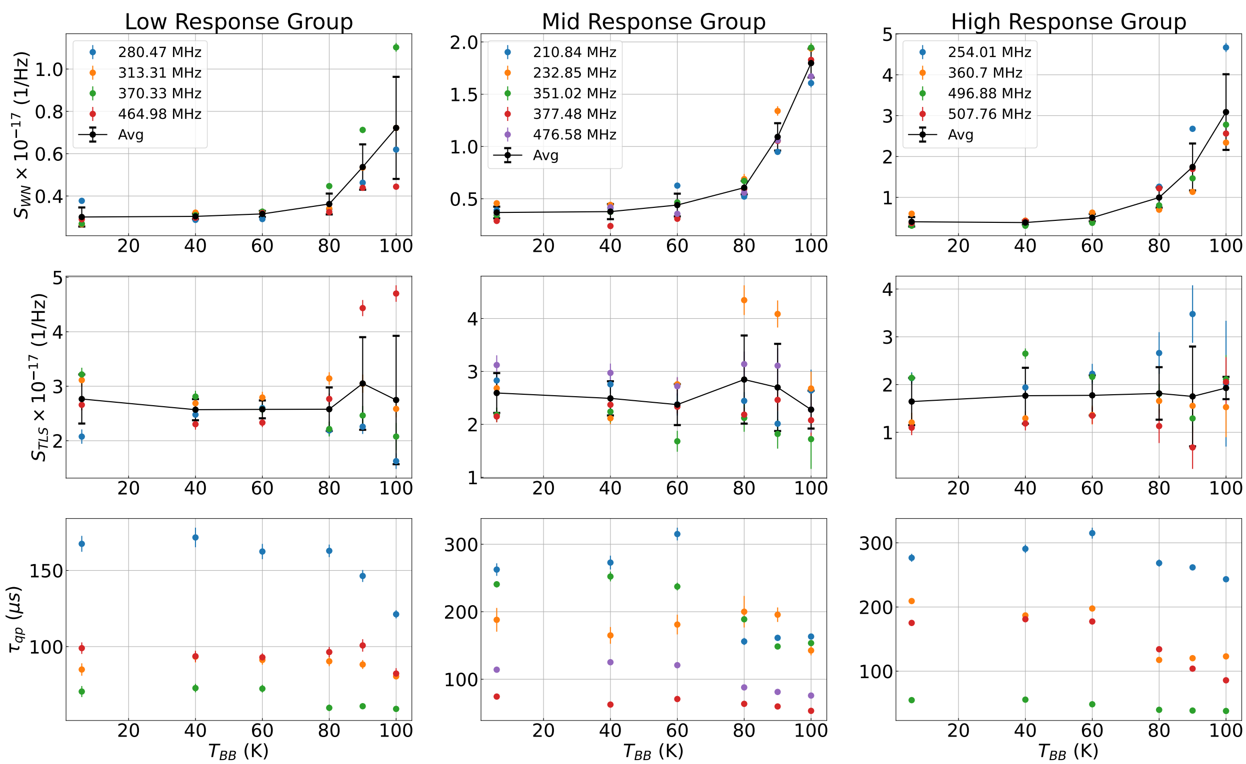

Figure 5.23: All three parameters (S_{WN}, S_{TLS}, τ_{qp}) fits for the low, mid and high response groups as a function of temperature. The solid black lines in the first two rows of plots are the average white noise and TLS noise levels over all resonators in their corresponding response group. The error bars are calculated from the standard deviation of the fits.

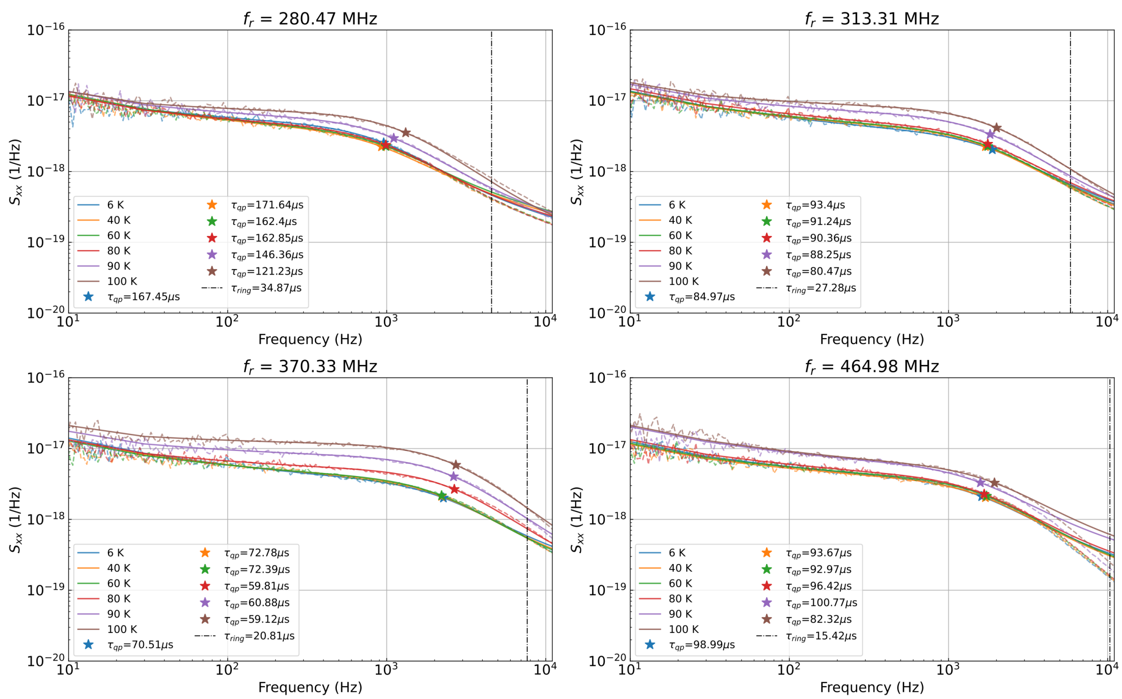

Figure 5.24: Low Response group S_{xx} fits. The dashed line is the measured S_{xx}. The solid line is the fit using Eq. 5.5. The stars represent where the roll-off τ_{qp} was estimated to be. The black dash dotted line is the the resonator ring time, $\tau_{ring} = \frac{Q_r}{\pi f_r}$. The resonator ring time is an intrinsic feature of LC circuits and reflects how long a resonator takes to dissipate energy.

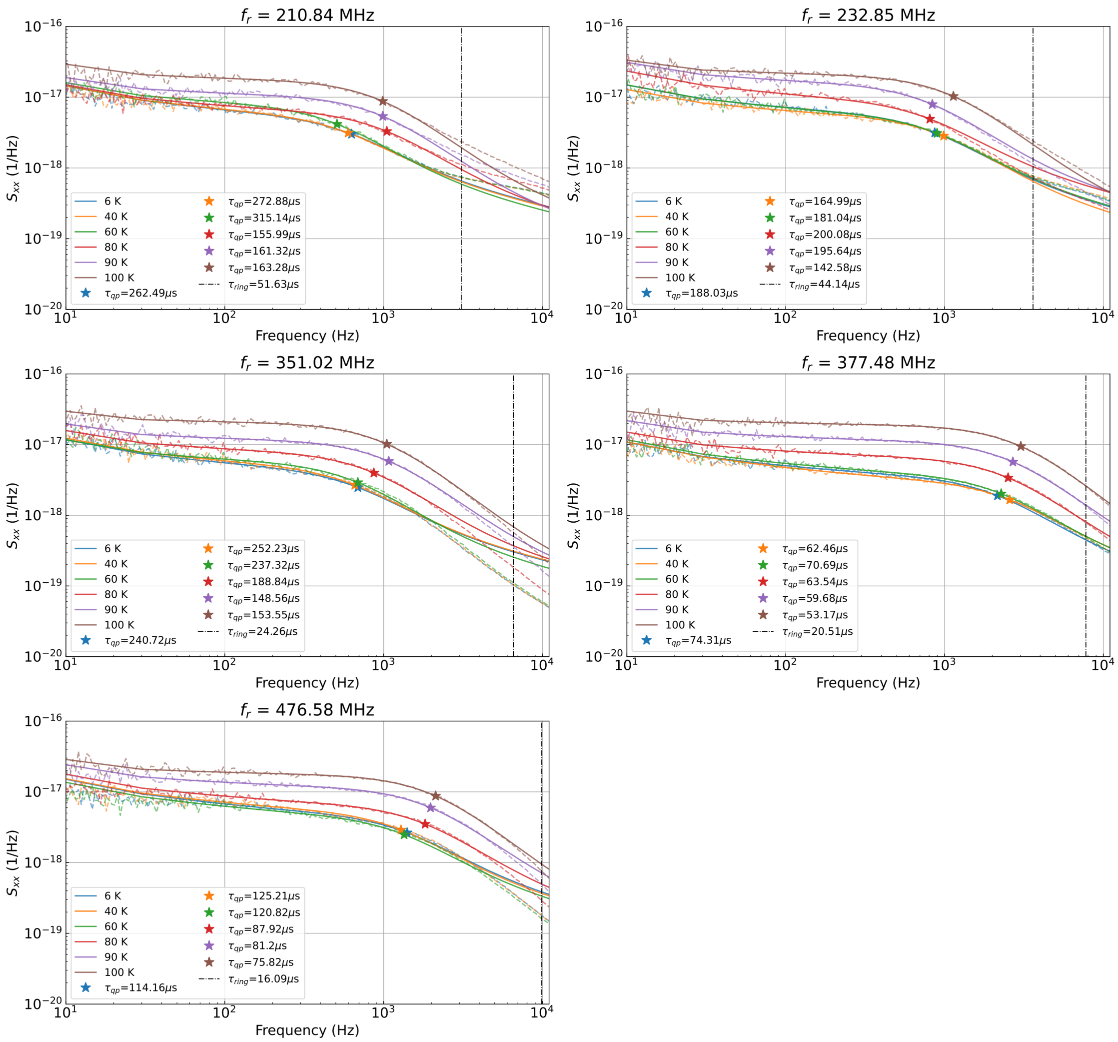

Figure 5.25: Mid Response group S_{xx} fits. The dashed line is the measured S_{xx}. The solid line is the fit using Eq. 5.5. The stars represent where the roll-off τ_{qp} was estimated to be. The black dash dotted line is the the resonator ring time, $\tau_{ring} = \frac{Q_r}{\pi f_r}$. The resonator ring time is an intrinsic feature of LC circuits and reflects how long a resonator takes to dissipate energy.

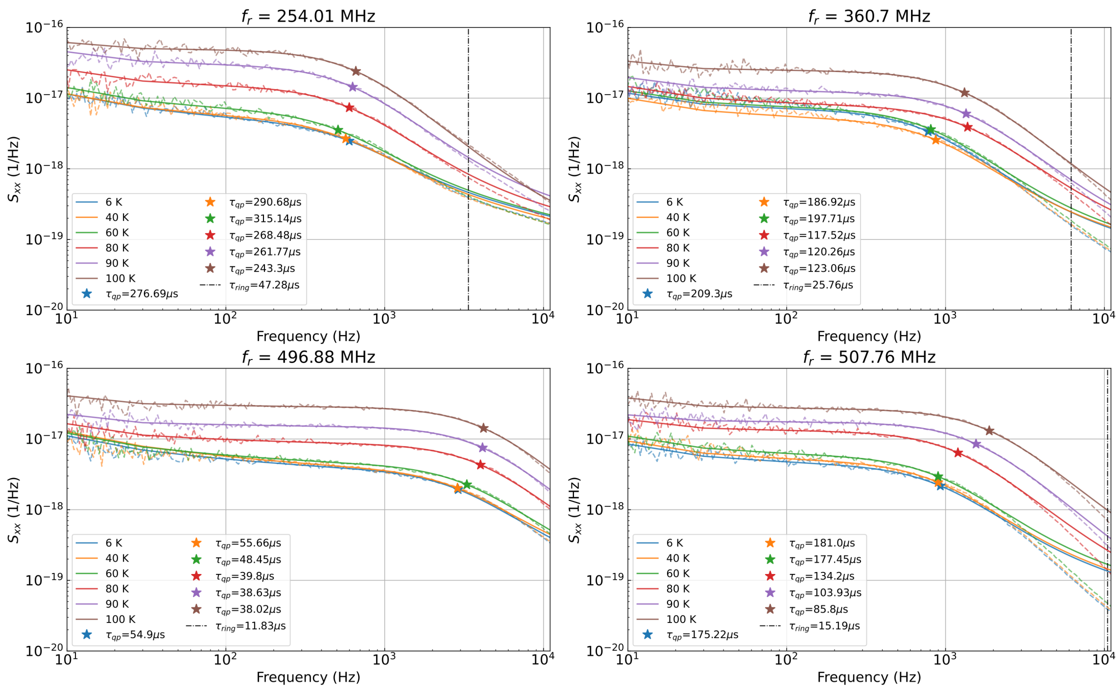

Figure 5.26: High Response group S_{xx} fits. The dashed line is the measured S_{xx}. The solid line is the fit using Eq. 5.5. The stars represent where the roll-off τ_{qp} was estimated to be. The black dash dotted line is the the resonator ring time, $\tau_{ring} = \frac{Q_r}{\pi f_r}$. The resonator ring time is an intrinsic feature of LC circuits and reflects how long a resonator takes to dissipate energy.

5.3.5 Measurement Results: Empirical NEPs

Here I calculate the empirical NEPs of the 12 resonators to determine if we reach the BEGINS sensitivity requirement. I also investigate the anomalously high power detected by the high response group, which we found to be ~ 1.8 times more than expected. NEPs are calculated in the frequency direction (NEP_{freq}), because the detector noise is dominant in that direction. The frequency noise PSD ($S_{xx,freq}$) is combined with the responsivity (R_x) to determine the empirical NEP as a function of absorbed blackbody power, where $NEP_{freq} = \sqrt{S_{xx,freq}}/R_x$. The calculations are done at 1 Hz, 10 Hz and 100 Hz for each PSD shown in Sec. 5.3.3. The BEGINS instrument modulation rate places the astronomical signal of interest in the 1-10 Hz range, so we are most interested in characterizing the NEP at these audio frequencies. However, most of the detectors exhibit TLS noise at those frequencies, so we chose to also erform the calculations at 100 Hz where most of the detectors are photon-noise limited.

Fig. 5.27 shows the results for the low, mid and high response detectors (left panel) and with the low response mean subtracted out (right panel). The different line styles represent the frequency that the NEP was calculated; either at 1 Hz (dotted line), 10 Hz (dashed line), or 100 Hz (solid line). The different markers and colored lines are used to distinguish between the resonators (legend at top of left panel). The solid gray line represents the cryogenic blackbody photon-noise, $NEP_{BB,ph} = \sqrt{2P_{BB,abs}h\nu_{ph}(1+n_0)}$, the teal dotted dashed line represents the expected BEGINS photon noise NEP at 25 μm for our optical set up, which is expected to be 7.58×10^{-17} W/$\sqrt{\text{Hz}}$ for an absorbed power of 0.36 pW. The BEGINS absorbed power is then calculated by taking the expected BEGINS incident optical load at the focal plane for 25 μm wavelength and applying the efficiencies from our optical set up (η_{opt} and η_{abs}).The black lines are the average measured NEPs of all resonators at 1 Hz, 10 Hz, and 100 Hz, which are are listed in tables 5.6, 5.7, and 5.8.

NEP_{freq} should be equivalent to $NEP_{BB,ph}$ if optical and detector absorption efficiencies are correct and the detectors are photon-noise limited. However, the asymptotic behavior at high optical loads indicate that the detectors are only photon-noise limited down to 210 fW. At 1 Hz the detectors are dominated by TLS noise, so none of them follow $NEP_{BB,ph}$. None of the low response group follow $NEP_{BB,ph}$ because the detector optical efficiency is less than the expected η_{opt}. The opposite occurs with the high response group at 10 Hz and 100 Hz, where NEP_{freq} falls below $NEP_{BB,ph}$. This demonstrates that the high response group is detecting extra radiation, possibly from the five neighboring FZP lenses, that results in the overestimation of detector sensitivity. The average of the mid response group in the left panel at 100 Hz appears to be photon-noise limited, so we take this group as representative of the true sensitivity of the detectors. The BEGINS NEP requirement is met at 100 Hz, but at 10 Hz the average mid response NEP is 9.2×10^{-17} W/$\sqrt{\text{Hz}}$, 1.2 times larger than the BEGINS NEP requirement. The NEP can be reduced by increasing the quasiparticle lifetime τ_{qp}, decreasing the band gap energy Δ_0 or reducing the volume of the inductor which increases responsivity R_x.

The plots in the right panel of Fig. 5.27 show the mid and high response groups with the low response mean subtracted. Neither group falls along the $NEP_{BB,photon}$ line at high optical powers. The high response group still shows indication of an inflated response from extra radiation. The mid response group is now less sensitive. This either means the optical efficiency estimate is incorrect and/or the low response mean overestimates the response from extra radiation. The latter could be the case if the measured low response group contains more resonators with five neighboring FZP lenses than the mid response group (which we hypothesize to have 2, 3 or 4 neighboring lenses). Due to the uncertainty in this method we place low confidence in the estimated NEPs.

If we assume the original mid response group represents the true detector sensitivity then the KIDs are a factor of 1.2 above the BEGINS NEP requirement at 25 μm wavelength. To improve the NEP the next fabricated BEGINS KID array will have inductors with smaller volumes and higher absorption efficiency. It will also be coupled to a microlens array. Results of optical tests on a KID array successfully bonded to a microlens array chip are discussed in Ch. 7. The microlens array shown no indication that extra radiation from neighboring lenses is being absorbed. This will improve the NEPs, decrease the scatter in its value across the array, and confirm if we have correctly quantified all absorber and optical efficiencies.

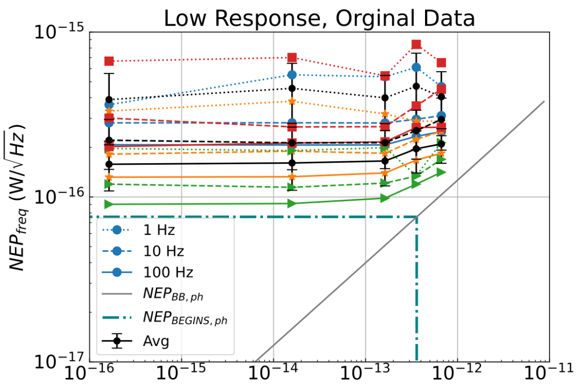

Symbol	Low (MHz)	Mid (MHz)	High (MHz)
● (blue circle)	280.47	210.84	254.01
★ (orange star)	313.31	232.85	360.70
▶ (green triangle)	370.33	351.02	496.90
■ (red square)	464.98	377.48	507.76
◆ (purple diamond)		476.58	

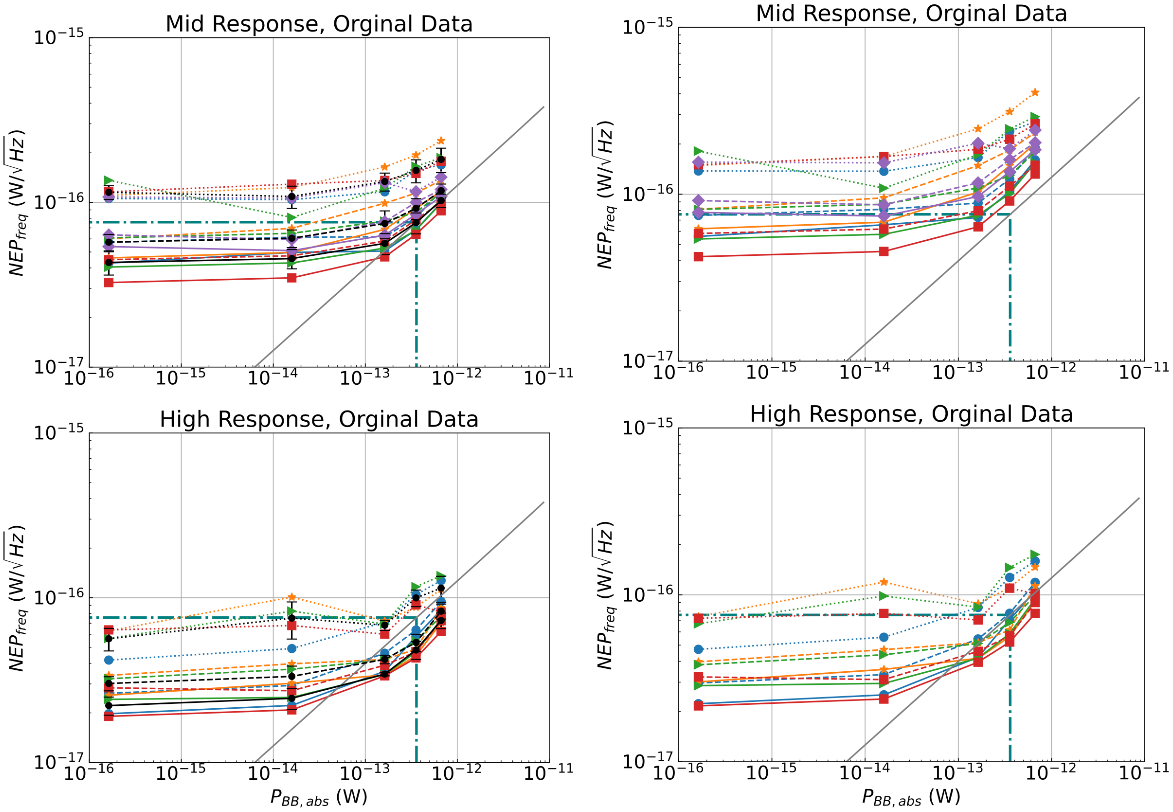

Figure 5.27: NEPs for the unaltered original data for the low, mid and high response detectors and the results for the mid and high response detectors with the low response mean subtracted out. The different line styles represent the audio frequency where the NEP was calculated; either at 1 Hz (dotted line), 10 Hz (dashed line), or 100 Hz (solid line). The markers and color represent the specific detector from each group, as described in the legend at the top right of the figure. The solid gray line represents the cryogenic blackbody photon noise NEP, where $NEP_{BB,ph} = \sqrt{2P_{BB,abs}h\nu_{ph}(1+n_0)}$. The teal dotted dashed line represents the expected BEGINS photon noise NEP at 25 μm, which is expected to be 7.58×10^{-17} W/$\sqrt{\text{Hz}}$ for an absorbed power of 0.36 pW. The black lines are the average NEPs of all resonators at 1 Hz, 10 Hz, and 100 Hz.

$P_{BB,abs}$ (pW)	1 Hz, (10^{-16} $W/\sqrt{Hz}$)	10 Hz, (10^{-16} $W/\sqrt{Hz}$)	100 Hz, (10^{-16} $W/\sqrt{Hz}$)
1.63×10^{-4}	4.0±1.7	2.2±0.7	1.6±0.5
1.60×10^{-2}	4.6±2.0	2.1±0.7	1.6±0.5
0.16	4.0±1.5	2.1±0.6	1.7±0.5
0.35	4.7±2.8	2.5±0.8	2.0±0.6
0.67	4.1±1.7	3.0±1.0	2.1±0.5

Table 5.6: Low Response average NEPs at 1 Hz, 10 Hz and 100 Hz of original response data from fig. 5.27.

$P_{BB,abs}$ (pW)	1 Hz, (10^{-17} $W/\sqrt{Hz}$)	10 Hz, (10^{-17} $W/\sqrt{Hz}$)	100 Hz, (10^{-17} $W/\sqrt{Hz}$)
1.63×10^{-4}	11.5±1.1	5.7±0.7	4.3±0.7
1.60×10^{-2}	10.9±1.7	6.1±0.7	4.6±0.6
0.16	13.4±1.7	7.4±1.4	5.6±0.8
0.35	15.6±2.5	9.2±1.3	7.5±1.1
0.67	18.2±3.1	11.8±1.1	10.3±1.0

Table 5.7: Mid Response average NEPs at 1 Hz, 10 Hz and 100 Hz of original response data from fig. 5.27.

$P_{BB,abs}$ (pW)	1 Hz, (10^{-17} $W/\sqrt{Hz}$)	10 Hz, (10^{-17} $W/\sqrt{Hz}$)	100 Hz, (10^{-17} $W/\sqrt{Hz}$)
1.63×10^{-4}	5.6±1.0	3.0±0.3	2.2±0.3
1.60×10^{-2}	7.5±2.0	3.3±0.5	2.5±0.4
0.16	6.8±0.5	4.2±0.3	3.4±0.1
0.35	10.0±1.2	5.4±0.7	4.8±0.6
0.67	11.4±2.1	8.3±0.9	7.3±0.8

Table 5.8: High Response average NEPs at 1 Hz, 10 Hz and 100 Hz of original response data from fig. 5.27.

We also investigated the amount of extra power absorbed by the high response group from the original data. This is done by scaling NEP_{freq} at 0.67 pW for $f_r = 507.76$ MHz at 100 Hz (solid red line in fig. 5.27 Bottom Left) to equal $NEP_{BB,ph}$. This required a scaling factor of 0.60. The scaled high response NEPs are shown in the left plot of Fig. 5.28. We must also adjust the responsivities, using $R_x = \sqrt{S_{xx,freq}}/NEP_{freq}$ (Fig. 5.28 Right), and the absorbed power, $P_{BB,abs} = x/R_x$ ($x = df/f$, the fractional frequency response). The results are shown in table 5.9. The first columns is the blackbody temperature, the second column is the new estimated average absorbed power of the scaled high response resonators and the last column lists by what factors the expected absorbed power increased (labeled as an efficiency). The efficiency is similar from 60 to 100 K with an average of 1.8. At 40 K the efficiency increases by a factor of 6.7. This could explain why we see the NEP saturate to a constant value towards the lowest absorbed power in Fig. 5.27 for all detectors. J. Hubmayr, et al. saw this in there measurements on TiN KIDs, as well [47]. They hypothesized that it was due to stray light in their cryostat. This possibility is discussed further in sec. 5.3.6, where we compare the empirical NEPs to the expected NEPs derived from the sensitivity model in Sec. 3.3. Due to timing and other projects we were not able to test this theory by improving the light-tightness of our testbed.

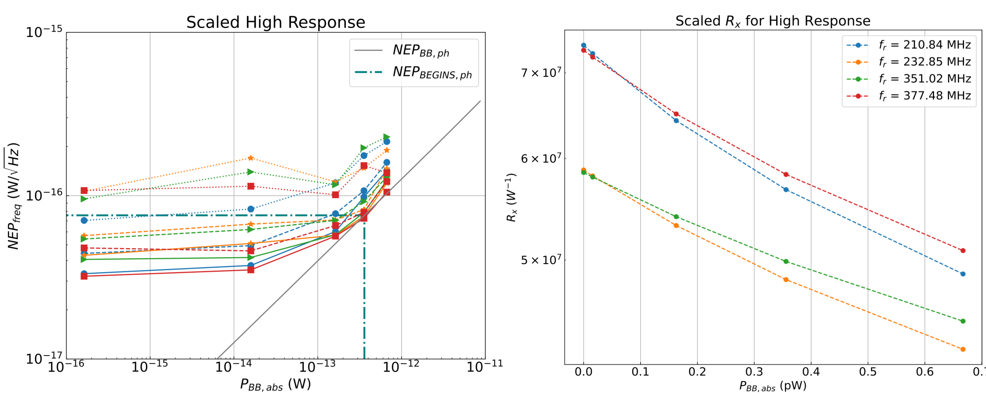

Figure 5.28: *Left*: Scaled high response NEPs, such that the NEP at 100 Hz for the resonator at 507.76 MHz (solid red line in fig. 5.27 *Bottom Left*: followed the $NEP_{BB,photon}$ line. This required a scaling factor of 0.52. Factor was applied to all the high response NEPs. *Right*: Responsivities calculated from the scaled NEPs, using $R_x = \sqrt{S_{xx}}/NEP_{freq}$. The calculated responsivities are plotted as a function of power.

BB Temp (K)	New Estimated Absorbed $P_{BB,abs}$ (pW)	High Response Detector Efficiency
40	2.00×10^{-3}	12.14
60	3.1×10^{-2}	1.9
80	0.246	1.5
90	0.665	1.9
100	1.317	2.0

Table 5.9: First Column: The blackbody temperature. Second Column: The estimated average absorbed power of the high response resonators after scaling the NEPs. Third Column: Shows how much more power was absorbed when compared to the calculated absorbed power in table 5.5.

5.3.6 BEGINS KIDs Expected NEP vs Empirical NEP

We can use measured parameters from the BEGINS prototype array to calculate the theoretical NEPs that contribute to the total NEP (NEP_{tot}) with the method described in Sec. 3.4 and compare this to the empirical NEPs calculated in Sec 5.3.5. We chose the resonator with $f_r = 476.58$ MHz for this comparison because at high optical loading it falls along the $NEP_{BB,ph}$ line. The total NEP is calculated by adding all NEP contributions in quadrature, $NEP_{tot}^2 = NEP_{TLS}^2 + NEP_{amp}^2 + NEP_{photon}^2 + NEP_{GR}^2$. Table 5.10, lists the parameters required to determine the NEPs, their values and the source or reference to literature of the value. The following parameters were determined from the dark and optical measurements discussed in the chapter: f_r, $Q_{i,0}$, Q_c, τ_{qp}, α, T_c, and S_{TLS}. The parameter η_a, the quasiparticle pair-breaking efficiency of the absorbed drive power, is not well-known. It has been measured to be as low at 0.001 and as high as 0.5 with a dependence on the resonant frequency [44, 80]. We chose to implement both extreme values to calculate the NEPs.

Fig. 5.29, shows the expected NEPs. The left plots has $\eta_a = 0.001$ and the right plot has $\eta_a = 0.5$. The pink squares are the measured NEP at 100 Hz and the brown squares are the measured NEP at 10 Hz for the mid response resonator, $f_r = 476.58$ MHz. Both are photon-noise limited above 0.2 pW. Below 0.2 pW they saturate to a constant NEP that is dominated by G-R and TLS noise for $\eta_a = 0.001$ and G-R, TLS, microwave power and amplifier noise for $\eta_a = 0.5$. While the increase in η_a increases NEP_{tot} by a factor of 1.5 it is still below the empirical NEPs.

Table 5.10: Input Parameters for BEGINS KIDs Expected NEPs

Symbol	Parameter	Value	Source
f_r	resonant freq	476.58 MHz	measured
ν	optical freq	12.5 THz	known
$Q_{i,0}$	Internal quality factor	6×10^4	average estimated
Q_c	Coupling quality factor	7×10^4	average estimated
χ_g	generator efficiency	1	[108]
η_{pb}	Pair-breaking efficiency	0.57	[44]
τ_0	characteristic electron-phonon interaction time	13 μs	[52]
τ_{max}	max lifetime	100 μs	[58]
V	Inductor volume	110 μm^3	calculated
η_a	qp breaking Readout efficiency	.001/.5	[44]
α	Kinetic inductance fraction	0.23	estimated
T_c	critical temperature	1.43 K	estimated
T_{oper}	bath temp	326 mK	known
S_{TLS}	TLS noise	2.55e-17 Hz^{-1}	average estimated
P_g	Drive power	4.7 pW	known

At low powers the empirical NEPs saturate to 5.1×10^{-17} W/$\sqrt{\text{Hz}}$. They are a factor of 4.6 and 2.5 greater than $\eta_a = 0.001$ and $\eta_a = 0.5$, respectively. This could be due to stray light in the cryostat or stray light from neighboring FZP lenses not captured by the model or the model is underestimating NEP_{tot}.

Parameters predicted by the sensitivity model include R_x. The model predicts an R_x that is about one order of magnitude greater than the estimated R_x from measurements. This paired with the values gathered from the literature such as η_{pb}, τ_{max}, and τ_0 create uncertainty in the model. This is apparent with NEP_{TLS} which is inversely proportional to R_x, according to Eq. 3.60. The predicted R_x by the model underestimates NEP_{TLS} compared to measurements. Despite the uncertainty, the model is still a useful tool when designing KIDs for high R_x and estimating the optical power at which the KID is no longer photon-noise limited.

5.4 Discussion

In this chapter I presented the results of dark and optical measurements made on a 25 μm BEGINS KID prototype array coupled to FZP lenses. The goal of this work was to determine if the

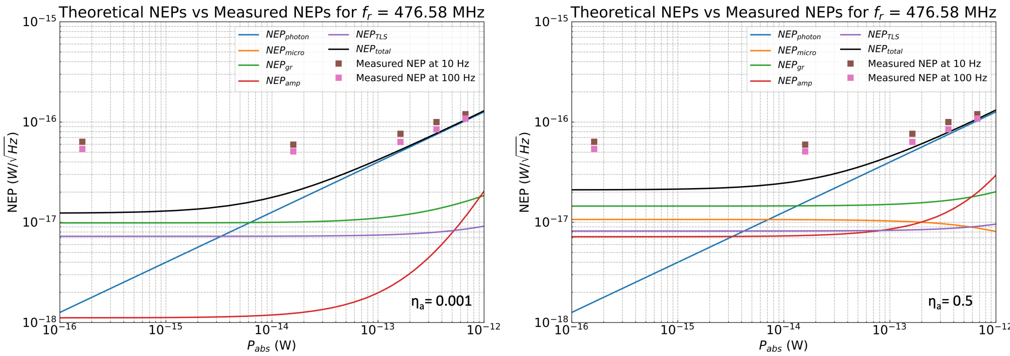

Figure 5.29: The expected NEPs and measured NEPs for f_r = 476.58 MHz. The left plot has $\eta_a = 0.001$ and the right plot has $\eta_a = 0.5$. The pink squares are the measured NEP at 100 Hz for the mid response resonator, f_r = 476.58 MHz. The brown squares are the measured NEP at 10 Hz for the same mid response resonator, f_r = 476.58 MHz.

BEGINS NEP requirement was met by the prototype detector array in a laboratory environment. The NEP requirement in our optical set up was 7.6×10^{-17} W/$\sqrt{\text{Hz}}$ for an absorbed optical power of 0.36 pW. We measured an empirical NEP of 9.2×10^{-17} W/$\sqrt{\text{Hz}}$, a factor of 1.2 above the requirement. Below I will highlight results from the dark and optical measurements and their importance towards this work and KID modeling.

Dark measurements on the prototype array indicate that $T_c = 1.43 \pm .008$ and $\alpha = 0.23 \pm .008$. The critical temperature was within the expected range of 1 K to 1.5 K. However, α was lower than expected for TiN KIDs. The low value of α will decrease the responsivity of a KID. The kinetic inductance of a KID is proportional to the sheet resistance of the KID material, by $L_{ki} = \frac{\hbar R_s}{\pi \Delta_0}$ [7]. This indicates the low value of α might be due to low R_s or a product of the fit. To increase responsivity we need to increase the kinetic inductance fraction for the next generation of prototype arrays.

Highlighted optical measurement results:

(1) We discovered 3 different fractional frequency response groups in our optical measurements. A low, mid and high response group. We believe the variation in response is due KIDs

detecting radiation from their neighboring FZP lenses. The low response group is thought to be made up of resonators blocked from radiation. The high response group absorbed an average factor of 1.8 more optical power than expected, likely due to stray light being absorbed from neighboring FZP lenses. This limited the accuracy of our NEP calculations and raised doubt that the FZP lenses were suitable for this application.

(2) τ_{qp} was estimated as a function of blackbody power. It varied from 59-171 μs, 53-315 μs, and 38-315 μs in the low, mid and high response groups, respectively. The lifetimes are within expected lifetime for TiN, so the NEP was not limited by shorter than expected lifetimes.

(3) The average two level system noise was measured to be $S_{TLS} = 2.55^{-17}$ Hz $^{-1}$. The PPCs did not reduce TLS noise as we had hoped and was comparable to TLS noise found in IDC KIDs. However, PPCs are still promising because they reduce pixel size enabling a compact instrument.

(4) For estimating R_x we confirmed that Model 2, derived from Mattis-Bardeen theory in Sec. 3.2.2, agrees well with the measured fractional frequency response as a function of absorbed optical power. This model fit the data better than the linear model.

(5) We found that the expected NEPs estimated using the sensitivity model do not match the empirical NEPs of this prototype array. This may be due to stray light in the cryostat, stray light from neighboring FZP lenses, and/or the uncertainty that arises from approximated parameters from the literature. We found better agreement with the sensitivity model and the PRIMA prototype KID array discussed in Ch. 7.

5.4.1 Future Work

A new 25 μm BEGINS TiN KID array has been designed and fabricated with a smaller inductor volume and higher absorption efficiency. This array will be bonded to a Si microlens array. Results of optical tests on a KID array successfully bonded to a microlens array chip are discussed in Ch. 7. The microlens array focuses the light onto the absorber efficiently with no indication of extra radiation from neighboring lenses. The goal with this prototype array is to make changes to increase the responsivity and improve radiation coupling for a more sensitive detector. Dark and optical measurements are planned for this prototype array.

Chapter 6

Mid-IR KIDs for the Galaxy Evolution Probe (GEP)

The Galaxy Evolution Probe (GEP), the predecessor probe to PRIMA, was a concept for a Probe-class space observatory to study the physical processes related to star formation over cosmic time by utilizing large arrays of back-illuminated, lumped-element, microlens-coupled, aluminum kinetic inductance detectors (KIDs). It consisted of one instrument with two modules, an imager (GEP-I) and a dispersive spectrometer (GEP-S). The sensitivity requirements for the modules were an NEP of 1.6x10^{-18} W/$\sqrt{\text{Hz}}$ for the GEP-I and 1x10^{-19} W/$\sqrt{\text{Hz}}$ for the GEP-S. The shortest detection wavelength was 10 μm, vs 25 μm for PRIMA. This short wavelength limit was necessary for detection of polycyclic aromatic hydrocarbons (PAHS) which have rest-frame emission features from 3-13 μm [59], and can be used to measure redshifts and characterize interstellar physical conditions and chemistry in millions of galaxies. Although KIDs research is a popular and growing field, KIDs for the short wavelength range (10-100 μm) are just starting to be developed.

In this chapter we present an inductor geometry for KIDs sensitive to wavelengths of 10 μm, challenges that come with optimizing our design to increase the wavelength range, initial tests on our design of fabricated 10 μm KIDs, and theoretical NEP calculations. The prototype array and results discussed in this chapter were preliminary measurements made before we decided to move forward with PRIMA 25 μm KIDs. Therefore, there are not any optical measurements. This prototype array still has potential for future space missions. The work in this chapter is split up as follows: The KID absorber was proposed by Jonas Zmuidzinas and I did further investigation to improve the design, Peter Day designed the complete KID array, the KID array was fabricated by Rick Leduc, dark measurements were made by Peter Day at JPL and the analysis was done be me.

Our main goal with the research presented in this chapter was to set the groundwork for KIDs sensitive to 10 μm and determine if the GEP NEP requirements are theoretically met at 10 μm. The goal of the dark measurements discussed in this chapter were to determine the KID arrays f_r, T_c, α, Q_i, array yield, and find evidence of TLS noise. This is important for the following reasons:

(1) If these values deviate significantly from the expected design or predicted values there is an issue with the fabrication and/or material that must be investigated and addressed.

(2) The responsitivies and sensitivities of the KIDs have a dependence on T_c and α.

(3) The noise PSD measurements presented were to find evidence of TLS noise and estimate the level of TLS noise (S_{TLS}).

(4) Estimations of T_c, α, and S_{TLS} are necessary parameters to predict if GEP NEP requirements are achievable.

6.1 10 μm Al KIDs Design

The resonator type chosen for the GEP KIDs was an LEKID. Each KID consists of a lithographically patterned absorbing inductive section connected to a large interdigitated capacitor and coupled to the feedline with small interdigitated capacitors. The goal with this prototype array was to create a low volume inductor design sensitive to 10 μm. Since the NEP is proportional to the active volume, we expect the NEP to decrease with volume. The inductors of the LEKIDs consist of 60 μm circular envelopes effective for optical coupling to a microlens array.

The material used for all components of the LEKID is a single layer 40 nm thick Al. Al is well described by the Mattis-Bardeen theory and has been shown to have a long quasiparticle lifetime greater than 1.5 ms [34, 44]. This is an attractive feature because the NEP is inversely proportional to τ_{qp}, so long lifetimes should lead to lower NEPs. We also chose Al because its T_c

is well known. Pure Al has a $T_c = 1.2$ K, which corresponds to a band gap energy of $\Delta_0 = 182$ eV. Therefore, photons with energies greater than 364 eV can break Cooper pairs. This energy corresponds to wavelengths shorter than 3.4 mm, of interest for GEP.

The inductor deign was proposed by Jonas Zmuidzinas and I did further investigations for improvements through simulations. The approach taken to create an inductor design that would enhance absorption at 10 μm was to incorporate resonant structures in the absorber, which makes the absorber a type of frequency selective surface. This approach is inspired by the use of resonant techniques for impedance matching in electrical circuits. We refer to the inductor design explored as a short meander, which has multiple resonant features and is broadband at a wavelength of 10 μm.

6.1.1 Inductor Design

The inductor is comprised of periodic geometric structures with absorption features at 10 μm, repeated in a circular envelope. This is depicted in the top image of Fig. 6.1 where the geometric structure shown in the bottom left of Fig. 6.1 is repeated to form the inductor. In order to predict and model the absoprtion efficiency we used ANSYS High Frequency Structure Simulator (HFSS)[1] simulations. HFSS, is a full-wave frequency domain electromagnetic field solver based on the finite element method that numerically solves Maxwell's equations across a specified frequency range for a specified structure geometry, material configuration, and boundary conditions.

HFSS simulations were done using a single unit cell simulated in an infinite periodic grid to approximate the repeated geometric structure across the absorber, Fig. 6.1 Bottom Right. Floquet ports were assigned to the faces of the vacuum and substrate boxes which allows simulation of a plane wave with two Floquet modes (TE_{00} and TM_{00}) that represent the incident horizontally and vertically polarized electromagnetic plane waves. HFSS achieves the periodic grid condition by assigning linked boundaries between parallel walls of the vacuum and substrate boxes of the unit cell. The linked boundaries enforce the parallel walls to have the same fields. The simulation calculates

[1] `https://www.ansys.com/products/electronics/ansys-hfss`

the S-parameters from which the absorption efficiency can be determined by, $A = 1 - |S_{21}|^2 - S_|11|^2$. Where S_{21} and S_{11} are the S parameters used to calculate the transmittance and reflectance of the incident wave, respectively.

The aluminum (blue meander in Fig. 6.1 Bottom) was modeled with a sheet of impedance set to that of 40 nm thick aluminum exposed to 30 THz electromagnetic radiation on a substrate,

$$Z_s = \frac{1+i}{\delta\sigma} coth\Big(\frac{1+i}{\delta}t\Big), \tag{6.1}$$

where δ = 11.14 nm is the skin depth, σ = 6.87x10^7 Ω^{-1}m^{-1} is the conductivity, and t is the thickness of the aluminum [68]. The conductivity was calculated from 4 K sheet resistance measurements of 40 nm thick sputtered aluminum films made at JPL. At 30 THz (= 10 μm) in cryogenic temperatures the sheet impedance is estimated to be, Z_s = (1.32+1.32i) Ω.

The 2.4 $\times$ 2.4 μm unit cell with the short meander geometry (Fig. 6.1 Bottom Left), has aluminum line widths and gaps of 200 nm. The vertical lines couple to vertically polarized light, and the horizontal portion of the meander increases the resistance per unit length, enabling high absorption efficiency. This geometry was chosen because of its high HFSS-simulated absorption efficiency at 30 THz (Fig. 6.2 Left). When simulated on a silicon (Si) substrate with a dielectric constant of 11.7, the absorption efficiency at 30 THz is near 73%. Since the absorption profile is broad, spectral bands can be defined with band pass filters. Although Si is a common substrate material it contains absorption features at 10 μm. This problem can be addressed by using a germanium substrate (Ge) which has better transmittance than Si from 10-20 μm [18]. The simulation results of the the short meander on a germanium (Ge) substrate are shown in the right plot of Fig. 6.2. Since Ge has a dielectric constant of 16, the resonance features are shifted to lower frequencies [11]. This is seen when comparing the solid lines of the left and right plots in Fig. 6.2, for aluminum linewidths of 200 nm and unit cell size of 2.4 $\times$ 2.4 μm where the absorption profile at 30 THz with the Si shifts to 25 THz with the Ge. To achieve absorption features at 30 THz the aluminum linewidth and spacing needs to be between 150 - 200 nm, which is achievable with e-beam lithography. The right plot in Fig. 6.2 also demonstrates how the absorbed wavelength scales with the unit cell size enabling the use of the same inductor geometry for a wider range of wavelengths.

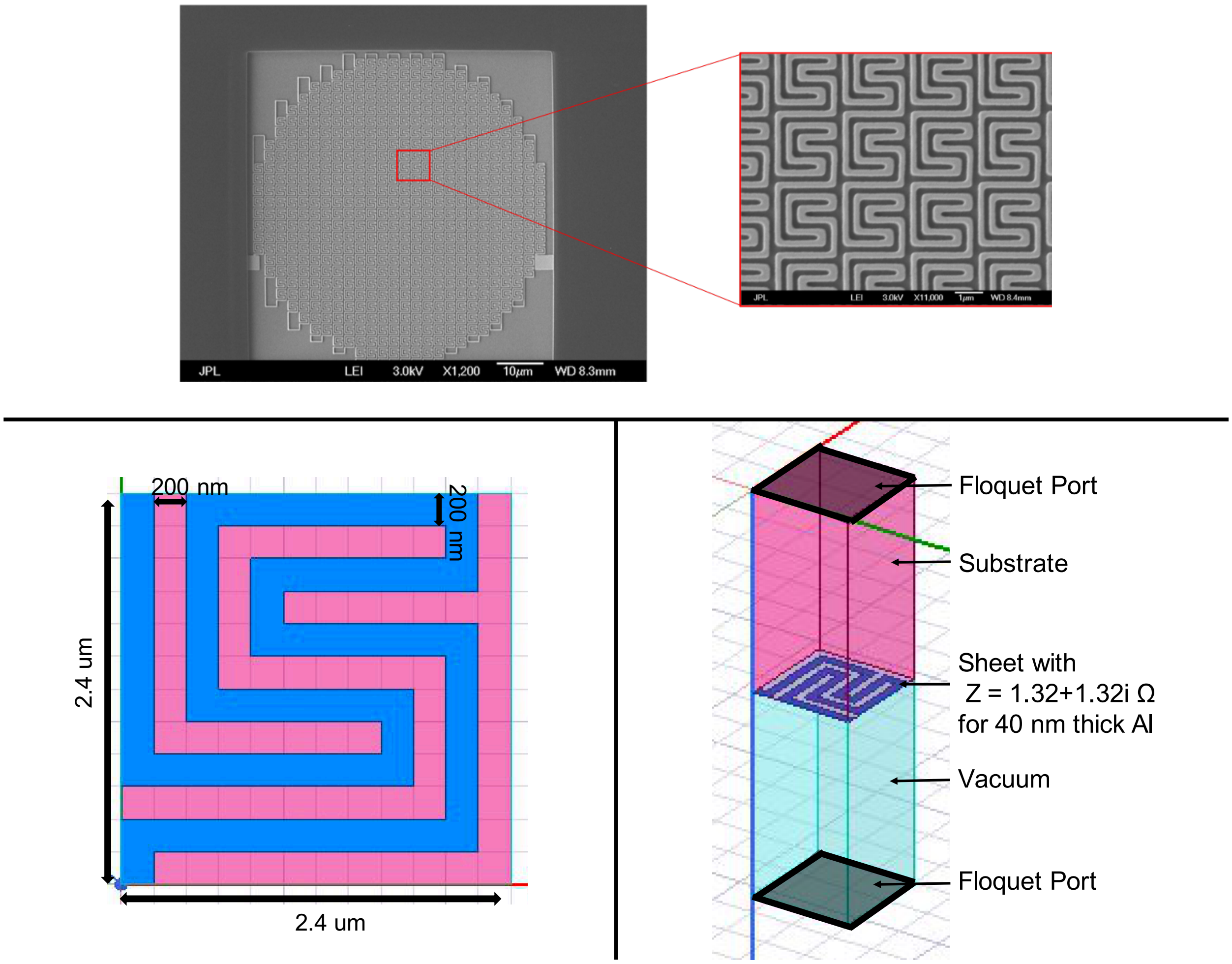

Figure 6.1: (Color figure online) *Top:* Photograph of the inductor portion of a 10 μm KID. The unit cell shown in Fig. 6.1 Bottom Left is repeated to cover the entire absorber area, which has a circular envelope with a diameter of 60 μm. *Bottom Left:* short-meander unit cell geometry. The blue represents Al with Z = $(1.32 + 1.32i)\Omega$ and the pink represents the Si substrate. The material of the microlens array that couples radiation to the KIDs will be made of the same material as the substrate. The total unit cell size depicted is 2.4 x 2.4 μm, but will vary according to wavelength and substrate material. *Bottom Right:* 3D model of HFSS unit cell simulation. The plane wave travels from the top Floquet port to the bottom Floquet Port. The vacuum and substrate box heights have been shortened for illustration purposes to show where the Floquet ports are assigned.

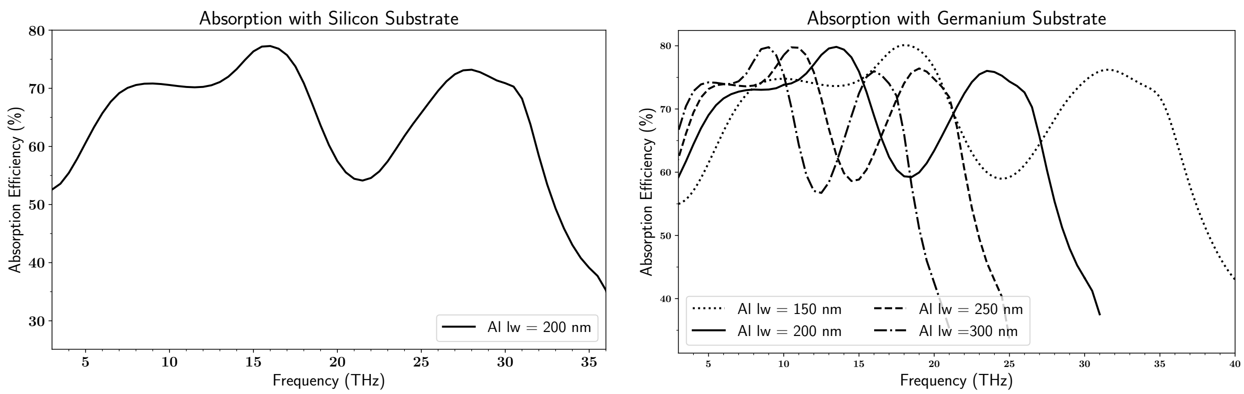

Figure 6.2: HFSS-simulated absorption efficiency of short-meander (lw = aluminum line width). *Left:* Absorption efficiency of about 73% near 30 THz on Si substrate. *Right:* Absorption efficiency shifts to lower frequencies (greater wavelength) as lw is increased on Ge substrate. Absorption efficiency varies from 16-32 THz, showing that the detector is capable of absorbing different wavelengths by adjusting the aluminum line width and unit cell size.

6.2 Preliminary Measurements

A test prototype array with the short meander inductor design and 40 nm thick aluminum was fabricated at the Microdevices Laboratory at JPL, on a Si substrate (Fig. 6.1 Top). The array consisted of a 4x48 array of LEKIDs spaced on a 250 μm pitch. Initial testing showed 70% yield for resonant frequencies from 1.37-2 GHz with high internal Q-factors on the order of 5×10^5. We performed bath temperature sweep measurements of a resonator at 1.37 GHz to estimate the T_c and kinetic inductance fraction (α) of the prototype array. Noise measurements were also made to identify TLS noise. These measurements were used to calculate theoretical NEPs of the prototype array.

6.2.1 Results: T_c Measurements

A bath temperature sweep measurement from 25 to 400 mK was made for one resonator at 1.37 GHz. Measurements were performed by Peter Day at JPL and I performed the analysis. The critical temperature and kinetic inductance fraction were estimated using the model and method described in Sec. 3.1.2, yielding $T_c = (1.32 \pm 0.05)$ K and $\alpha = 0.763$. This result is comparable to the T_c and α of aluminum found in the literature [12, 83, 44]. The estimated values will be used as input parameters for the sensitivity model discussed in Sec. 6.4.

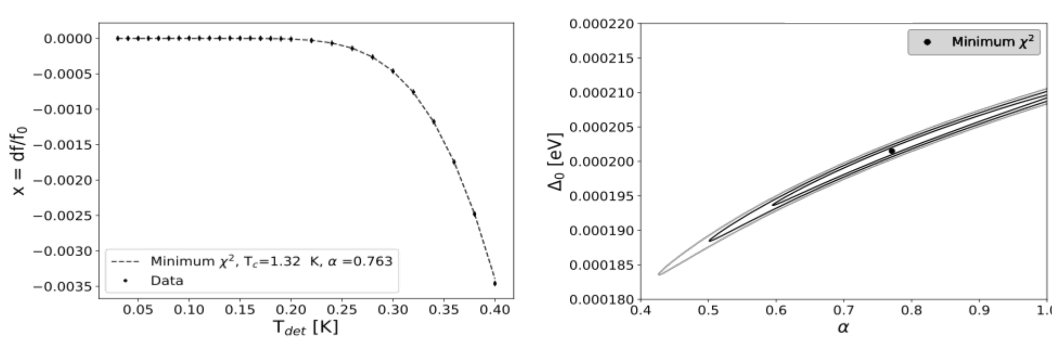

Figure 6.3: *Left:* Fractional frequency shift as a function of temperature. The *dashed line* represents the best-fit model. *Right:* $\Delta\chi^2$ contour plots of 1σ, 2σ, and 3σ uncertainties in the parameters. The 1σ bounds were used to assign an error to T_c, which yielded $T_c = (1.32 \pm 0.05)$ K.

6.3 Results: TLS Noise

Noise measurements of the resonator at 1.37 GHz were taken to determine if TLS noise was present in the KIDs. The noise measurements were taken at bath temperatures of 100 mK and 200 mK with varying drive powers of -102 dBm, -104 dBm, -106 dBm, and -108 dBm at each temperature. As noted in Sec. 3.3.4, TLS noise has a 1/f shape in the frequency noise and has been shown to decrease with increasing drive power and increasing temperature. The S_{xx} PSDs in the frequency noise direction, found to be dominated by fundamental detector noise sources, are shown in Fig. 6.4 (refer to Sec. 5.3.3 for a discussion on PSD features). We observe that S_{xx} decrease with increasing drive power and decreases with increasing temperature, verifying the presence of TLS noise. For a bath temperature of 100 mK the noise starts at $\sim 5 \times 10^{-16}$ Hz^{-1} and decreases to $\sim 1 \times 10^{-16}$ Hz^{-1} for a bath temperature of 200 mK, showing a significant difference. The noise measurements also allow us to infer S_{TLS}, which is an input parameter for theoretical NEPs calculations of the GEP KID arrays. A fit to the noise PSD at 100 mK (GEP KIDs operating temperature) for a drive power of -102 dBm yielded $S_{TLS} = 2.84{\times}10^{-16}$ Hz^{-1} (PSD fits are discussed in Sec. 5.3.4). This drive power was chosen to calculate the theoretical NEP, because the resonators will be driven at the highest power possible below bifurcation to reduce TLS noise and improve the NEPs of the KIDs. The TLS noise level is comparable to values seen in the literature, however, lower levels of TLS noise for IDC KIDs have also been measured [34, 44]. To improve the TLS noise we can increase the capacitor size or switch to PPCs.

Another feature shown in the noise PSDs is the resonator ring time, $\tau_{ring} = \frac{Q_r}{\pi f_r}$, an intrinsic feature of LC circuits that reflects how long a resonator takes to dissipate energy. This resonator was calculated to have a $\tau_{ring} = 6.7\mu s$ (=1.5×10^5 Hz), which is identifiable at both bath temperatures (Fig. 6.4 black dashed-dotted line). If the quasiparticle lifetime is longer than the resonator ring time we are not able to determine τ_{qp} from the PSDs. A slight roll-off before τ_{ring} is observed at $\sim$ 10 kHz, but due to the dominating 1/f noise we were not able to produce confident fits for τ_{qp} of the prototype array. Since we did not do optical measurements or continue investigating this prototype array we were not able to determine if τ_{qp} would limit its empirical NEP.

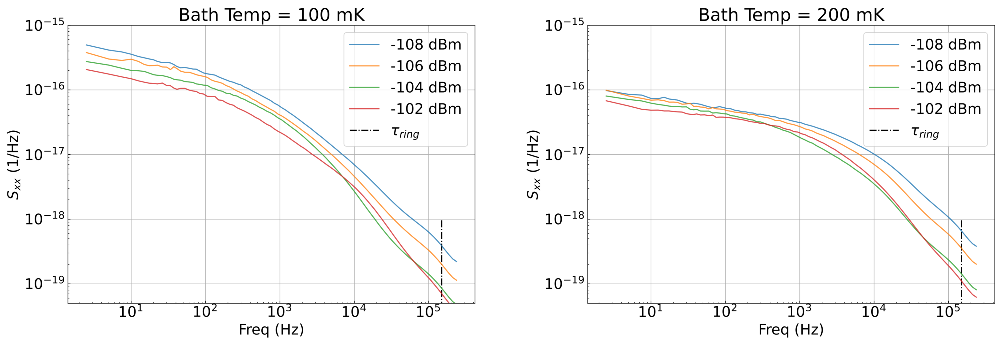

Figure 6.4: S_{xx} PSDs in the frequency noise direction, showing evidence of TLS noise. As the driving power decreases the noise increases (driving power starts at -102 dBm and is attenuated by 2 dB with each curve). At higher temperature (200 mK) the noise decreases. A fit to the noise PSD at 100 mK for a drive power of -102 dBm gives $S_{TLS} = 2.84 \times 10^{-16} Hz^{-1}$. The black dashed line indicated the resonator ring time roll off at $\tau_{ring} = 6.7 \mu s$ (=1.5 $\times$ $10^5 Hz$).

6.4 Theoretical NEPs

Although we did not perform optical measurements on this prototype array a theoretical NEP was calculated using the formulas and iteration method found in Sec. 3.3. The total NEP was calculated by adding all NEP contributions in quadrature, $\mathrm{NEP_{tot}}^2 = \mathrm{NEP_{TLS}}^2 + \mathrm{NEP_{amp}}^2 + \mathrm{NEP_{photon}}^2 + \mathrm{NEP_{GR}}^2$. Table 6.1, shows all the parameters needed to calculate the NEPs, their values and how their values were determined. Values that were taken from the literature have their reference included in the "Source" column. The operating temperature for GEP was T = 100 mK with an expected photon loading of 6.3×10^{-17} W at λ =10 μm. Fig. 6.5, shows the results of the theoretical NEPs as a function of absorbed optical power. At an absorbed optical power of 6.3×10^{-17} W, the estimated total NEP is 1.65×10^{-18} W/$\sqrt{\text{Hz}}$ and the estimated photon noise NEP (blue line) is 1.6×10^{-18} W/$\sqrt{\text{Hz}}$. Although the total NEP is comparable to GEP-I sensitivities it, is limited by $\mathrm{NEP_{TLS}}$ (purple line in Fig. 6.5) and improvements on the GEP prototype array are required to be photon-noise limited. Replacing the IDCs with PPCs may solve this issue. We have shown lower levels of TLS noise with PPCs (S_{TLS} on the order of 10^{-17} Hz^{-1}) for BEGINS and PRIMA KIDs (Ch. 5 and Ch. 7). If we apply the TLS noise found in the aluminum PRIMA KIDs

(Sec 7.4.4) of $S_{TLS} = 9.2\times^{-17}$ Hz^{-17} we theoretically meet NEP requirements and the detector noise is sub-dominant to the photon-noise (Fig. 6.6). The theoretical predictions are promising but to confirm them optical measurements are required on a new prototype array with PPCs.

Table 6.1: Theoretical NEP Input Parameters for 10 μm GEP KIDs.

Symbol	Parameter	Value	Source
f_r	resonant freq	1372.39 MHz	measured
ν	optical freq	30 THz	known
T_c	Critical Temperature	1.32 K	estimated
$Q_{i,0}$	Internal quality factor	512251	estimated
Q_c	Coupling quality factor	30492	estimated
χ_g	generator efficiency	1	[108]
η_{pb}	Pair-breaking efficiency	0.57	[44]
τ_0	characteristic electron-phonon interaction time	438 ns	[51]
τ_{max}	experimentally observed max lifetime	1000 μs	[108]
V	Inductor volume	56.55 μm^3	calculated
η_a	qp breaking Readout efficiency	.001	[108, 44]
α	Kinetic inductance fraction	0.763	estimated
T_{oper}	bath temp	100 mK	known
S_{TLS}	TLS noise	2.84×10^{-16} Hz^{-1}	estimated
P_g	Drive power	6.3×10^{-14} W	known

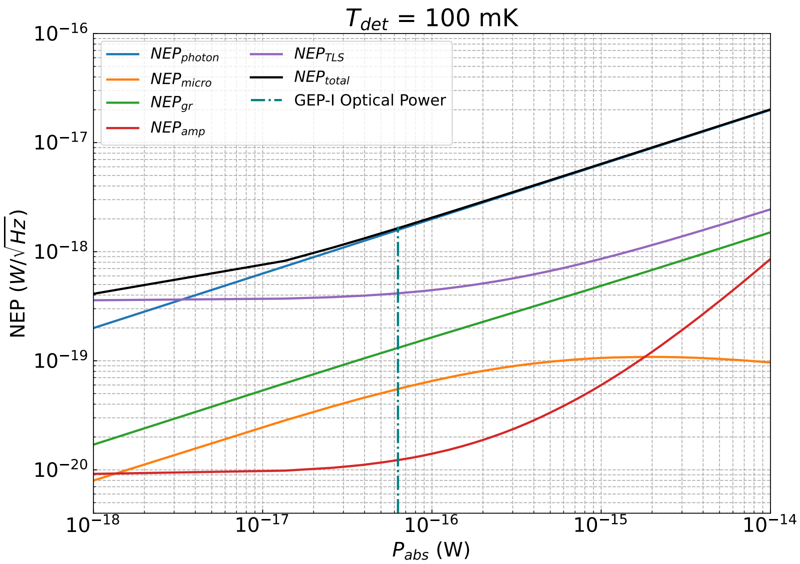

Figure 6.5: Theoretical NEP plot of 10 μm GEP KIDs. The NEPs were calculated using the input parameters listed in Table 6.1 and the estimated T_c, α, and S_{TLS} from the preliminary measurements made on the resonator with f_r = 1.37 Hz from the prototype array. The teal dashed-dotted line represents the estimated GEP optical load at 10 μm of 6.3×10^{-17} W.

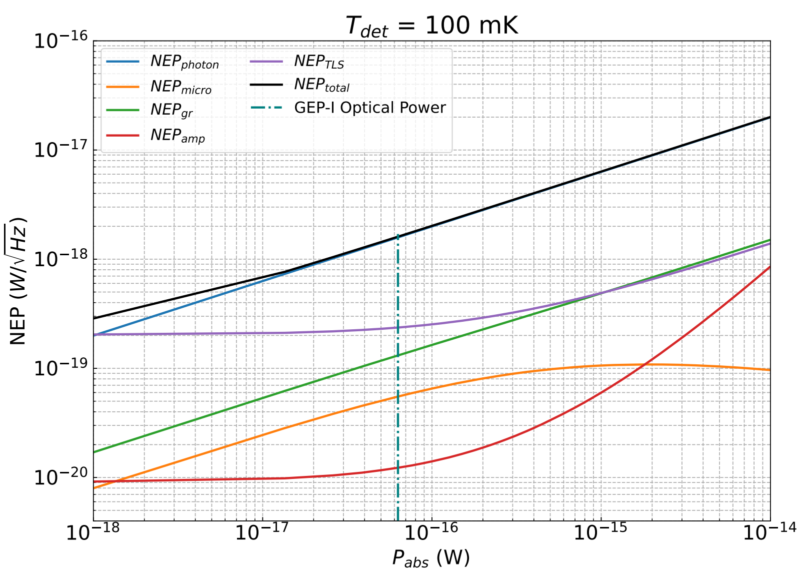

Figure 6.6: Theoretical NEP plot of 10 μm GEP KIDs with $S_{TLS} = 9.2\times^{-17}$ Hz^{-17}, showing the detector is photon-noise limited at the GEP-I optical loading at $\lambda = 10$ μm. The teal dashed-dotted line represents the estimated GEP optical load at 10 μm of 6.3×10^{-17} W.

6.5 Discussion

In this chapter I have discussed the simulated absorption efficiency of a KID design sensitive to 10 μm and the results of dark measurements on a fabricated array with our design of the 10 μm KIDs. This was preliminary work towards KID arrays for PRIMA's predecessor GEP, which shortest detection wavelength was 10 μm. We met the goal of developing a KID design sensitive to 10 μm that theoretically meets GEP-I requirements of $\sim 1.6 \times 10^{-17}$ W/$\sqrt{\mathrm{Hz}}$ with PPCs for an optical load of 6.3×10^{-17} W at 10 μm. Below I will highlight results from the simulations and the dark measurements.

Highlighted absorption efficiency simulation results:

(1) We successfully developed a broadband KID absorber (or inductor) sensitive to wavelengths of 10 μm with a high absorption efficiency of ~73 % on a Si substrate with no back-short. The absorber is a frequency selective surface with a short meander periodically repeated across the the inductor area and sensitive to vertically polarized light.

(2) Although Si is a common substrate material it contains absorption features at 10 μm, so simulations were also performed with a germanium substrate which has better transmittance than Si from 10-20 μm. Simulations with Ge yielded an absorption efficiency $\sim$ 75%, an increase of 2 %.

(3) We verified that the absorbed wavelength scales with the short meander unit cell size, enabling the use of the same inductor geometry for a wider range of wavelengths.

(4) Optical measurements of the absorber were not made to verify the simulated efficiency. However, it is still a promising geometry for mid-IR KIDs.

Highlighted dark measurement results:

(1) Fractional resonant frequency shift vs bath temperature measurements yielded T_c = (1.32 $\pm$ 0.05) K and $\alpha = 0.763$. This result is comparable to the T_c and α of aluminum found in the literature [12, 83, 44].

(2) The TLS noise level was estimated to be $S_{TLS} = 2.84\times10^{-16}$ Hz^{-1} at 100 mK (the detectors operating temperature for GEP). The TLS noise level is comparable to values seen in the literature, however, lower levels of TLS noise for IDC KIDs have also been measured [34, 44].

(3) The estimate parameters from dark measurements listed above were used to predict the NEP of the fabricated prototype array. It was shown to be photon-noise limited down to $\sim 2\times10^{-18}$ W/$\sqrt{\text{Hz}}$ with IDCs. Which did not meet the GEP NEP requirements. However, if PPCs are used the prototype array has the potential to be photon-noise limited down to $\sim 1.5 \times 10^{-18}$ W/$\sqrt{\text{Hz}}$ and meets requirements for GEP-I.

After this work we shifted our focus to 25 μm PRIMA KIDs and did not perform optical measurements to estimate the sensitivity of the KID array. However, this work is promising for future observatories that plan to utilize KIDs in this wavelength range.

Chapter 7

Aluminum KIDs for PRIMA

In this chapter I will discuss the design and characterization of the first generation 25 μm PRIMA KID array, the shortest wavelength covered by PRIMA. I will discuss the results of dark and optical measurements made to reach the PRIMA KID sensitivity requirements for detection at 25 μm and future work towards PRIMA KID arrays. The research discussed in this chapter was split up as follows: Peter Day designed the prototype array, the prototype array was fabricated at JPL by Rick Leduc, optical measurements were done at JPL and the analysis was done by me, measurements and analysis for T_c and α were done by Logan Foote at Caltech.

The goals and purpose of the dark measurements discussed in this chapter are to determine the KID arrays f_r, T_c, α, Q_i, Q_c, and array yield. The importance of these measurements are the same as those listed in Ch. 5. The goals and purpose of the optical measurements are to calculate the KID array noise PSDs (S_{xx}) and empirical NEPs. The PSDs are important for measuring the TLS noise level (S_{TLS}) of the detectors in the array which if too high limits the sensitivity. The empirical NEP will be compared to the expected total NEP derived from the sensitivity model discussed in Sec. 3.3. The ultimate goal of the work presented in this chapter is to determine if the prototype array meets the PRIMA NEP requirements which are on the order of 2.5×10^{-19} W/$\sqrt{\text{Hz}}$ for an optical load of a few attoWatts [1] . This work is also important because it presents the performance of a Si microlens array developed at GSFC that was bonded to the KID array for optical measurements.

[1] These are estimates. The sensitivity had not been finalized at the time that this thesis was written.

7.1 25 μm Al PRIMA KIDs Design

The resonator type chosen for the PRIMA KIDs was an LEKID similar to the ones chosen for the BEGINS KIDs and GEP KIDs, where a discrete inductor is used to absorb radiation. The inductors consists of 70 μm circular envelopes for coupling to a microlens array and the capacitors are parallel plate capacitors (PPC). The prototype PRIMA KID consisted of a single layer of 30 nm thick aluminum lithographically patterned on a 675 μm thick Si substrate. The array employs PPC capacitors to decrease TLS noise and aluminum superconducting material which has shown to have long quasiparticle lifetimes to reach the required PRIMA NEPs that are on the order of 2.5×10^{-19} W/$\sqrt{\text{Hz}}$. The advantage of PPCs and aluminum are discussed in Chapters 5 and 6, respectively.

Fig. 7.1, shows images of the fabricated PRIMA prototype array. The test array has 44 KIDs with a pitch of 900 μm. The frequency bandwidth of the array is set by the length of the PPC while the inductor size and geometry is identical for each KID. To increase the responsivity of the detectors the inductors were designed to have a high absorption efficiency at 25 μm and are a low volume of 17 μm^3. Test samples with only the resonant structure on a Si substrate were made to determine the absorption profile of the fabricated inductors, which is important for estimating the optical power absorbed by the detector.

7.1.1 Inductor Design and Characterization

The inductor geometry for PRIMA KIDs was designed by Peter Day and is capable of absorbing both polarizations on a single detector. Similar to the GEP KID inductor, it is a type of frequency selective surface with a periodic structure across the circular envelope. Fig. 7.2 Left shows the unit cell of the structure that is repeated across the inductor (Fig. 7.2 Right). The periodic structure sets the width and center frequency of the absorption resonance. It was designed to have an absorption profile that peaks at 25 μm (=400 cm^{-1}) in both polarization directions.

To measure the absorption of the inductor a 1-inch sample with the aluminum inductor

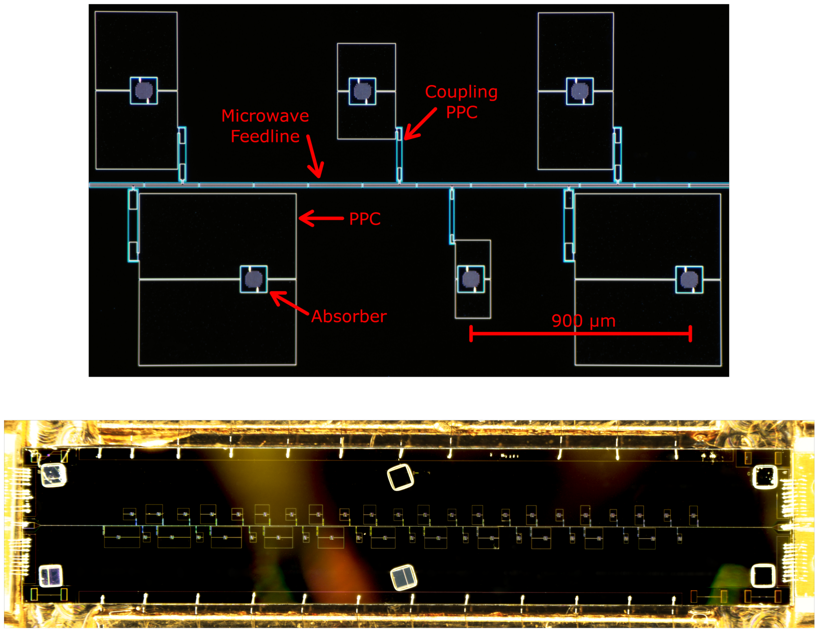

Figure 7.1: Images of fabricated 25 μm PRIMA KID prototype array. The inductors consists of 70 μm circular envelopes for coupling to a microlens array and the capacitors are PPCs. The test array has 44 KIDs with a pitch of 900 μm.

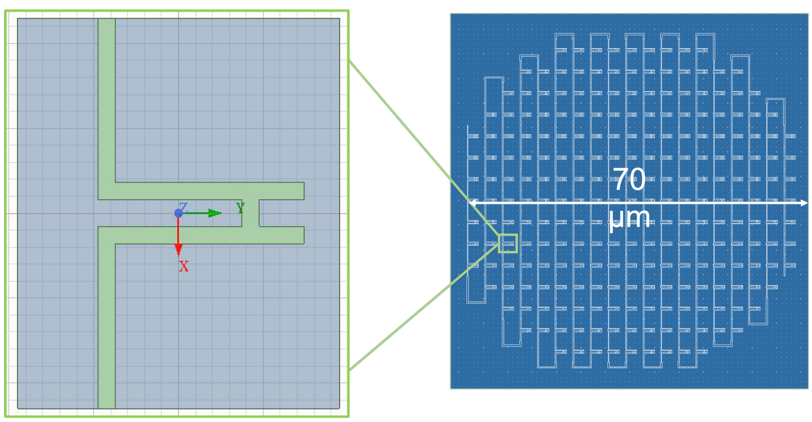

Figure 7.2: *Left*: The unit cell of the resonant structure that is repeated across the inductor and sensitive to both polarizations. The geometry of the structure sets the width and the center frequency of the absorption resonance. *Right*: Layout of the inductors portion of the 25 μm PRIMA KIDs. inductors consists of 70 μm circular envelopes for coupling to a microlens array.

trace on a Si substrate was fabricated. The transmission of the sample was measured at 5 K by the GSFC optics group using a Fourier transform spectrometer (FTS). Fig. 7.3 *Top*, shows the measured transmittance of both horizontal (H) and vertical (V) polarizations of the fabricated inductor sample. The FTS resolution was set to 0.06 icm to resolve the fringes that arise from the Si cavity that is between the vacuum and Al absorber interfaces. The values of the fringe peaks and troughs allow us to calculate the absorption of the Al absorber from the measured transmission[2] which can then be used to calculate the absorbed blackbody power in Sec. 7.4.2.

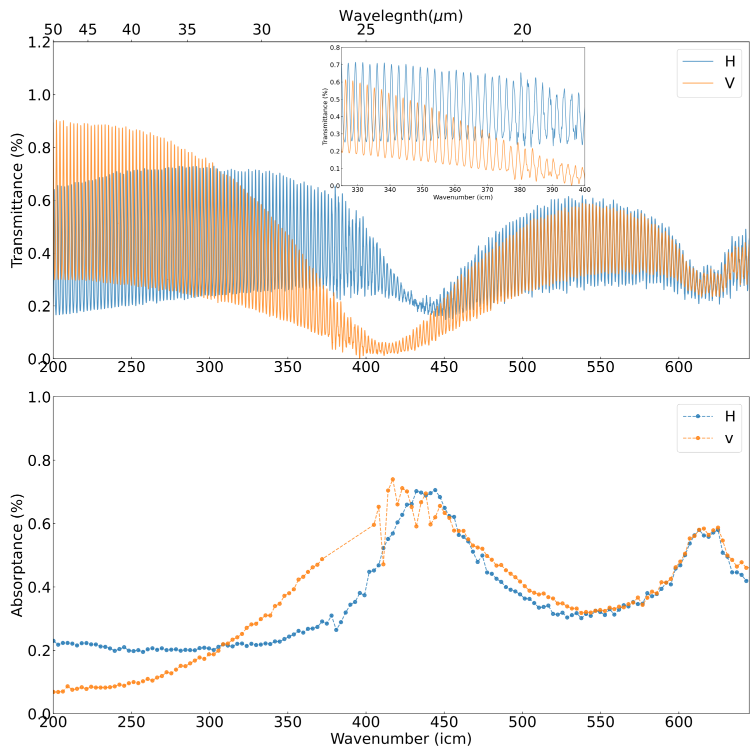

Figure 7.3: *Top*: The horizontal (H) and vertical (V) polarization transmission of a a 1-inch sample with the aluminum inductor trace on a Si substrate measured at 5 K by the GSFC optics group using an FTS. *Bottom*: Absorption spectra extracted from the FTS transmission measurements.

2 Derived with the help of Peter Day through private communication.

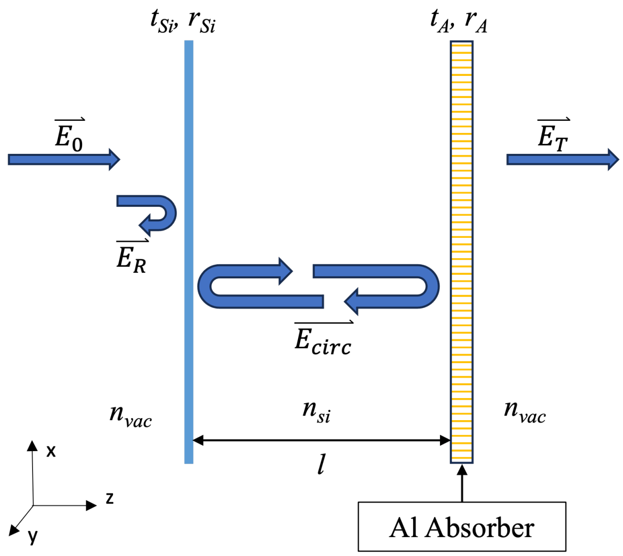

Figure 7.4: A simplified Etalon/Fabry-Perot interferometer diagram of the Si-cavity between vacuum and the 25 μm PRIMA Al absorber. A complete general diagram can be found in reference [48], by Ismail et al.

A simplified etalon diagram of the Si cavity between vacuum and the Al absorber is shown in Fig. 7.4. The electric field amplitude of the output transmitted plane wave, E_t, through an etalon is given by [96],

$$E_t = E_0 \frac{t_{Si} t_A e^{i\beta l}}{1 - r_{Si} r_A e^{2i\beta l}} \tag{7.1}$$

and the power transmission is

$$T = \frac{|E_t|^2}{|E_0|^2}, \tag{7.2}$$

where E_0 is the electric field amplitude of the incident plane wave, t_{Si} and r_{Si} are the transmission and reflection coefficients at the vacuum-Si interface, t_A and r_A are the transmission and reflection coefficients at the Si-Al absorber interface and $\beta = \frac{2\pi}{\lambda}$ is the wave-number. Of these we measure the power transmission (T) and can derive t_{Si} and r_{Si}. Since we are interested in the reflection within the Si cavity that creates the fringes, we define r_{Si} as the reflection coefficient in Si reflecting off the vacuum surface. Therefore r_{Si} is,

$$r_{Si} = \frac{n_{Si} - n_{vac}}{n_{Si} + n_{vac}}, \tag{7.3}$$

$$\tag{7.4}$$

and the transmission coefficient, t_{Si} from vacuum to Si is given by

$$t_{Si} = \frac{2}{1 + n_{Si}}, \tag{7.5}$$

where n_{Si} and n_{vac} are index of refraction of Si and vacuum, respectively. The transmission reaches a maximum value when the term $e^{2i\beta l} = +1$, and a minimum value when $e^{2i\beta l} = -1$.

We start by defining T_{max} and T_{min} as the transmissions at the peak (maximum) and trough (minimum) of a fringe, respectively,

$$T_{max} = \frac{|E_t|^2}{|E_0|^2} = \left| \frac{t_{Si} t_A}{1 - r_{Si} r_A} \right|^2, \tag{7.6}$$

$$T_{min} = \frac{|E_t|^2}{|E_0|^2} = \left| \frac{t_{Si} t_A}{1 + r_{Si} r_A} \right|^2. \tag{7.7}$$

We can solve for r_A by taking the ratio of T_{max}/T_{min},

$$\frac{T_{max}}{T_{min}} = \left| \frac{1 + r_{Si} r_A}{1 - r_{Si} r_A} \right|^2 \Rightarrow \sqrt{\frac{T_{max}}{T_{min}}} = \frac{1 + r_{Si} r_A}{1 - r_{Si} r_A} \tag{7.8}$$

$$r_A = \frac{\sqrt{\frac{T_{max}}{T_{min}}} - 1}{r_{Si}(\sqrt{\frac{T_{max}}{T_{min}}} + 1)}. \tag{7.9}$$

Next, we can use Eq. 7.6 to solve for t_A which gives,

$$t_A = \frac{\sqrt{T_{max}}}{t_{Si}}(1 - r_{Si} r_A). \tag{7.10}$$

Substituting Eq. 7.9 in for r_A and simplifying gives the following expression for t_A,

$$t_A = \frac{2}{t_{Si}} \left(\frac{1}{\sqrt{T_{max}}} + \frac{1}{\sqrt{T_{min}}} \right)^{-1}. \tag{7.11}$$

The measured values of T_{max} and T_{min}, shown in Fig. 7.3 Top, are then used to solve for r_A and t_A for each polarization separately. Lastly, we derive an equation to calculate the absorption of the aluminum absorber. The plane wave is traveling through two different media, Si and vacuum. The power per unit area of a plane wave traveling through a medium in the positive z direction is given by the Poynting vector, P=$\frac{n|E_x|^2}{Z_0}$, where Z_0 is the impedance of free space and n is the index of the refraction of the medium. Part of the power of the plane wave is reflected back into the Si, part of it is absorbed by the absorber and the remainder is transmitted. The power per unit area of the incident plane wave can then be described by the following expression,

$$\frac{n_{Si}|E_x|^2}{Z_0} = \frac{n_{Si}r_A^2|E_x|^2}{Z_0} + \frac{n_{vac}t_A^2|E_x|^2}{Z_0} + P_{absorbed}, \tag{7.12}$$

where $P_{absorbed}$ is the power absorbed. We can calculate the the absorptance (A_{abs}), which is the fraction of power absorbed relative to the incident plane wave, by dividing both sides of the equation above by the power of the incident plane wave ($\frac{n_{Si}|E_x|^2}{Z_0}$), yielding

$$A_{abs} = 1 - r_A^2 - \frac{n_{vac}t_A^2}{n_{Si}}. \tag{7.13}$$

Now r_A and t_A for each polarization can be inserted into Eq. 7.13 to obtain the absorptance spectra for each polarization, shown in Fig. 7.3 Bottom. The peak shown above 600 cm^{-1} is a Si absorption feature. The peaks near 450 cm^{-1} are the absorption of the 25 μm absorber with a maximum absorption of 70-75%. We expected the peak to be at 400 cm^{-1}. The difference is likely due to differences in the fabricated vs. designed periodic structure, such as the Al linewidth and the length and width of the horizontal portion of the structure. These will be adjusted in the next batch of fabricated prototype arrays. We use these absorptance spectra to calculate the amount of blackbody power that is absorbed by the inductors in the optical measurements.

7.2 Optical Coupling Scheme

The PRIMA KIDs test array and flight array will be optically coupled to monolithic arrays of silicon microlenses with a parabolic profile and back-illuminated. Microlenses couple the incoming radiation from the telescope onto the absorbers, effectively increasing the filling factor of the absorbers on the focal plane. It is also critical to ensure that radiation is coupled onto the absorber and not into other components or reflected within the Si substrate to be absorbed by other KIDs. The challenges we faced with microlens arrays were the lack of such lenses available for wavelengths at 25 μm and determining the best method to attach the microlens array to the KID array without damaging the KIDs. At 25 μm wavelegnths technical challenges arise due tight tolerances on surface accuracy and roughness. These challenges were addressed and solved by our collaborators at the DDL in GSFC, who developed a method to design and fabricate full-depth monolithic silicon arrays for wavelengths down to 25 μm.

Fig. 7.5, shows a model of the optical-coupling scheme we employed for the microlens array. The first gray layer consists of an anti-reflection (AR) coated Si microlens array on a Si substrate, the second thin orange layer is the bonding epoxy layer which attaches the lens array substrate to the back of the KID array substrate (the second gray layer). The cyan rectangles represent the KID absorbers and the dark gray line below represents either a quarter-wave back short or an absorbing back-short.

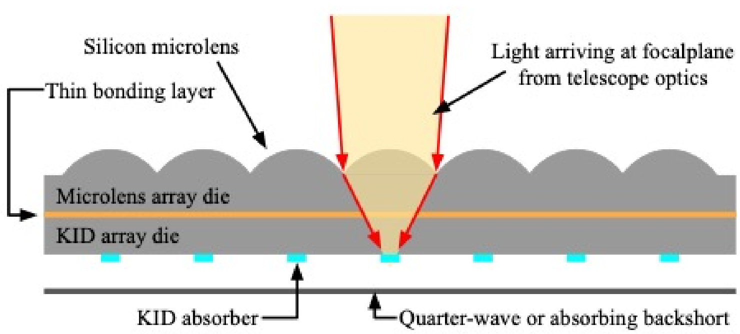

Figure 7.5: A model of the optical-coupling scheme employed for the PRIMA microlens array.

The microlenses are designed, fabricated, and packaged at the Detector Device Laboratory

(DDL) at GSFC. They are fabricated on 525 μm thick double-side polished, high resistivity float-zone wafers. The DDL developed a method to fabricate the lenses using gray-scale lithography combined with deep reactive ion etching. The lithography was done with a Heidleberg DWL 66+laser-pattern generator. After fabricating the microlenses they are AR-coated with Parylene-C and cleaned with a solvent wash to prepare for bonding to a KID array. A discussion on anti-reflection coatings and Parylene-C are presented in Sec. 8.5.1. The microlens array and KID array both are aligned and bonded with a Smart Equipment Technology FC150 flip-chip bonder. They are aligned to within 3 μm using alignment marks etched onto bonding surfaces of each array substrate. A tapered syringe is then used to apply the epoxy onto the back-side of the KID array. The substrates are then brought into contact and compressed to minimize the thickness of the epoxy while it cures. Fig. 7.6, shows a photograph of a 44-element anti-reflection coated microlens array hybridized to the 25 μm PRIMA prototype array, shown in Fig. 7.1 *Bottom*. The lenses have a circular perimeter and are hexagonally packed with a 900 μm pitch to align with the KID absorbers. Finally, the hybridized chip is packaged into a detector package similar to the one shown in 5.3 (Fig. 5.12) for optical measurements.

Profilometry measurements showed that the microlenses match the designed profile well to better than 2 μm. However, the full-depth of the microlens is not captured and will be improved in future trials. The surface root mean square (RMS) surface accuracy was measured to be 53 nm, which is more than sufficient enough for the 25 μm KID arrays. The surface RMS is used to measure the roughness of the surface. A detailed discussion on the microlens arrays is being prepared for submission to, *Applied Optics*.

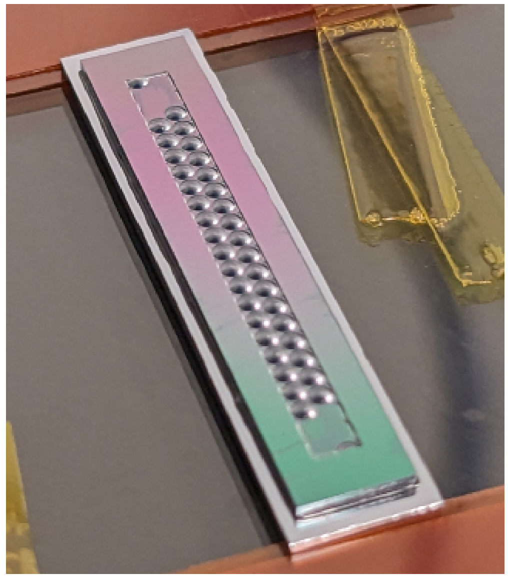

Figure 7.6: A photograph of a 44-element anti-reflection coated microlens array hybridized to the 25 μm PRIMA protoype array, shown in Fig. 7.1. The chip is 1x0.24 inches. *Bottom.* The lenses have a circular perimeter and are hexagonally packed with a 900 μm pitch to align with the KID absorbers.

7.3 Dark Measurement Results

In this section I will discuss the resonant frequencies, quality factors, T_c and α of the 25 μm PRIMA Al KID prototype array. Resonance and quality factors are from measurements made in Peter Day's lab at JPL and analyzed by me. The critical temperatures, T_c, and kinetic induction fractions, α, are from measurements and analysis by Logan Foote at The California Institute of Technology (Caltech).

Fig. 7.7, shows the full S_{21} sweep of the prototype array where each resonance was recorded individually. 43 out of the 44 were found, resulting in a high yield of 98%. The designed frequency span was 250 MHz to 1500 MHz. The measured resonator frequencies ranged from 248 MHz to 1423 MHz, spanning a bandwidth of 1.2 GHz. The large bandwidth was chosen to ensure that there were no colliding resonators, allowing for better optical response measurements. Fig. 7.8 shows histograms of the estimated total, internal, and coupling quality factors (Q_r, Q_i, and Q_c).

The resonators were all designed to have a coupling quality factor, $Q_c = 1 \times 10^4$. Overall, Q_c varies from 1.6×10^4 to 14.3×10^4 with an average of $5.2 \times 10^4 \pm 2.3 \times 10^4$. The array had high Q_i's of $1.7 \times 10^5 \pm 9.0 \times 10^4$.

Dark measurements of an identical prototype array from the same Si wafer were performed at Caltech by Logan Foote. The fractional frequency response of four resonators was measured during a bath temperature sweep from 20 mK to 300 mK and fit to the model discussed in Sec. 3.1.2. For the fit α was fixed to be the design value of 0.8[3] , leaving Tc as the only free parameter in the fit. The estimated T_c for each resonator was 1.39, 1.36, 1.38, and 1.34 K, yielding $T_c = 1.37 \pm 0.02K$[4] .

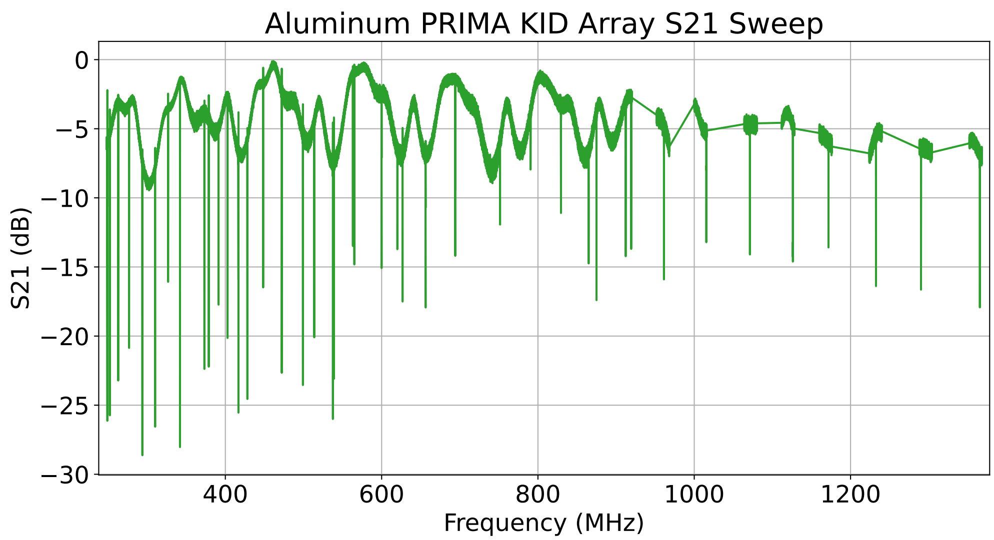

Figure 7.7: 25 μm PRIMA KIDs prototype array VNA S_{21} Sweep. The measured frequency span ranged from 248 MHz to 1423 MHz. 43 out of the 44 KIDS in the array were found, giving a high yield of 98%.

7.4 PRIMA KIDs Optical Performance

Optical tests on the prototype array were performed in Peter Day's cryogenic test bed at JPL and analyzed by me. The tests were performed using a cryogenic blackbody at temperatures of 3, 40, 50, 60, 80, and 100 K, while the prototype array was kept at a bath temperature of 150 mK.

[3] This value was estimated through Sonnet simulations.
[4] Values provided by Logan Foote through private discussion.

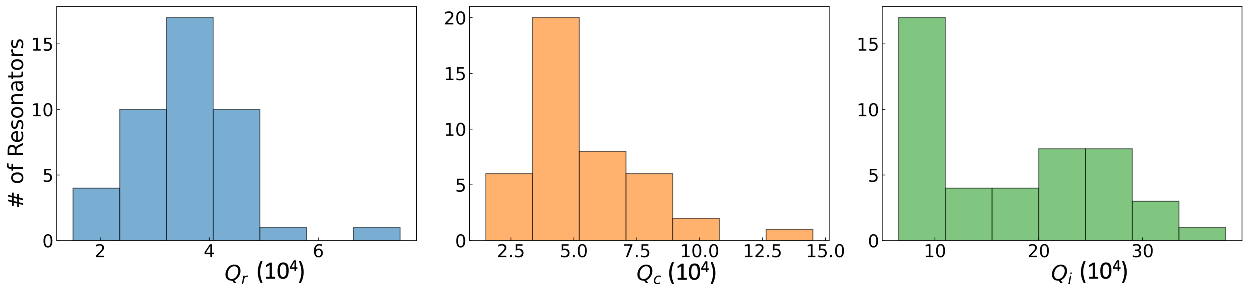

Figure 7.8: Histograms of the estimated quality factors Q_r, Q_i, and Q_c.

The Cardiff filter stacks described in Sec. 5.3, were used to block wavelengths shorter than 25 μm. However, rather than using all four low-pass filters only two were used, the 600 icm low-pass filter and the 1050 icm low-pass filter. A neutral density (ND) filter, was also used to further reduce the blackbody power incident on the detectors to better simulate the attoWatt-range optical loading from the space-based PRIMA instrument. Fig. 7.9 shows the ND filter transmittance at 5 K which will be included in the calculation of the amount of blackbody power absorbed by the detectors. The PRIMA prototype array was packaged like the BEGINS prototype array shown in Figs. 5.11 and 5.12.

Two different types of measurements were made: 1. S_{21} sweeps were recorded at each blackbody temperature using a VNA to measure the fractional frequency response of all the detectors, 2. Single tone measurements of 3 different resonators at blackbody temperatures of 3, 60, 80 and 100 K. These measurements are used to calculate responsivity and electrical NEPs of the prototype array.

7.4.1 PRIMA KIDs Optical Performance

While taking optical measurements of the prototype array we discovered that the resonant frequencies drifted to higher frequencies over time. This drift appears to be due to a component in the cryogenic testbed cooling down over a long period of time, which is adding an optical load on the detectors. The drift in fractional frequency (df/f) vs time is shown in Fig. 7.10. The plot

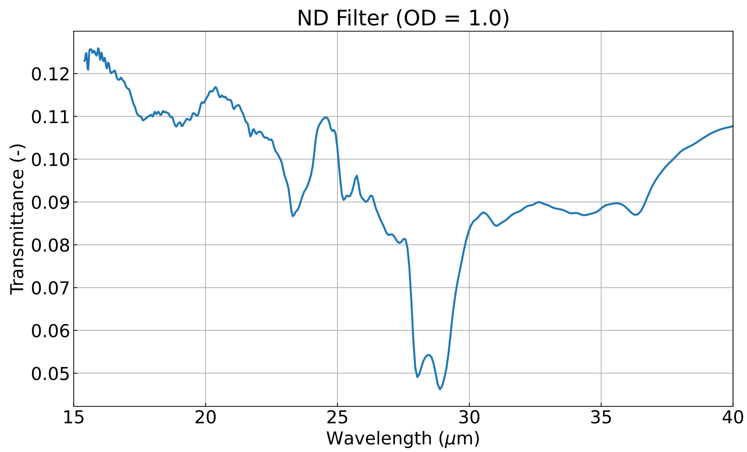

Figure 7.9: Transmittance of a neutral density filter with OD = 1.0 at 5K. This filter is used in the optical measurements experimental set up. The measurement was made with an FTS by the GSFC Optics Group.

shows the fractional frequency response of all the detectors as the blackbody is ramped up from 6-100 K and then ramped down from 100-6K. The colored dots represent the temperature of the blackbody at the time of the measurement. The detectors coupled to a microlens have a response greater than -1.5×10^{-5} at 100 K. The detectors with a response below -0.5×10^{-5} at 100 K are the 8 resonators that are not coupled to a microlens. For a given blackbody temperature, there are differences in fractional frequency response between the ramp-up and ramp-down temperature sweeps, which indicated a temperature drift in part of the instrument that did not reach thermal equilibrium.

In order to remove the drift an exponential decay model is fit to the response of each resonator and removed. The model has the following form,

$$\frac{df}{f}(t) = -Ae^{-Bt} + C. \tag{7.14}$$

The model is only fit to the data where $T_{BB} = 6$, 40, and 50 K, because the response is not significantly affected by the blackbody at these temperatures. An example of the drift removal process is shown for one of the resonators in Fig. 7.11. The left plot shows the response of a

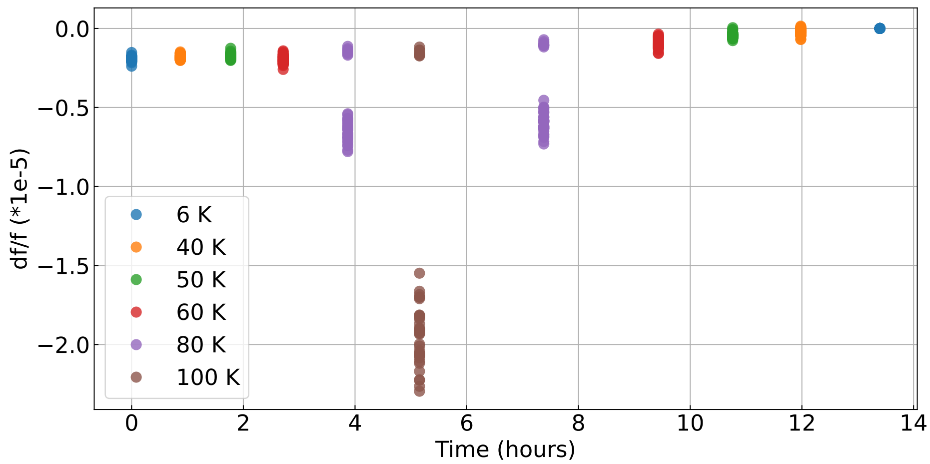

Figure 7.10: Plot of the fractional frequency drift shown across all resonators on the array as a function of time. The fractional frequency response with time is calculated using, $\frac{f_r(t)-f_r(t_f)}{f_r(t_f)}$, where t_f is the time at which the last measurements were taken. The plot shows the fractional frequency response of all the detectors as the blackbody is ramped up from 6-100 K and then ramped down from 100-6K. The colored dots represent the temperature of the blackbody at the time of the measurement.

resonator (blue dots), along with the exponential fit model (green dotted line). This middle plot shows the response with the exponential fit subtracted (red dots). The plot on the right, shows the response with the drift removed plotted as a function of blackbody temperature for the blackbody temperature ramp up (blue dots), ramp down (orange squares) and the average response of the ramp up and ramp down (black stars, demonstrating that this method is effective in removing the drift.

Fig. 7.12, shows histogram of the average fractional frequency response at each blackbody temperature relative to the resonant frequencies at 3 K. The orange bars are the dark resonators and the blue bars are the resonators coupled to a microlens. In the 40 K response the blackbody power is not large enough to see response from optically-coupled resonators relative to the dark resonators. In the 50 K data, we see most of the optically-coupled resonators shift to the left, indicating an optical response to the blackbody. The shift in response of the a few of the dark resonators have shifted to the left may be due to blackbody radiation reaching the the dark resonators, or

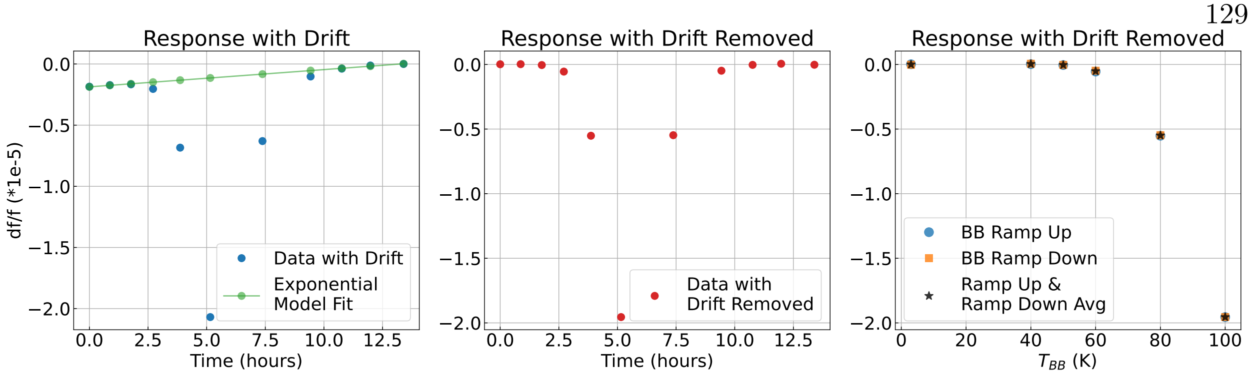

Figure 7.11: *Left*: The response of a resonator (blue dots), along with the exponential fit model (green dotted line). *Middle*) The response with the exponential fit subtracted out (red dots). The plot shows that the exponential fit worked well to remove the the time dependant resonance drift. *Right*: The response with the drift removed plotted as a function of blackbody temperature for the blackbody temperature ramp up (blue dots), ramp down (orange squares) and the average response of the ramp up and ramp down (black stars).

chip heating which creates thermally generated quasiparticles. We see that there is a noticeable difference in the response between the two type of resonators at 60, 80, and 100 K. The average response calculated from the distributions seen in the histograms for optically-coupled and dark resonators at 60, 80 and 100 K are listed in Table 7.1. This shows that the microlenses are focusing radiation onto the absorbers efficiently with responses greater than the dark resonators by a factor of 23, 60 and 54 at 60 K, 80 K, and 100 K, respectively. The dark resonators are known because they are within the expected resonant frequencies of the design dark resonators. In the following section we use these measured responses to calculate the responsivity of the PRIMA prototype array.

df/f Temp (K)	Optically-Coupled Resonators	Dark Resonators
60	-5×10^{-7}	-2×10^{-8}
80	-5×10^{-6}	-9×10^{-8}
100	-2×10^{-5}	-3×10^{-7}

Table 7.1: This table shows the average response at each blackbody temperature.

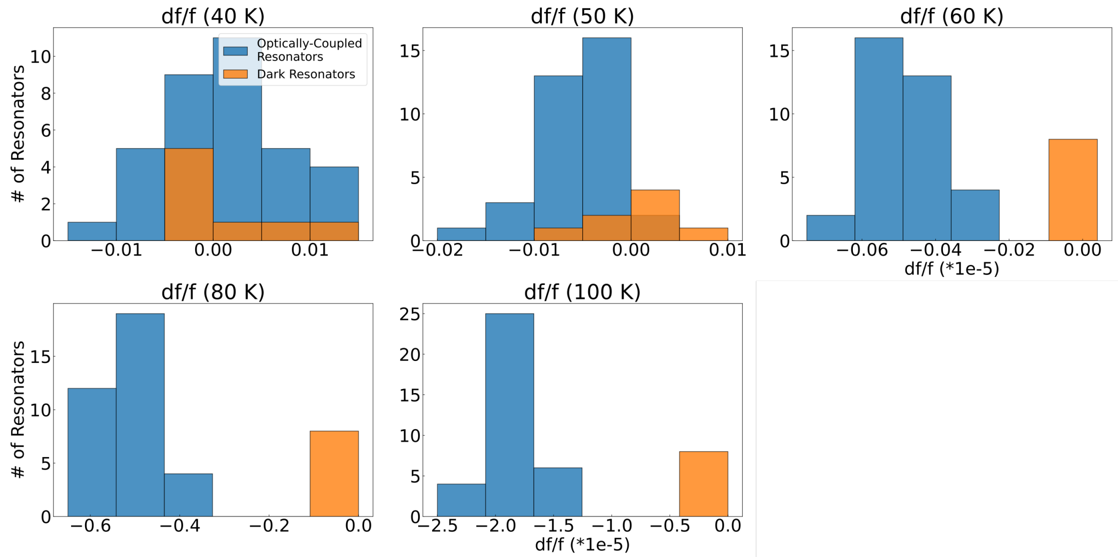

Figure 7.12: Histograms of the average fractional frequency response at each blackbody temperature relative to the resonant frequencies at 3 K. The orange bars are the dark resonators that are not coupled to a microlens. The blue bars are the resonators that are coupled to a microlens.

7.4.2 Measurement Results: Responsivities (R_x)

The absorbed blackbody power ($P_{BB,abs}$) for the experimental set up must first be calculated by taking the following integral over a given wavelength range,

$$P_{BB,abs} = A_{pixel}\Omega\eta_{opt}\int_{\lambda_i}^{\lambda_f} B(\lambda,T)F_\lambda\ A_\lambda\ ND_\lambda\, d\lambda, \tag{7.15}$$

where $A_{pixel} = 0.64$ mm^2 is the area of the microlens circular profile, $\Omega = 2\times10^{-6}$ is the solid angle subtended by the blackbody onto the microlens, and $\eta_{opt} = 0.55$ is the optical efficiency (Table 7.2), F_λ is the transmittance of the filter stacks as a function of wavelength, A_λ is the absorption efficiency of the inductor as a function of wavelength and ND_λ is the transmittance of a neutral density (ND) filter as a function of wavelength. Table 7.3 shows the calculated absorbed blackbody power. The spread in the R_x is likely due to the the placement of the detector along the array. Detectors in the middle of the array directly below the blackbody aperture will receive more power than the detectors at the edge of the chip, where the beam intensity decreases.

Efficiency description	value
Blackbody emissivity	0.8
Microlens efficiency	0.76
Blackbody aperture diffraction efficiency	0.9

Table 7.2: The efficiencies that make up η_{opt} for the BEGINS prototype array optical set up.

T_{BB} (K)	$P_{BB,abs}$ (fW)
3	9.2×10^{-29}
40	4.6×10^{-4}
50	8.2×10^{-3}
60	5.6×10^{-2}
80	6.4×10^{-1}
100	2.8

Table 7.3: Cryogenic blackbody optical power absorbed by PRIMA KID prototype array. First column: the blackbody temperature. Second Column: The calculated power absorbed by each KID on the array.

The fractional frequency response as a function of $P_{BB,abs}$ was fit to Model 2 (Eq. 3.52) for all optically-coupled resonators. An example of the fits are shown for three resonators in Fig. 7.13 Left. Fig 7.13 Right shows the calculated responsivity for the three resonators. The responsivity was calculated using the method explained in Sec. 3.2.2 with Eq. 3.53. The responsivities at the low optical loading are in the range of 7.0×10^9 to 1.1×10^{10} W^{-1}. Fig. 7.14 shows histograms of R_x for all resonators at each $P_{BB,abs}$. The histograms show the variation in the responsivity across the array. The average responsivity of R_x at each $P_{BB,abs}$ is listed in Table 7.4. The decrease in responsivity is due to shorter quasiparticle lifetimes as the quasiparticle density increases with increasing absorbed optical power.

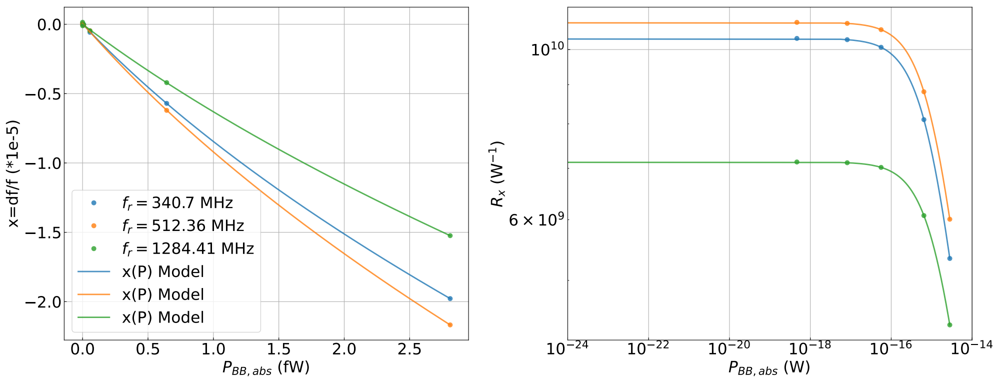

Figure 7.13: *Left*: The response of three resonators as a function of $P_{BB,abs}$. *Right*: The calculated responsivity for the three resonators as a function of $P_{BB,abs}$. The responsivity was calculated using the method explained in Sec. 3.2.2 with Eq. 3.53.

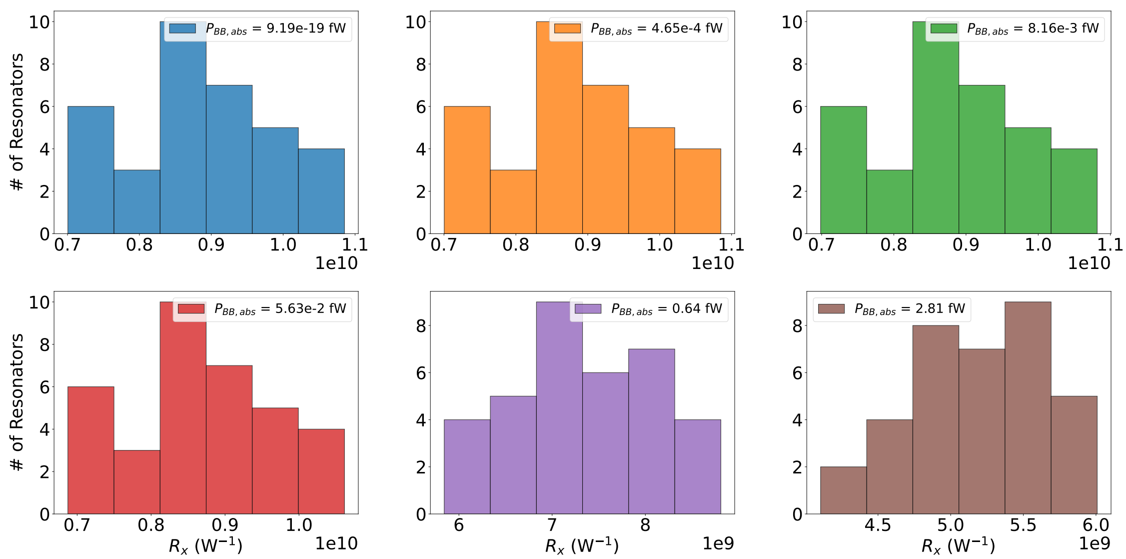

Figure 7.14: Histograms of R_x for all resonators at each $P_{BB,abs}$.

$P_{BB,abs}$ (fW)	Average R_x (10^9 W^{-1})
9.2×10^{-29}	8.8 ± 1.0
4.6×10^{-4}	8.8 ± 1.0
8.2×10^{-3}	8.8 ± 1.0
5.6×10^{-2}	8.7 ± 1.0
6.4×10^{-1}	7.4 ± 0.7
2.8	5.2 ± 0.5

Table 7.4: The average responsivity of R_x at each $P_{BB,abs}$.

7.4.3 Measurments Results: Noise PSDs S_{xx} & Empirical NEPs

Noise measurements were made on three resonators with $f_r = 340.7$, 512.36, and 1284.41 MHz to calculate empirical NEPs, and characterize TLS noise. The PSDs of the three resonators are shown in the left panel of Fig. 7.15, for blackbody temperatures of 3, 60, 73, 80, 89 and 100 K. The resonator with $f_r = 340.7$ MHz, only has PSDs for 3, 60, 80, and 100 K. The PSDs are shown for the frequency/phase (solid lines) and dissipation/amplitude (dashed lines) noise (discussion on PSD features in Sec. 5.3.3). The signature feature that indicates TLS noise is 1/f noise in the frequency noise which is only seen for resonators, $f_r = 341$ MHz and 1284 MHz from ~ 0.1 to 10 Hz. For $f_r = 341$ MHz at the 80 K and 100 K the white noise level, due to photon noise and G-R noise, dominates over the 1/f noise. Since the resonator at 1284.41 MHz has TLS noise present at each temperature it is used to set an upper limit on the TLS noise (S_{TLS}) of this prototype array. The upper limit is set by fitting the PSDs to the model discussed in Sec. 5.3.4. The results of the fits are discussed in Sec. 7.4.4, where the empirical NEPs are compared to the expected NEPs.

From the frequency noise PSDs shown in the left panel of Fig. 7.15 we calculated NEP_{freq} at 1 Hz (dark green dots), 10 Hz (cyan dots) and 100 Hz (pink dots) for each blackbody temperature. NEP_{freq} was calculated using the formula $NEP_{freq} = \sqrt{S_{xx}}/R_x$. This resulted in the empirical NEP_{freq} as a function of $P_{BB,abs}$ shown in the right panel of Fig. 7.15. The colored dots with a dashed line represent the the NEP_{freq} at 1 Hz (dark green dots), 10 Hz (cyan dots) and 100 Hz (pink dots). Since the 1/f noise was either not present or very low the NEP_{freq} values are similar at 1 Hz, 10 Hz and 100 Hz. All three resonators demonstrate an asymptotic behavior above 3×10^{-16} W that follows $NEP_{BB,photon}$, this shows that at high optical loading the resonators are photon-noise limited and that our system optical efficiency is well understood. At low powers the NEPs reach a minimum NEP of $\sim 6.5 \times 10^{-19}$, 9.5×10^{-18} and 1.5×10^{-18} W/$\sqrt{\text{HZ}}$ for $f_r = 340.7$, 512.36, and 1284.41 MHz, respectively. This indicates that there are other noise sources limiting the empirical NEPs such as TLS noise, G-R noise, microwave power quasiparticle generation noise, readout noise, and/or stray light in the cryostat. The expected KID absorbed optical load for

PRIMA is a few attoWatts with NEPs on the order of 2.5×10^{-19} W/$\sqrt{\text{Hz}}$ which are not met by the prototype array. The following section discusses what may be limiting the empirical NEPs.

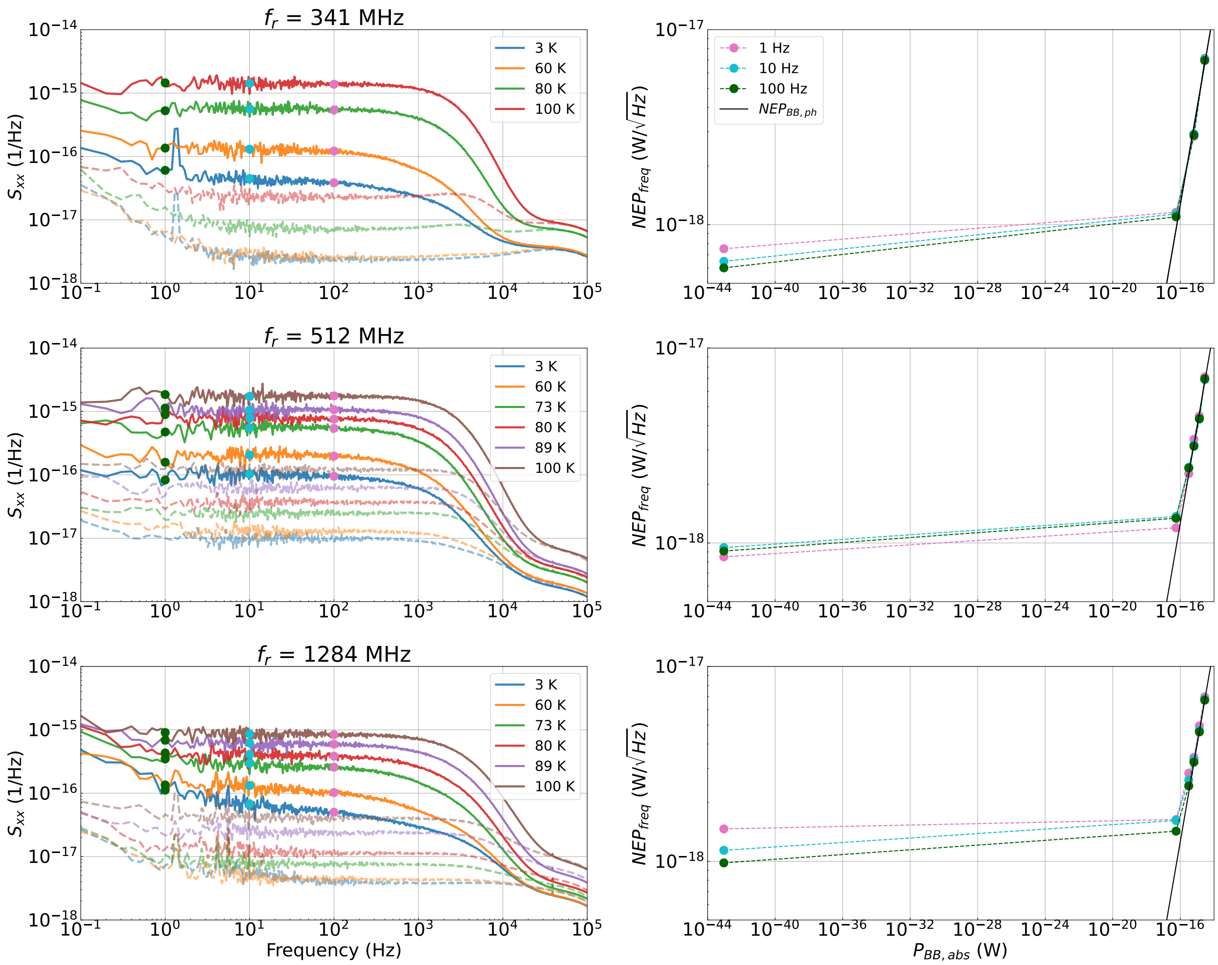

Figure 7.15: *Left*: Noise PSDs of three resonators with f_r = 340.7, 512.36, and 1284.41 MHz. The PSDs for each resonator are shown for blackbody temperatures of 3, 60, 73, 80, 89 and 100 K. The resonator with f_r = 340.7 MHz, only has PSDs for 3, 60, 80, and 100 K. *Right*: Empirical NEP_{freq} as a function of $P_{BB,abs}$. The colored dots with a dashed line represent the the NEP_{freq} at 1 Hz (dark green dots), 10 Hz (cyan dots) and 100 Hz (pink dots).

7.4.4 Results: Expected NEP vs. Empirical NEP

The estimated values from the measurements made to characterize the prototype array are used as input parameters to calculate the total expected NEP of the resonator at 1284.41 MHz. The input parameters are listed in Table 7.5. This resonator displayed the largest amount of TLS noise and was used to set an upper limit on the TLS noise. The value for S_{TLS} was estimated from a PSD fit at $T_{BB} = 3$ K which yielded $S_{TLS} = 8 \times 10^{-17}$ Hz^{-1} at 1 Hz (Fig. 7.15 Bottom Left). This is comparable to those found for PPCs in the BEGINS TiN KID which were on the order of 10^{-17}Hz^{-1}. The value for τ_{max} was also estimated from the PSD fit under the assumption that at 3 K $\tau_{max} \approx \tau_{qp}$. This was applied because τ_{max} is the maximum lifetime that quasiparticles have been observed to saturate to in the low temperature limit of dark measurements. Therefore, this assumption is only an approximation and may be underestimating τ_{max}. The fit yielded $\tau_{qp} \approx 40$ μs, which is much shorter than expected for aluminum of a few milliseconds. Short lifetimes around 150 μs were also measured by Elijah Kane on a prototype array from the same wafer [5] . At low temperatures impurities and disorder in superconductors have shown to reduce τ_{qp} [22, 6, 37]. The short lifetimes limit the responsivity and sensitivity of the detectors.

Fig. 7.16 shows the expected NEPs plotted as a function of absorbed optical power along with the empirical NEPs for $f_r = 1284.41$ MHz. The model agrees well with the empirical NEP at 1 Hz. The model indicates that TLS noise is the main source limiting the total NEP. Since $NEP_{TLS} \propto \frac{1}{R_x} \propto \frac{1}{\tau_{qp}}$, the short quasiparticle lifetimes are also liming the NEP. To address the short quasiparticle lifetimes we changed the fabrication method on a new prototype array to the method used on the aluminum KID arrays for the longer wavelength range of PRIMA. The longer wavelength range array employed electron beam lithography over UV stepper lithography and displayed lifetimes on the order of 1 ms. To address TLS noise we will test IDCs against PPCs on the same array to determine which reduces TLS noise. The responsivity will also be improved with a small volume absorber and adjusted absorption peak to be at 25 μm to increase responsivity.

[5] Value provided by Elijah Kane from Caltech through private discussion. His work on this measurement will be published in the *Journal of Low Temperature Physics.*

Table 7.5: Input Parameters for PRIMA KIDs Expected NEPs

Symbol	Parameter	Value	Source
f_r	resonant freq	1284.41 MHz	measured
ν	optical freq	12.5 THz	known
$Q_{i,0}$	Internal quality factor	8×10^4	estimated from S_{21} fits
Q_c	Coupling quality factor	7×10^4	estimated from S_{21} fits
χ_g	generator efficiency	1	[108]
η_{pb}	Pair-breaking efficiency	0.57	[108]
τ_0	characteristic electron-phonon interaction time	438 ns	[51]
τ_{max}	max lifetime	40 μs	estimated from PSD fit
V	Inductor volume	17 μm^3	calculated
η_a	qp breaking Readout efficiency	.001	[44]
α	Kinetic inductance fraction	0.8	known
T_c	critical temperature	1.37 K	estimated from T_c fits
T_{oper}	bath temp	150 mK	known
S_{TLS}	TLS noise	9.2e-17 Hz^{-1}	estimated from PSD fit
P_g	Drive power	10 fW	known

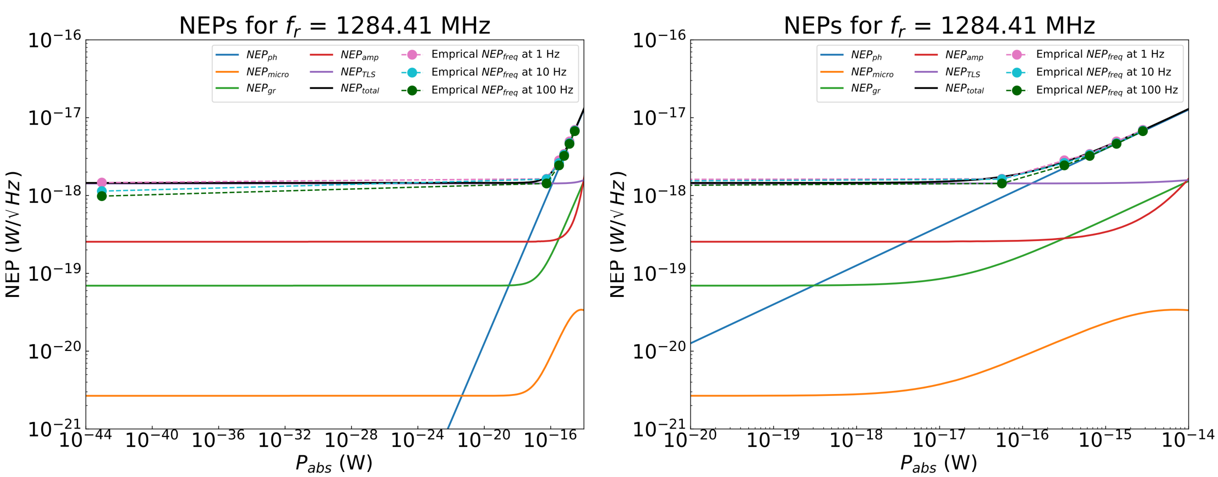

Figure 7.16: The expected NEPs plotted as a function of absorbed optical power along with the empirical NEPs for $f_r = 1284.41$ MHz. Both plots display the same data. The left plot shows the total expected NEP at the lowest optical load which agrees with NEP_{freq} at 1 Hz. The right plot is included to show that the total expected NEP and data also agree well at the higher optical loading.

7.5 Discussion and Future Work

In this chapter I have discussed the results of dark and optical measurements made on a 25 μm PRIMA KID prototype array coupled to a silicon microlens array. The goal of this work was to determine if the PRIMA NEP requirement of 2.5×10^{-19} W/$\sqrt{\text{Hz}}$ for an optical load of a few attoWatts was achievable in a lab set up. The most sensitive detector was photon-noise limited down to 0.1 fW with a limiting detector NEP of $\sim 6.5 \times 10^{-19}$ W/$\sqrt{\text{Hz}}$. Which indicates that we did not meet the PRIMA NEP requirements. We found that short quasiparticle lifetimes around 50-150 μs and TLS noise are limiting the NEP. To address the short quasiparticle lifetimes we changed the fabrication method on a new prototype array to the method used on the aluminum KID arrays for the longer wavelength range of PRIMA. The longer wavelength range array employed electron beam lithography over UV stepper lithography and displayed lifetimes on the order of 1 ms. Preliminary measurements of the new 25 μm prototype array have shown improved lifetimes around 1 ms and NEPs below the PRIMA requirement. The inductor volume of the new array was also decreased to improve responsivity. The analysis on this new prototype array is on-going. We will investigate TLS noise by testing IDCs against PPCs on the same array to determine which reduces TLS noise. Below I highlight the results of the dark and optical measurements made on this prototype array discussed in this chapter.

Dark measurements on the prototype array indicate $T_c = 1.37$ K, which is around the expected value for aluminum and similar to what was measured for GEP. The array had a high yield of 94 % with a frequency span close to the design frequency span. We also estimated high internal Qs of 1.7×10^5. High internal quality factors indicate that there is low dissipation loss in the resonator. The dark measurements were important to use as input parameters in the sensitivity model and show that the prototype array does not deviate from design expectations.

Highlight optical measurement results:

(1) The KIDs employ an inductor designed to have an absorption peak at 25 μm in both polarizations. FTS measurements were made on a 1-inch sample with the aluminum inductor

trace on a Si substrate to measure the absorption. We found that the fabricated inductor had an absorption peak of 70-75 % at 22 μm in both polarizations. The next generation of prototype arrays have the absorption peak adjusted to 25 μm to improve the response of the detectors.

(2) We found that the fractional frequency response as a function of absorbed optical power fit Model 2, derived in Sec. 3.2.2, well. This was also confirmed in the BEGINS chapter which shows this model is reliable for estimating the R_x of KIDs.

(3) An upper limit on the TLS noise of the prototype array was set by fitting the noise PSD of the KID displaying the largest amount of TLS noise (f_r = 1284.41 MHz). We found $S_{TLS} = 9.2 \times 10^{-17}$ Hz^{-1} at 1 Hz. The fit also estimated a short $\tau_{qp} = 40$ μs. A short lifetime of 150 μs was also estimated on an array from the same wafer by Elijah Kane at Caltech.

(4) The sensitivity model agreed well with the empirical NEP at 1 Hz. The model indicated that TLS noise and short quasiparticle lifetime are the main sources limiting the total NEP.

(5) The optical measurements show the Si microlens array developed at GSFC was a success and performed well in focusing radiation onto the absorbers of the KIDs. This enables a compact design at the focal plane of the instrument.

Chapter 8

Linear Variable Filter Development for BEGINS

Observations in the far-IR require optical filters to define the instrument bands of observatories with a specific resolving power (or spectral resolution) $R = \lambda_0/\Delta\lambda$, where λ_0 is the bandpass peak wavelength. Metal-mesh filters have been studied for far-IR instruments since the first publication by Ulrich [100]. The simplest form consist of a single layer of metal-mesh which can be free-standing or deposited on a substrate. The mesh consists of a periodic structure the geometry of which determines whether the filter is a low-pass, high-pass or bandpass filter. Due to their compactness and ease of fabrication scheme we have chosen metal-mesh bandpass filters (MMBP) to define the BEGINS and PRIMA instrument bands. Our goal is to create a linear variable filter (LVF) made up of MMBPs, with a bandpass that varies linearly along one direction of the filter (Fig. 8.1). The LVFs will enable hyperspectral imaging from 25 μm to 65 μm with a lower limit resolving power of R=7.5 and target R=10 and multispectral imaging for wavebands centered at 70, 100, 160, and 250 μm with R = 3-6 (discussed in Sec. 1.3.1.1).

In this chapter I will discuss how we simulate the filters to determine the cross-slot parameters before fabrication; I will present a transmission line model for the filters; and I will discuss the results of transmission measurements of a 44 μm MMBP and a BEGINS prototype LVF and how they compare to the modeled filters. The work on the 44 μm MMBP was preliminary works towards the development of the LVF. This wavelength range was also investigated for the future high priority flagship mission Uranus Orbiter and Probe which will carry a net flux radiometer (NFR) to study the in situ heat flux of the icy giants atmosphere to 10 bar pressure[4, 77]. The NFR will measure

Uranus's net radiation flux in seven spectral bands, spanning solar to infrared wavelengths (0.2 μm to 300 μm) [4]. All simulations and measurement analysis were performed by me, all fabrication was performed by Kevin Denis at the GSFC DDL, and all filter transmission measurements were made by the GSFC Optics Group.

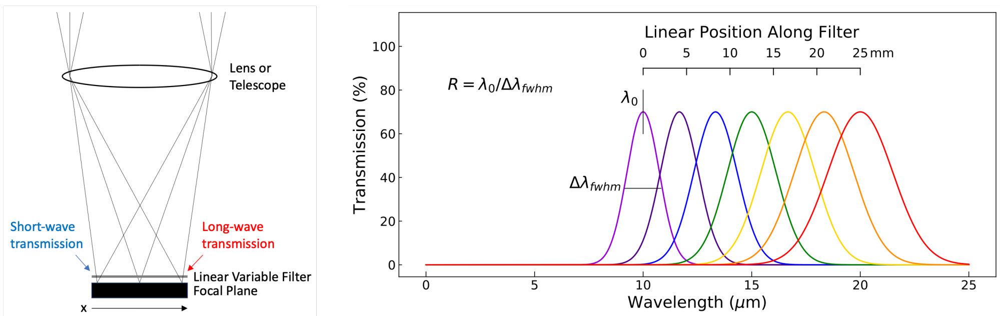

Figure 8.1: *Left*: A schematic showing how a continuous LVF is placed in an imaging optical system to create a spectral mapper. The LVF is placed directly in front of the focal plane array. *Right*: A schematic of the spectral transmission for the LVF. The bandpass central wavelength λ_0 varies continuously and smoothly along the filter length [41]

.

8.1 MMBP Cross-Slot Geometry and Transmission Profile

The transmission profile of a MMBP is similar to a Lorentzian with asymmetry, explained later in the chapter, and is determined by its cross-slot parameters; the periodicity (G), the cross length (K) and the cross width (B) (Fig. 8.2) [99, 88, 75, 73, 74]. The bandpass center peak scales with K (the cross length) and the bandwidth becomes small as the ratios of G/K and G/B increase [88]. The filters discussed in this chapter are made of thin film gold and supported by a silicon (Si) substrate. Gold was chosen because of its low resistivity which allows for high transmission. We use high-resistivity floatzone Si wafers for low dielectric loss. For the LVFs the cross-slots vary in sizes along the length of the silicon (Si) substrate.

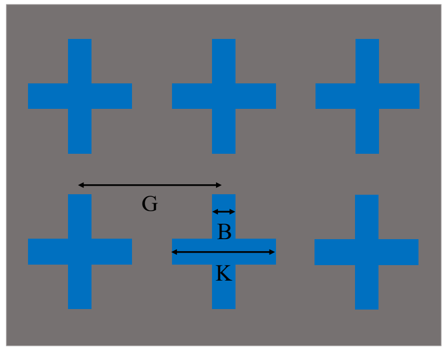

Figure 8.2: Illustration of metal-mesh cross-slot parameters. G is the periodicity, K is the cross-length and B is the cross-width. Gray represents gold film. Blue represents bare Si substrate.

8.2 Filter Methodology

In this section I present two methods of modeling the metal-mesh bandpass filters, electromagnetic simulations and a transmission line model.

8.2.1 Ansys HFSS Simulation Method

In order to predict and model the MMBP performance we used Ansys High Frequency Structure Simulator (HFSS)[1] software. HFSS, is a full-wave frequency domain electromagnetic field solver based on the finite element method and numerically solves Maxwell's equations across a specified frequency range for a specified structure geometry, material configuration, and boundary conditions. HFSS is used to extract S-parameters and predict the transmission profiles of the metal-mesh filters. Through symmetry, an array of cross apertures in a gold film on a Si substrate can be simulated by a single unit cell with perfect electric ($\vec{E}$) and magnetic ($\vec{H}$) field boundary conditions [74, 88]. The unit cell structure is shown in the left panel of Fig. 8.3. Wave ports in vacuum at the top and bottom of the unit cell are used to simulate a normal incident wave. A wave port is equivalent to a semi-infinite waveguide. Since the cross has four-fold symmetry we only used a quarter of the structure shown in the left panel of Fig. 8.3, as seen in the right panel

[1] `https://www.ansys.com/products/electronics/ansys-hfss`

of Fig. 8.3, to reduce the simulation time.

The gold is modeled with bulk conductivities at room and cryogenic temperatures. The room temperature conductivity is determined from DC resistivity measurements of the gold film used to fabricate the filters. The cryogenic bulk conductivity is calculated using the DC residual resistivity ratio (RRR) of the gold film which is the ratio of the electrical resistance of a metal measured at room temperature and 4.2 K.

The dielectric permittivity of the Si substrate is set to $\epsilon_{Si} = 11.7$. There is ~0.3 reflectance at each vacuum-Si interface, so we implemented quarter-wave AR coatings on both the metal-mesh side and on the back side of the filter. To assess the effect of the quarter-wave filters we ran simulations of the structure shown in the right panel of Fig. 8.3.

The cross-slot parameters are initially calculated using formulae from the literature [73, 75], given the desired bandpass center wavelength (λ_0). The cross length parameter K is approximately $\lambda_0/2$, where λ_0 is the band center wavelength in the medium, in this case silicon ($n_{Si} = 3.42$). The estimated parameters are then optimized using simulations to achieve the desired bandpass profile. The simulations will be thoroughly investigated against transmission measurements in Sec. 8.4.2.

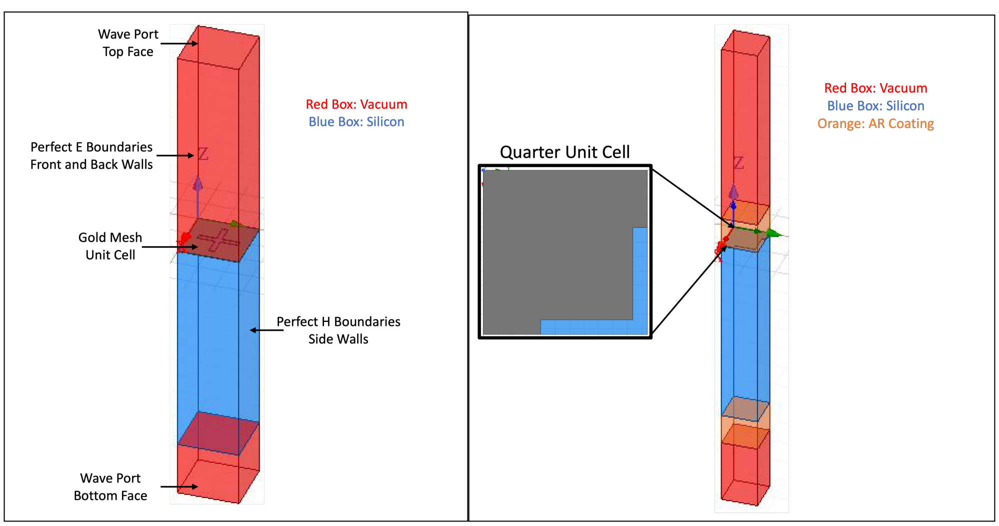

Figure 8.3: *Left*: 3D model of an HFSS unit cell simulation for a non-AR coated MMBP. *Right*: 3D model of an HFSS unit cell simulation for a double sided AR coated MMBP. The quarter unit cell is used to reduce the simulation time. For illustration purposes, the vacuum, Si substrate and AR coating box heights are not to scale.

8.2.2 Transmission Line Model

Another method used to model the transmission of the metal-mesh filters is an analytical transmission line model. The transmission line model provides a faster method to determine how the losses due to the resistivity of the gold film or the dielectric substrate will affect the transmission profile of the filter. It can also be used to model the effect of AR coatings.

The metal-mesh cross-slots are self-resonant structures with an impedance that can be modeled as a passive LRC circuit [19, 88, 3]. The reactive part of the LRC circuit determines the shape of the bandpass. The real part, while still contributing to the bandwidth, is responsible for the losses in the circuit due to ohmic losses. The transmittance of our filters is modeled by using the transmission line model shown in Fig. 8.4, where $Z_0 = 377\ \Omega/\text{sq}$, is the characteristic impedance of free-space. The Si is modeled as a transmission line with length equal to thickness of the Si substrate and characteristic impedance, $Z_{\text{Si}} = Z_0/\sqrt{\epsilon_{Si}} = 110\ \Omega/\text{sq}$. An expression for the reflection coefficient of the transmission line model can be derived to model the transmission of the filters. This derivation discussed is based on the transmission line model used by Al-Azzawi, et al.[3].

The impedance of the LRC circuit is given by

$$Z_{LRC} = \frac{R + j\omega L}{1 + j\omega RC - (\omega/\omega_0)^2}, \tag{8.1}$$

where R is the resistance, C is the capacitance, L is the inductance, ω is the angular frequency and ω_0 is the is the circuit resonant angular frequency. The input impedance at the bottom of the Si substrate looking towards the mesh is then given by [89]

$$Z_{Load} = Z_{Si}\frac{Z_0 + jZ_{Si}\tan((\alpha_{Si} + j\beta_{Si})l_{Si})}{Z_{Si} + jZ_0\tan((\alpha_{Si} + j\beta)l_{Si})}, \tag{8.2}$$

where l_{Si} is the Si thickness and $\beta_{Si} = \frac{2\pi}{\lambda_{Si}}$ is the wave-number, $\lambda_{Si} = \frac{\lambda}{n_{Si}}$ is the wavelength in the Si substrate, and α_{Si} is the attenuation constant due to any dielectric losses. The load impedance and equivalent impedance of the LRC circuit (Z_{LRC}) are in parallel with an equivalent impedance of

$$Z_{eq} = \frac{Z_{Load} * Z_{LRC}}{Z_{Load} + Z_{LRC}}. \tag{8.3}$$

The reflection coefficient, Γ, is given by

$$\Gamma = \frac{Z_{eq} - Z_0}{Z_{eq} + Z_0}. \tag{8.4}$$

The transmittance, or the fraction of incident power transmitted, is $|T|^2 = 1 - |\Gamma|^2$. This transmission line model is used to fit the output of the HFSS simulated transmission of the MMBP to estimate R, C and L of the filter and compared to transmission measurements.

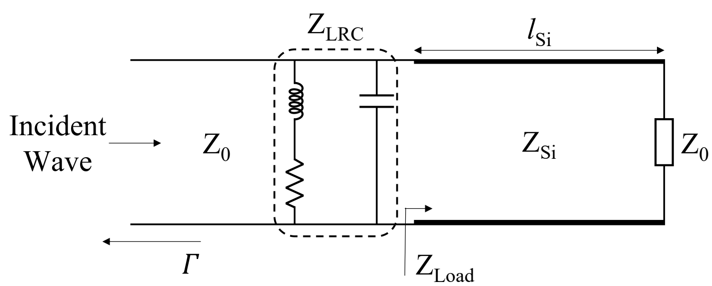

Figure 8.4: Transmission line model representation of a MMBP on a Si substrate. Z_0, is the impedance of free-space, Z_{LRC} is the impedance of the MMBP, Z_{Si} is the impedance of Si, Z_{Load} is the load impedance at the beginning of the Si transmission line of length, l_{Si}. Γ, is the reflection coefficient used to calculate the fraction of incident power transmitted from the incident wave.

The same method can be used to derive the reflection coefficient for a transmission line model that includes the AR coatings to increase the transmission of a filter. Similar to the Si substrate, the AR coatings are modeled as a transmission line with length equal to thickness of the AR coatings and characteristic impedance $Z_{AR} = Z_0/\sqrt{\epsilon_{AR}}$, where ϵ_{AR} is the relative permittivity of the AR coating material. Fig. 8.5 shows the process used to derive the reflection coefficient. Starting at the input to the transmission line on the left, we calculate the load impedance due to the first AR coating layer,

$$Z_{Load\ 1} = Z_{AR} \frac{Z_0 + jZ_{AR} \tan((\alpha_{AR} + j\beta_{AR})l_{AR})}{Z_{AR} + jZ_0 \tan((\alpha_{AR} + j\beta_{AR})l_{AR})}, \tag{8.5}$$

where l_{AR} is the AR coating thickness, $\beta_{AR} = \frac{2\pi}{\lambda_{AR}}$ is the wave-number, $\lambda_{AR} = \frac{\lambda}{n_{AR}}$ is the wavelength in the AR coating, and α_{AR} is the attenuation constant due to any losses in the AR coating. Next the load impedance due to the Si transmission line is calculated,

$$Z_{Load\ 2} = Z_{Si} \frac{Z_{Load\ 1} + jZ_{Si} \tan((\alpha_{Si} + j\beta_{Si})l_{Si})}{Z_{Load\ 1} + jZ_0 \tan((\alpha_{Si} + j\beta_{Si})l_{Si})}. \tag{8.6}$$

Now $Z_{Load\ 2}$ and Z_{LRC} are added in parallel,

$$Z_{eq,AR} = \frac{Z_{Load\ 2} * Z_{LRC}}{Z_{Load\ 2} + Z_{LRC}}. \tag{8.7}$$

Finally, the load impedance due to the second AR coating can be calculated,

$$Z_{Load\ 3} = Z_{AR} \frac{Z_{Eq,AR} + jZ_{AR} \tan((\alpha_{AR} + j\beta_{AR})l_{AR})}{Z_{AR} + jZ_{Eq,AR} \tan((\alpha_{AR} + j\beta_{AR})l_{AR})}. \tag{8.8}$$

The reflection coefficient is then

$$\Gamma = \frac{Z_{Load\ 3} - Z_0}{Z_{Load\ 3} + Z_0}. \tag{8.9}$$

The transmittance is calculated in the same manner as above.

In Sec. 8.4.3 the transmission line model is fit to the output of the HFSS simulated transmission where the resonant frequency, sheet resistance and capacitance are free parameters. The resulting fit transmission is compared to the measured transmission. We learn that the transmission line model can be used to determine how resistive losses, dielectric losses and losses in the AR coatings will change the peak transmission of the bandpass.

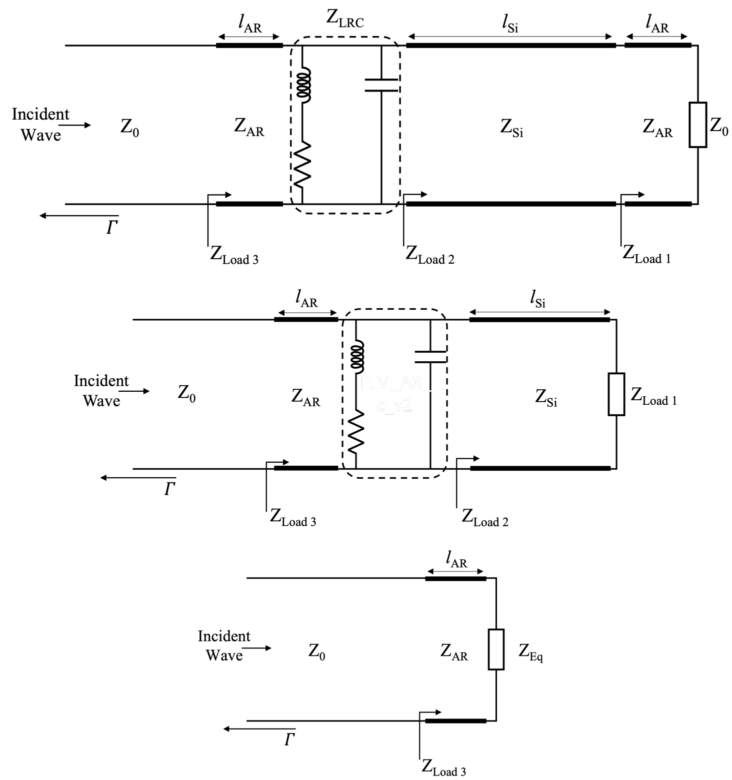

Figure 8.5: Transmission line model of a MMBP on a Si substrate with AR coatings. The figure shows how the transmission line model simplifies as the steps are taken to derive Γ.

8.3 FTS Transmission Measurement Setup

The transmission measurements were made using a Bruker Optics – IFS 125HR, which is a high resolution Fourier transform infrared spectrometer (FTS) (Fig. 8.6 left panel). Measurements were made at 5 K and at room temperature. The filters are placed in a sample holder, shown in Fig. 8.6 right panel. An aperture is placed in front of the holder to control the beams size. The sample holder with both the filter and an open aperture is attached to a rod which can be moved through the optical path. First, a reference spectrum is collected for the open aperture (without filter). Then, for the linear variable filters the rod is moved down manually in segments to measure the transmission of the varying bandpasses along the filters. The transmission spectra is then calculated by taking the ratio of the beam spectrum going through the filter divided by the reference beam spectrum going through the hole.

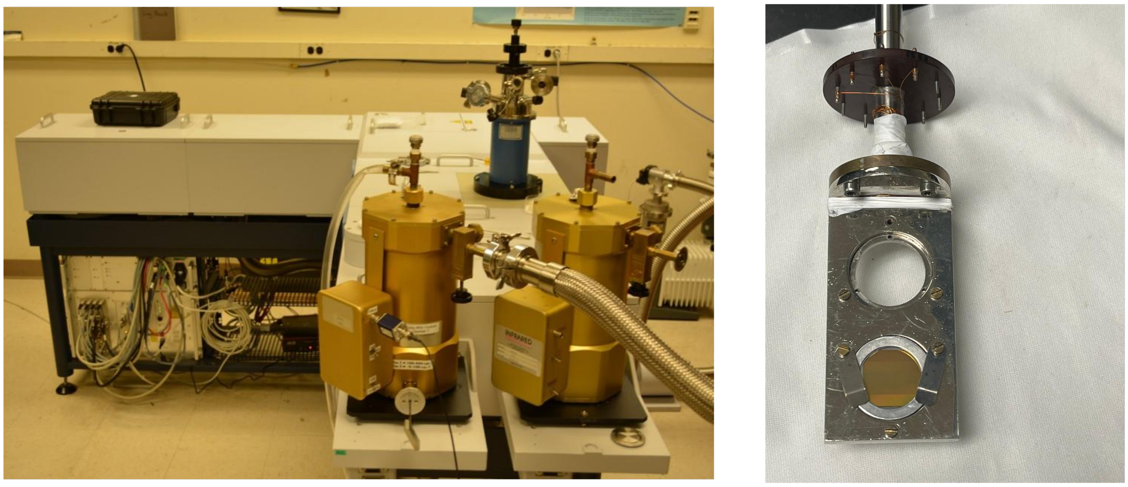

Figure 8.6: *Left*: Bruker Optics – IFS 125HR, a high resolution Fourier transform infrared spectrometer. This instrument was used to make the transmission measurements of the metal-mesh filters. *Right*: Sample holder used to hold the metal-mesh filters in the optical set up.

8.4 44 μm BP

In this section I present the development of a prototype 44 μm MMBP filter including simulations, fabrication, and measurement results. The simulations are compared to measurements of the fabricated filters and fit to the transmission line model. All simulations and measurement analysis were performed by me, fabrication was performed by Kevin Denis at the GSFC DDL, and filter transmission measurements were made by the GSFC Optics Group.

8.4.1 44 μm MMBP Design and Fabrication

The 44 μm MMBP was fabricated in a simple single layer process. Double side polished intrinsic float zone silicon wafers ($\rho > 20$ kΩ-cm) were coated with a 5 nm thick Ti adhesion layer and 100 nm thick gold layer by electron beam evaporation in the GSFC Detector Development Laboratory (DDL). Table 8.1 shows the filter design parameters. Gold was chosen as the mesh material because of its low resistivity which minimizes ohmic losses. It is also ~5 times thicker than the skin depth of gold at the desired bandpass frequency, making the Au layer optically thick.

The sheet resistance of the gold was measured to be 0.3 Ω/sq at 300 K which for 100 nm thick gold corresponds to 3.33×10^7 S/m. It has minimum features of 1 μm which were lithographically patterned by a Heidelburg DWL 66+ direct write laser system and a single layer of S1805 resist. The gold was etched by argon ion milling (4-Wave) and the titanium was further etched by a combination of fluorine plasma and hydrofluoric acid. Several filters were fabricated on a single 100 mm silicon wafer. After etching, the photoresist was removed by oxygen plasma and solvent cleaning.

Next, the filters were coated with cyclic olefin copolymer (COC) on both sides of the wafer to serve as a low-loss AR coating. COC has a low index of refraction ($\sim$1.5) that provides low reflective loss over a modest bandwidth at the vacuum-to-Si interfaces [106]. In the simulations, the COC-AR coatings are defined as $\lambda_0/4$ thick volumes with a relative dielectric permittivity of 2.37 [106]. From the simulation we found that the addition of the AR coatings causes the original bandpass peak to shift to longer wavelengths by $\sim$ 1 μm because of a change in the effective capacitance of the MMBP. This shift was taken into consideration when choosing the design cross-slot parameters in Table 8.1.

A scanning electron microscope (SEM) image of the fabricated filter is shown in Fig. 8.7. The fabricated cross-slot parameters were measured over various positions along the filter and averaged (Table 8.2). The fabricated cross-slot parameters were similar to the design parameters and should not cause a significant difference in the transmission of the filter. However, a close up SEM image of one of the cross-slots shows the fabricated filter has rounded inner and outer edges. The rounded corners were measured to have a radius of curvature of $\sim$0.5 μm and do cause a difference between the simulated and measured transmission which is discussed in detail in the following section.

Table 8.1: Filter properties and design parameters for a bandpass filter with peak transmission at 44 μm.

Feature	Dimensions
Silicon substrate thickness ($\epsilon_{Si} = 11.7$)	540 μm
Au film thickness ($R_s = 0.3$ Ω/sq)	100 nm
Cross pitch	11.4 μm
Cross length	7.5 μm
Cross width	1.0 μm
$\lambda/4$ COC anti-reflection coating thickness (ϵ_{COC}=2.37)	7.2 μm

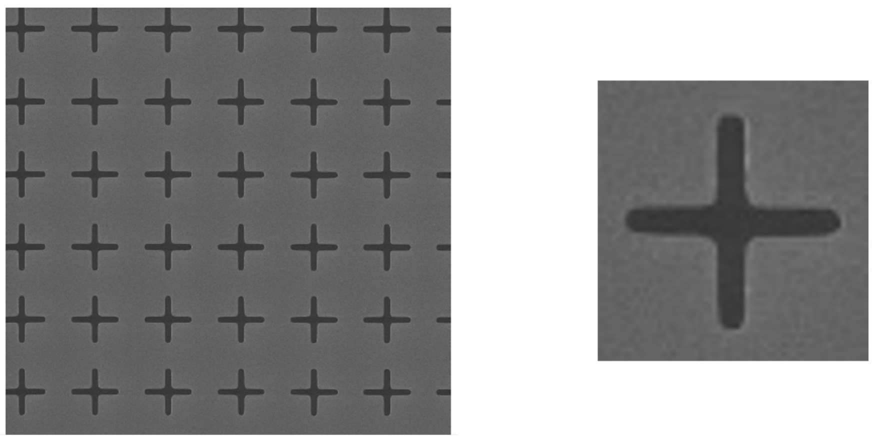

Figure 8.7: Scanning electron microscope (SEM) image of the fabricated 44 μm MMBP with cross-slot parameters presented in Table 8.1. The light gray is gold metal film and the dark gray is bare Si. The fabricated MMBP filter has rounded inner and outer edges with radius of curvature $\sim$0.5 μm.

Table 8.2: 44 μm MMBP design vs fabricated cross parameters.

Cross Parameter	Designed (μm)	Fabricated (μm)
Horizontal cross length	7.5	7.52$\pm$0.04
Vertical cross length	7.5	7.50$\pm$0.06
Horizontal cross width	1.0	1.03$\pm$0.03
Vertical cross width	1.0	1.05$\pm$0.03

8.4.2 Comparison of Simulations to Measurements

Only room temperature FTS measurements were made on non-AR coated and COC-AR coated 44 μm MMBPs since liquid helium was not available at the time. The measurements were made with an FTS resolution of 1 cm^{-1} and 2 mm aperture. Fig. 8.8 shows the measured filter transmission and the design HFSS simulated transmission.

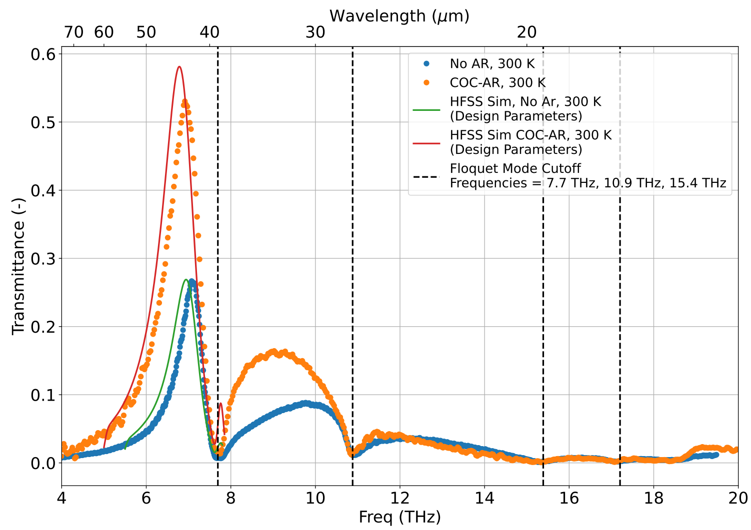

Figure 8.8: 300 K measured and simulated transmission of the non-AR coated and COC-AR coated 44 μm MMBP. Solid lines: HFSS simulated transmission using design cross parameters listed in table 8.1. Dotted lines: FTS measured transmission.

The measured filters (dotted lines) show what are referred to as grating lobes at high frequencies above the bandpass. The grating lobes occur because the periodic cross-slots act as a diffraction grating that diffracts a wave when the lattice size (or periodicity) is electrically large. The location of the grating lobe frequency cut-offs, where the transmission is nearly zero in the plot, can be predicted using Floquet's Theorem [13]. Since the mesh is periodic only one period of the structure, referred to as the unit cell, needs to be examined to determine the behavior of the electromagnetic fields in the mesh. In Floquet theory this is done by applying a periodic function to a uniform plane wave incident on the periodic structure and applying periodic boundary conditions. For a 2D structure this yields a set of solutions known as Floquet modes which are plane waves referred to as Transverse Electric (TE_{mn}) or Transverse Magnetic (TM_{mn}) modes.

For a normal incident wave these set of modes have frequency cut-offs that are determined by the following equation [13],

$$f_{c,mn} = \frac{c}{2\pi\sqrt{\epsilon_r}}\sqrt{\left(\frac{2\pi m}{G_x}\right)^2 + \left(\frac{2\pi n}{G_y}\right)^2}, \tag{8.10}$$

where c is the speed of light, ϵ_r is the relative permittivity of the medium which in our case is Si and G_x and G_y are the cross pitch in the x and y direction. The black dashed lines indicate the expected frequency cutoffs for Floquet modes $TE_{10/01}$, TE_{11}, $TE_{20/02}$ and $TE_{21/12}$. The same frequency cutoffs would apply to the TM modes. For a cross pitch of 11.4 μm the frequency cutoffs are at 7.7 THz, 10.9 THz, 15.4 and 17.2 THz. As shown in the plot, there is excellent agreement between predicted and measured cutoff frequencies. The relative power distribution between the bandpass peak and the first three lobes shown in the plot is determined by finding the normalized area under the curves of the bandpass peak and the grating lobes. Table 8.3, shows the power distribution for the non-AR coated filter. Only about half of the power goes into the bandpass peak while the other half is primarily distributed between the first two grating lobes. This is undesirable, because a broadband KID inductor/absorber will absorb a comparable amount of radiation in an undesired wavelength range. A technique used to block or reduce the transmission of the grating lobes are filters with multiple mesh layers.

Table 8.3: Power distribution between the bandpass peak and grating lobes of the non-AR coated 44 μm MMBP.

Transmission Feature	Relative Power (%)
Bandpass Peak	45.4
Lobe 1	34.5
Lobe 2	18.4
Lobe 3	1.7

Differences in the simulated and measured transmission are also shown in Fig. 8.8. The non-AR coated 44 μm MMBP was designed to have a band-pass peak at 7 THz with a resolving power (or spectral resolution), R$\sim$9. However the measured filter has a bandpass peak at a slightly higher frequency (7.1 THz) with a higher resolving power (R$\sim$11). The transmission of the measured filters is also less than the simulations transmission with an average error of 6.1 %. These differences are also seen for the COC-AR coated sample. Table 8.4 lists the bandpass peak, resolving power, peak transmission, and the average percent error between the measurements and simulations for the FTS measurements and the HFSS simulations. The discrepancies are likely due to the cross-slot rounded corners in the fabricated filter shown in Fig. 8.7. We expect this to change the transmission profile because it changes the capacitance and inductance of the filter which leads to a change in the resonant frequency, since $f \propto 1 \sqrt{LC}$.

Table 8.4: 44 μm MMBP HFSS simulated vs. measured bandpass peak, resolving power, and transmission.

	Filter Type	Peak Center (THz)	R = $\lambda/\Delta\lambda$	Peak Trans (%)
FTS Measurement	300 K COC-AR	7.0 (43.4μm)	8	53
	300 K No-AR	7.1 (42.4 μm)	11	27
HFSS Sim	300 K COC-AR	6.8 (44.2 μm)	7	58
	300 K No-AR	7.0 (43.2 μm)	9	28
Avg Error (%)		2.2	18.3	6.1

To determine the effects of the rounded edges three different simulations were run. The left panel of Fig. 8.9 shows different quarter unit-cells investigated one with rounded inner edges, one with rounded outer edges and one with both inner and outer rounded edges. The right plot in Fig. 8.9 shows the change in the simulated filter transmission for each unit cell. Note that the fringing along the transmission profile is due to the Si cavity created between the metal-mesh and the vacuum interface on the opposite side, which was resolved by the FTS. The simulation fringing was smoothed to approximate the resolution of the FTS. When the the inner edges are rounded there is an increase in transmission because the area of the slot increases. There is also a slight shift in the bandpass peak to higher frequency, by 0.1 THz. For a cross-slot with only rounded outer edges, the transmission decreases due to a decrease in the slot area with a shift to higher frequency as well but it still does not match the measured bandpass peak. The bandpass peak shifts to higher frequencies because the rounding of the edges decreases the capacitance. When both the inner and outer edges are rounded the simulated transmission aligns better with the FTS measurement. The bandpass peak is at 7.1 THz, with a transmission of 26% and resolving power of ∼11, which is very similar to the measured filter.

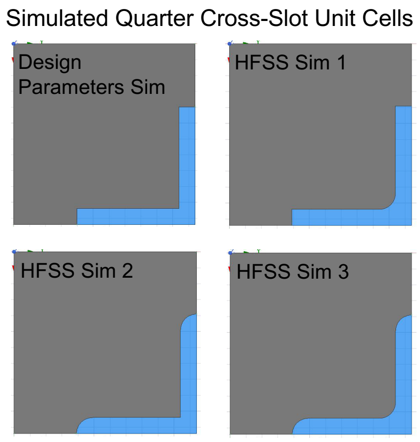

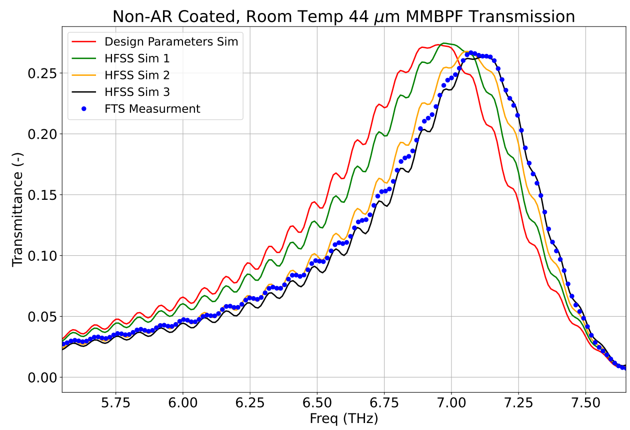

Figure 8.9: *Left*: The HFSS simulated quarter cross-slot unit cells of the simulated transmission shown in the right plot of Fig. 8.9. *Right*: HFSS simulated and FTS measured transmittance of the non-AR coated, room temperature 44 μm MMBP. Red Line: HFSS unit cell with cross-slot parameters in Table 8.1. Green Line: HFSS Sim 1 has rounded inner corners (radius of curvature = 0.5 μm). Orange Line: HFSS Sim 2 has rounded cross-ends (radius of curvature = 0.5 μm). Black Line: HFSS Sim 3 has rounded cross-ends and inner corners (radius of curvature = 0.5 μm). Blue: FTS measured transmission of fabricated 44 μm MMBP. The fringing along the transmission profile is due to the Si cavity created between the metal-mesh and the vacuum interface on the opposite side. The FTS resolution was small enough to barely resolve the fringes. In order for the simulations to match this, they were smoothed using a Gaussian filter to approximate the FTS apodization and resolution.

Table 8.5: The band-pass peak, resolving power, and transmission of HFSS Sim 1, HFSS Sim 2, HFSS Sim3, and FTS measured performances shown in Fig. 8.9 *Left* of the room temperature, non-AR coated 44 μm MMBP.

	HFSS Sim 1	HFSS Sim 2	HFSS Sim 3	FTS Measurements
Peak Center (THz)	7.0 (43 μm)	7.0 (43 μm)	7.1 (42 μm)	7.1 (42 μm)
$\lambda/\Delta\lambda$	9	10	11	11
Peak Transmission (%)	28	27	26	27

Since HFSS Sim 3 matched the non-AR coated measurement so well, COC-AR coatings were applied to HFSS Sim 3 to compare to the AR coated measurements. The results are shown in Fig.

8.10. The green line shows that HFSS Sim 3, does match the peak location better than the design parameter simulation (orange line). The peak location of HFSS Sim 3 with the AR coatings is 43.2 μm which is a 0.5% difference in comparison to the FTS measurement. The resolving power (R=9) was still approximated to be within an 11.0% difference from the FTS measurement. The simulated peak transmission decreased from 58% to 56% which is still higher than the measured transmission of 53 %. Differences may be due to non-uniformity in the filters fabricated across the same wafer. These simulations along with non-AR coated simulations demonstrate how the filter's response is sensitive to changes in the cross-slot features and incorporating them allows us to model our measurements more accurately.

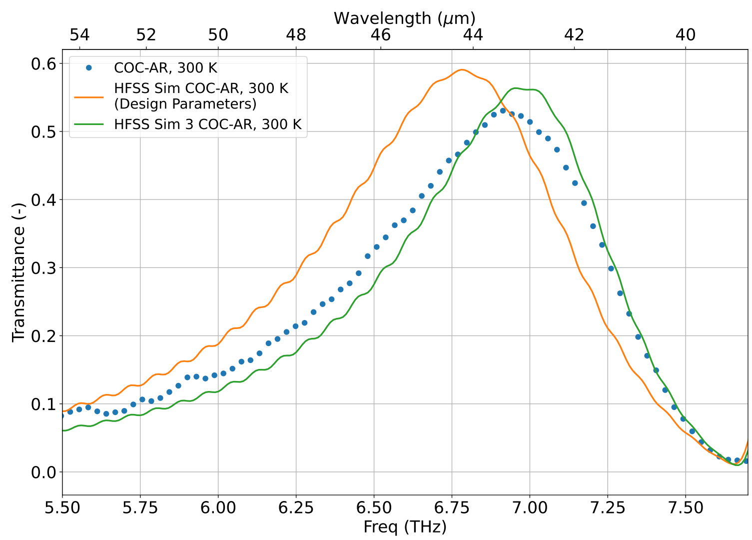

Figure 8.10: Orange: HFSS simulated transmission of a room temperature COC-AR coated 44 μm MMBP with the design parameters. Bandpass peak = 6.8 THz (44.2 μm), peak transmission = 58%, and resolving power = 7. Green: HFSS simulated transmission of a room temperature COC-AR coated 44 μm MMBP with the cross-slot unit cell used in HFSS Sim 3. Bandpass peak = 7.0 THz (43.2 μm), peak transmission = 56%, and resolving power = 9. Blue Dots: FTS measurement of the COC-Ar coated 44 μm MMBP.

8.4.3 Transmission Line Model Fitting to Simulations

The transmission line model without AR coatings, described in Sec. 8.2.2, was fit to HFSS Sim 3 in Fig. 8.9. The fit has three fit parameters: f_0 the resonant frequency, R and C. L is not a fit parameter because it can be rewritten is terms of C and f_0, where $L = \frac{1}{(2\pi f_0)^2 C}$. A second fit was performed with only two free parameters, f_0 and C, while R was fixed to match the DC resistance of the gold film, 0.3 Ω/sq. The fit results are shown in the left plot of Fig. 8.11. In both fits the bandpass frequency is fit well. However, the fringe amplitudes on either side of the bandpass peak are not well fit. This means our transmission line model does not fully capture the impedance mismatch at the metal-mesh and Si interface. The model is also unable to capture the asymmetry of the filter's transmission profile due to the higher order grating lobes. The right plot of Fig. 8.11 compares the smoothed fits to the smoothed HFSS Sim 3 and the FTS measurement. Since the model does not incorporate the affects of the grating lobes the bandwidth is larger than HFSS Sim 3 and the FTS measurement. The maximum transmission is fit well when R is fixed to 0.3 Ω/sq. When R is a free parameter it is estimated to be 2.75x10^{-1} Ω/sq, which leads to a slightly larger maximum transmission. This further confirms the DC measurement of the gold film and shows that the maximum transmission is mostly dependent on ohmic losses. Table 8.6, shows the estimated fit parameters. The estimated inductance was calculated from the resonant frequency and capacitance fits.

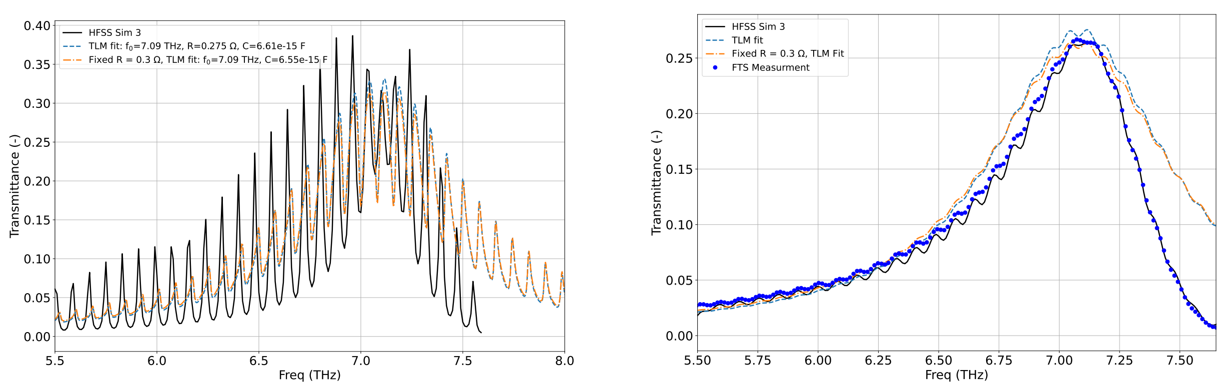

Figure 8.11: *Left*: Transmission line model (TLM) fits to HFSS Sim 3 in Fig. 8.9. Black Line: Simulated transmission of HFSS Sim 3 in Fig. 8.9. Blue Dashed Line: TLM fit to HFSS Sim 3 with three fit parameters: f_0, R and C. Orange Dashed-Dotted Line: TLM fit to HFSS Sim 3 with 2 fit parameters: f_0 and C. R was fixed to the measured gold DC resistance of the fabricated 44 μm MMBP, 0.3 Ω/sq. *Right*: Smoothed TLM fits compared to smoothed HFSS Sim 3 simulated transmission and the 44 μm MMBP measured transmission (dotted blue line).

The same analysis was performed to compare the transmission line model with AR coatings

Table 8.6: TLM fit parameter values for f_0, R, C and L. The middle column contains the fit parameters from the blue dashed line in Fig. 8.11 Left. The right column contains the fit parameters from the orange dashed-dotted line in Fig. 8.11 Left, where R was fixed.

	TLM Fit	Fixed R, TLM Fit
f_0 (THz)	7.09	7.09
R (Ω/sq)	0.275	0.300
C (fF)	6.61	6.55
L (fH)	76.2	76.9

to the simulations and measurements. The fit parameters for the sheet resistance and capacitance listed in the second column of Table 8.6 were taken and applied to the AR coated transmission line model. The AR coating relative permittivity was set to 2.37 for COC and the thickness of the coating was set to 7.2 μm. For COC the measured resonant frequency shifts to 7.1 THz, so this value was used for the f_0 input parameter of the AR coated transmission line model. Fig. 8.12 shows the results of the AR coated model. The transmission of the AR coated model has a peak transmission of 52% and resolving power of R = 7. The resolving power and transmission profile still do not match the measurements for the same reasons listed above for the non-AR coated model. The difference in the peak transmission between the AR coated and non-AR coated model is 26%, which is the same as the difference in the measured transmission. Therefore, the model correctly predicts the increase in transmission when AR coatings are applied to samples with the same sheet resistance and mesh geometry. It also suggests that we achieved the targeted AR coating thickness.

Although the transmission line model does not fully capture the simulation or measurement it is a useful tool, because it enables fast estimation of transmission characteristics as a function of design parameters. It helps us understand how the maximum transmission changes with resistance, allows us to determine how the fringe rate will change with different substrate materials and thicknesses, and predicts the increase in transmission when AR coatings are applied as long as the thickness and relative permittivity of the material is known.

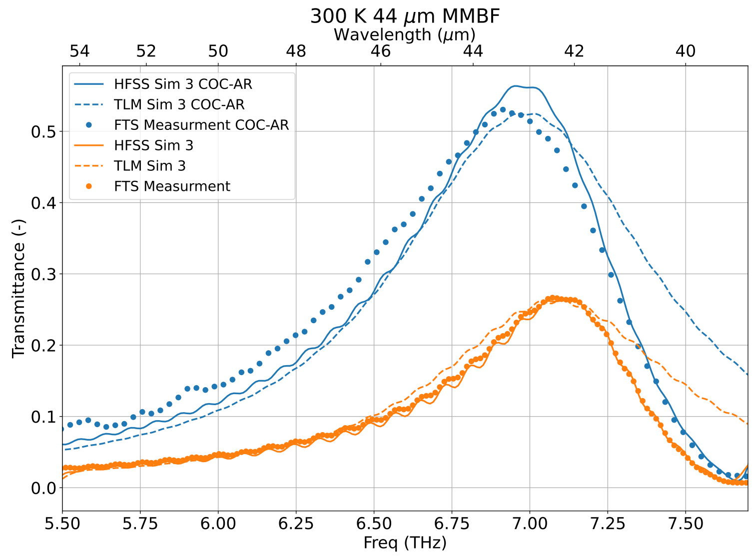

Figure 8.12: Transmission results of the AR coated model along with measured transmission and the HFSS sim 3 simulations. The blue lines are the COC AR coated transmission and the orange lines are the non-AR coated transmission. The dashed lines represent the transmission line model, the dotted lines represent the FTS measurements and the solid lines represent the HFSS simulations.

8.5 Linear Variable Filter Development

Here I present work on a non-AR coated and Parylene™ [1] -AR coated LVF. They were designed to span 24 to 36 μm, with a resolving power of 6. This is in the lower wavelength range of BEGINS. It was designed as prototype filter for preliminary measurements and work towards a flight-ready filter. In this section I compare the design and fabricated LVF, present simulations to predict the transmission of the filter, and discuss the FTS-measured transmission. All simulations and measurement analysis were performed by me, fabrication was performed by Kevin Denis at the GSFC DDL, and filter transmission measurements were made by the GSFC Optics Group.

8.5.1 LVF Design and Fabrication

The prototype LVFs were made of 300-nm thick gold on a high-resistivity floatzone silicon (Si) substrate. The cross-slots vary continuously in size along one direction, referred to as the x-

[1] https://www.hzo.com/technology/material-science/parylene-conformal-coating-services/

direction, for band centers from 24 to 36 μm. Simulations to to determine the cross parameters were done for a bandpass at 24 μm under the assumption that the 300 nm thick gold had a resistivity of 3 $\mu\Omega$-cm and that the Si substrate had no loss. The parameters were then scaled up across the LVF to 36 μm. The design parameters at 24 μm are listed in Table 8.7.

Table 8.7: Design cross parameters for a bandpass peak at 24 μm. These parameters were scaled up to 36 μm for a 17 mm long LVF.

Cross-Parameter	Dimensions (μm)
Cross pitch	6.17
Cross length	4.95
Cross width	0.8

The LVFs were fabricated in the same way as the 44 μm MMBP. However they were not COC-AR coated, but instead coated with Parylene-C, a thermoplastic polymer that is known to have thermal stability, good adhesion properties, and low water absorption. It is a popular AR coating for the THz region (far-IR) because of its high transmission. It has been successfully used between 1 to 8 THz as an AR coating for germanium lenses on the ISO satellite [39]. At THz frequencies its refractive index has been measured to be 1.62 [39]. Non-coated samples were sent to HZO[2] for the parylene coating deposition. They developed a method to deposit a coating with a gradient thickness across the filter. This way the thickness varied to approximately $\lambda/4$ of the bandpass peak across the filter. The filters were diced into 1 inch samples.

Measurements of the cross-slots were made on an LVF sample after fabrication. The measurements were made at y = 3, 8.5, and 12 mm and at positions x = 0, 3, 6, 8, 12, and 17 mm, where the bandpass varies along the x-axis. The top left image in Fig. 8.13 shows an SEM image of the cross-slot at (x,y) = (9, 8.5) mm with an example of how the measurements were made. There was also rounding at the corners of the cross that were measured. The results of the measurements are shown in the bottom panel of Fig. 8.13. The black markers on the first two plots are the average of the measurements made at y = 3, 8.5, and 12 mm which belong to the same bandpass

[2] https://www.hzo.com/technology/material-science/parylene-conformal-coating-services/

peak column at the specified x-position. The left plot shows that the cross widths deviated significantly from the design cross widths. There was an average error in “B-x” of 25% and in “B-y” of 20%. The middle plot shows the measured cross lengths were similar in the horizontal (K-x) and vertical (K-y) directions and had an average error of 3% when compared to the design cross length. The right plot shows the radii of the rounding at the cross corners. The inner radii are the radii of the corners at the cross ends and the outer radii are the radii of the corners at the cross intersection, as shown in the top right image of Fig. 8.13. This measurement was only made at y = 8.5 mm. The measurement was difficult, so it was repeated four times at each x-position. The dots are the average of the four measurements. The error bars are the average uncertainty in the measurement. On average the inner radii were 470 nm $\pm$ 110 nm and the outer radii were 375 $\pm$ 54 nm. The cross modifications were added to the simulations to determine how the bandpass peak would shift before AR coating the samples to calculate the correct AR coating thickness. The LVF gold resistivity was measured to be 2.94 $\mu\Omega$-cm and was included in the modified simulations, as well. Incorporating these modifications shifted the simulated bandpass peak from 24 μm to 23.82 μm. Therefore, the bandpass peak was predicted to vary from 23.82 μm to 35.74 μm across the 17 mm filter which required a Parylene-C thickness that varied from $\sim$3.7 μm to 5.5 μm.

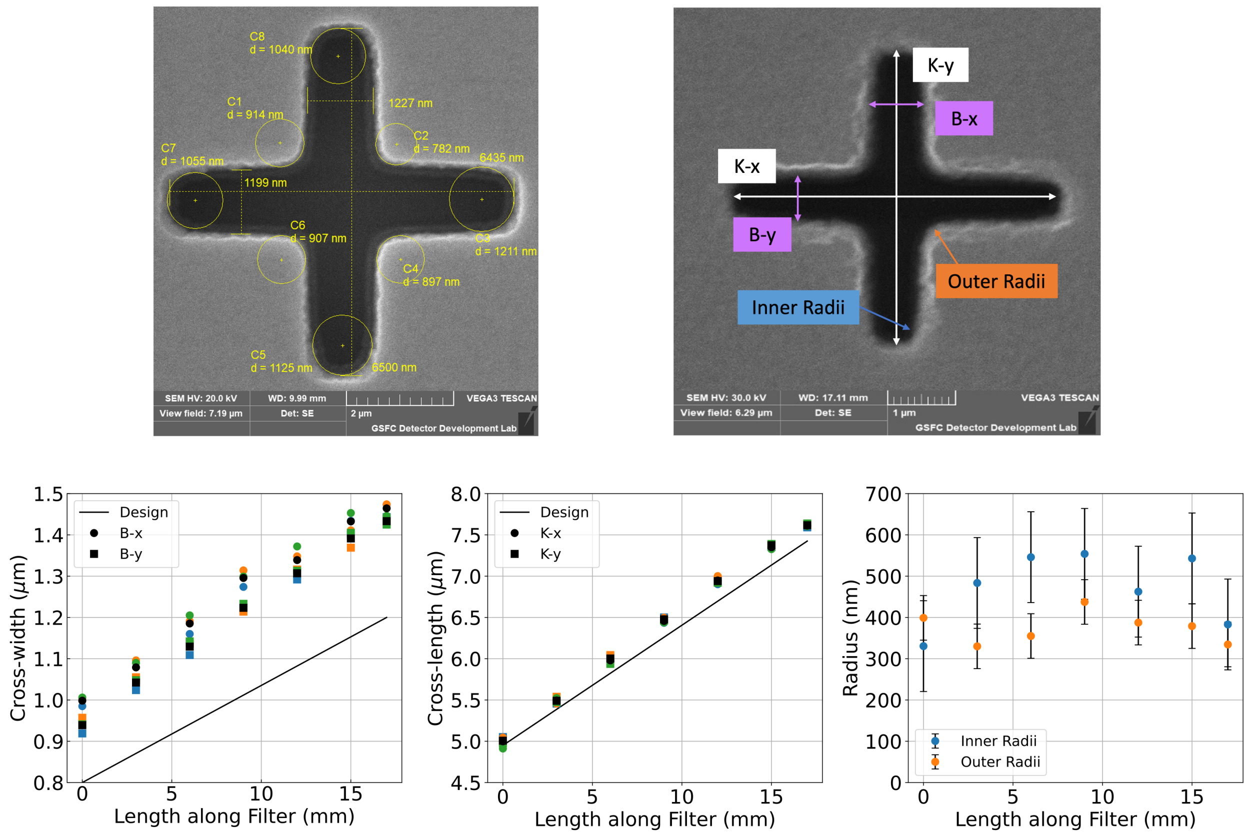

Figure 8.13: *Top Left*: SEM image of the cross-slot at (x,y) = (9, 8.5) mm. *Top Right*: SEM image with labels referencing the measurements plotted in the bottom panel of the figure. *Bottom*: Plots showing the results of the fabricated cross parameters as a function of length along the 17 mm filter. The left plot shows the measurements of the cross width in the horizontal (B-x) and vertical (B-y) directions. The solid line is the design dimension. The different color markers represent the measurements made at y = 3, 8.5, and 12 mm, which belong to the same bandpass peak column at the specified x-position. The black markers are the average of the measurements made at y = 3, 8.5, and 12 mm. The middle plot shows the measurements of the cross length in the horizontal (K-x) and vertical (K-y) directions. The solid line is the design dimension. The black markers are the average of the measurements made at y = 3, 8.5, and 12 mm. The right plot, plots the average inner radii and outer radii of the corners of the crosses across the length of the filter. This measurement was only made at y = 8.5 mm.

8.5.2 LVF Comparison of Simulations to Measurements

Room temperature (300 K) and cryogenic temperature FTS measurements (5 K) were made of two different LVF samples. One sample was non-AR coated and the other was AR coated on both sides with Parylene-C. The measurements were made with an FTS resolution of 2 cm^{-1} and a 2 mm aperture. In this section I discuss the FTS measurements results and compare them to simulations.

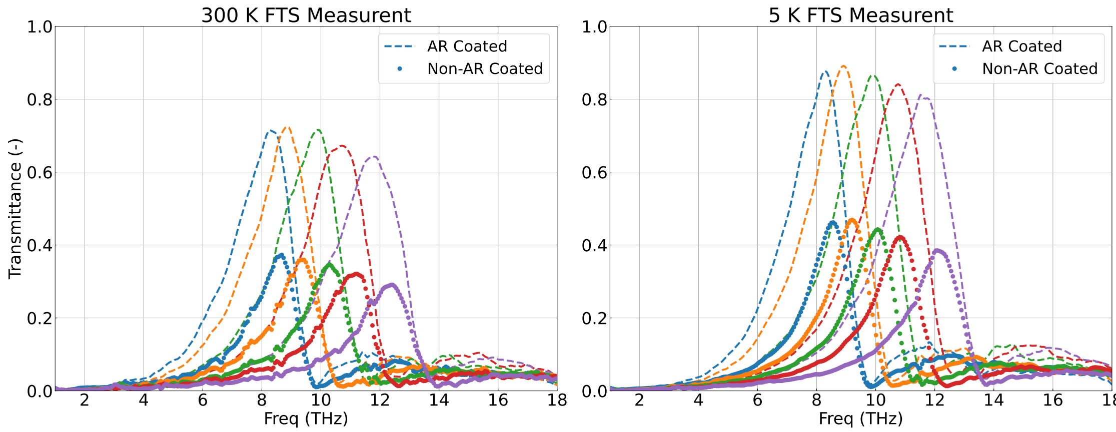

Figure 8.14: LVF FTS measurements at x = 3, 6, 9, 12 and 15 mm. *Left*: Measurements of the AR coated (dashed lines) and non-AR coated (dotted lines) at 300 K. *Right*: Measurements of the AR coated (dashed lines) and non-AR coated (dotted lines) at 5 K.

Fig. 8.14 shows the measured transmission across the LVF at locations x = 3, 6, 9, 12, 15 mm with an uncertainty of ±1.25 mm. This uncertainty is derived from the size of the aperture and the uncertainty of the location of the aperture, which is 0.5 mm. The left plot shows the transmission of the AR and non-AR coated samples at 300 K and the right plot shows their transmission at 5 K. The 5 K transmission is greater due to a decrease in lattice vibrations in the Si which decreases the random motion of electrons. From 300 K to 5 K, the non-AR coated samples increase in transmission by ∼10% and the AR coated sample increase in transmission by ∼17%, whereas simulations predict an increase of 7% and 10% for the non-AR coated and AR coated samples, respectively. The addition of AR coatings increases the transmission at the bandpass peak by 35% at 300 K and 42% at 5 K, whereas simulations predict an increase in transmission of 38% at 300 K and 41% at 5 K. Considering how sensitive the transmission profile is to the cross features the measured and simulated values are in good agreement.

Grating lobes are also identified in the measured transmission. However these measurements only span 0 to 19 THz, so only the first grating lobe is shown. For the non-AR coated sample the first grating lobe increases in peak transmission along the filter from ∼4%-8% and ∼5.5%-9.5% for the 300 K and 5 K measurements, respectively. For the AR coated sample the peak transmission of the grating lobes does not vary drastically and stays around 10% and 12.5 % at 300 K and 5 K, respectively. The addition of the AR coating cause the grating lobes to increase in transmission, but fractionally less than the increase in transmission of the bandpass peak where the quarter-wave AR coating is more effective. This out-of-band transmission is undesirable for BEGINS, but is an inherent property of the periodicity of the cross-slot filter design. However, this out-of-band transmission has been shown to decrease significantly with different aperture geometries and stacking mesh filters [65]. Through simulations we will experiment with both methods to further reduce and if possible eliminate the grating lobes for the next prototype LVF.

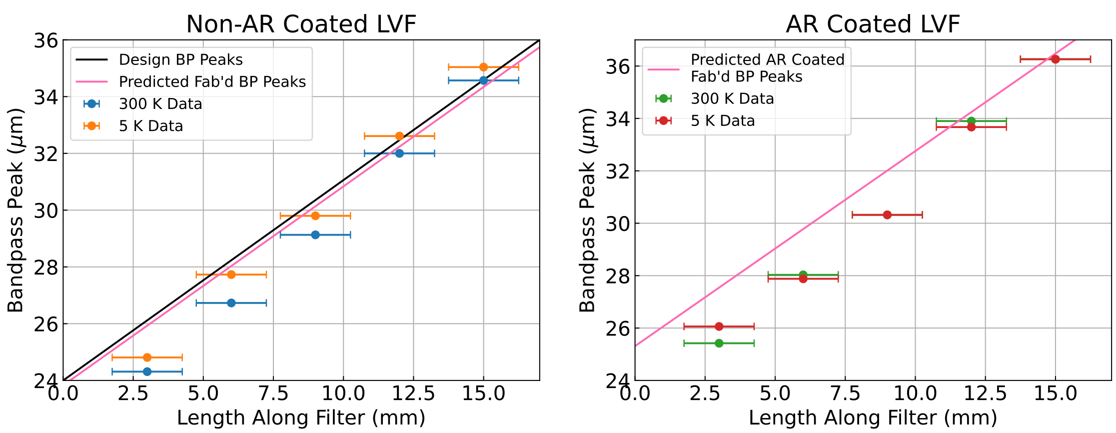

Figure 8.15: Plots of the bandpass peak as a function of length along the LVF. *Left*: Non-Ar coated LVF sample. Black line: expected design bandpass beak. Pink line: Predicted bandpass peak after the modification discussed in Sec. 8.5.1 were made to the cross. Blue dots: Bandpass peaks for the 300 K measurements. Orange dots: Bandpass peaks for the 5 K measurements. *Right*: AR coated LVF sample. Pink line: Predicted bandpass peak after the modification discussed in Sec. 8.5.1 were made to the cross and AR coating were applied. Green dots: Bandpass peaks for the 300 K measurements. Red dots: Bandpass peaks for the 5 K measurements.

We also examined how the bandpass peak center wavelengths compare between simulations and measurements. Fig. 8.15 shows how the measured and predicted bandpass peaks vary along the filter. The black line shows the expected design bandpass beak, before the modifications discussed in Sec. 8.5.1 were made to the cross. The pink line is the predicted bandpass peak after the modifications to the cross were made. There is only a 0.7% difference between the design and modified predicted bandpass peaks along the filter. The orange and blue dots represents the 5 K and 300 K non-AR coated LVF measurements, respectively. The error bars take into account the 0.5 mm tolerance in sample holder location and the 2 mm aperture. There is an average of 0.9 μm and 0.6 μm difference between the 300 K and 5 K measurements when compared to the predicated bandpass peaks for the modified cross (pink line), respectively. This should not be a problem for the BEGINS LVF, since there is 5 % design tolerance in the BEGINS bandpass peak center. There is also an average difference in the bandpass peak center of 0.7 μm between the 5 K and 300 K non-AR coated LVF measurements. Since the resistivity is the only characteristic that should change from 300 K to 5 K we would expect the 300 K and 5 K peak bandpass wavelengths to be the same. The difference is likely due to the uncertainty in the initial placement of the sample holder.

The right plot in Fig. 8.15 shows the same results but for the AR coated LVF. The measured bandpass peaks at 300 K and 5 K in this case are more similar, with an average difference of 0.2 μm. This further supports the hypothesis that the difference in the bandpass peak wavelengths between 300 K and 5 K are due to the sample holder alignment. Also, as shown by the pink line in Fig. 8.15 right panel, there is an average of 1.2 μm difference between the measured and predicted bandpass peaks. The slightly larger deviation in comparison to the non-AR coated sample could be due to fabrication variations in the cross features. However this is still within the BEGINS tolerance.

Finally, we also discuss the results of the transmission and resolving power of the crosses along the LVF. It is important to achieve high transmission such that the filters do not limit the amount of power received by the detectors. Fig. 8.16 shows how the measured transmission and resolving power vary along the filter. The squares represent the simulated transmission and resolving power for the bandpass at x=0 mm. The circles show the measured transmission and resolving power. The measured transmission increases along the length of the filter or as the bandpass increases. This is expected, since all the cross features (cross width, cross length and cross pitch) are scaled up with

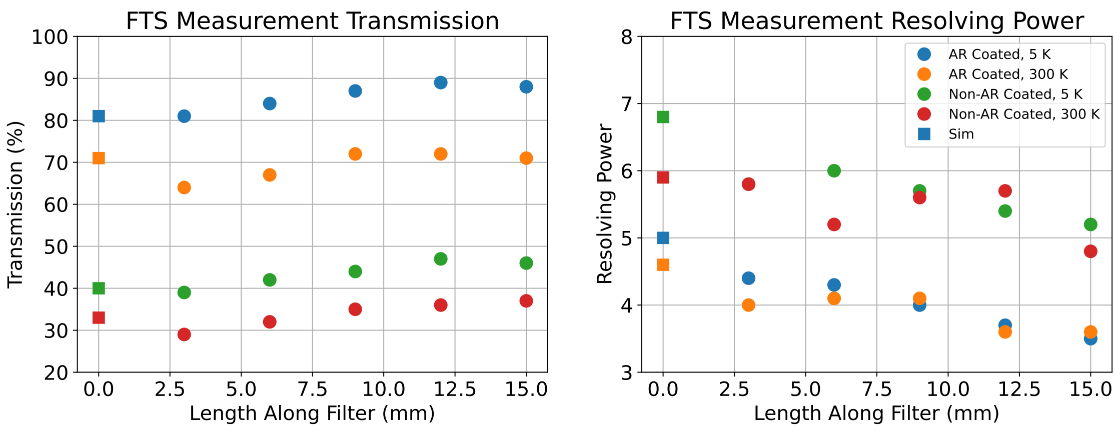

Figure 8.16: *Left*: Dots: Measured transmission along the filter. Squares: Simulated transmission for bandpass at x=0 on the filter. *Right*: Dots: Measured resolving power along the filter. Squares: Simulated resolving power for bandpass at x=0 on the filter.

the bandpass to preserve the resolving power along the filter, and the transmission is proportional to the cross width. Also, note that the measured transmission at x=3 mm is generally lower than the simulation at x=0 mm. This is likely due to the convolution of a range of bandpasses within the 2 mm FTS aperture, whereas the simulation assumes uniform cross features and bandpass. The AR coated filters measured at 5 K have high transmission and show that the gradient AR coating works well to increase transmission by the expected amount.

The resolving power should stay constant, however, it appears to decrease along the length of the filter. This could be due to the discrepancies between designed and fabricated cross-slot parameters along the filter. At both 300 K and 5K the resolving power of the AR-coated sample varies from ~ 4.5 to 3.5 along the length of the filter, and for the non-AR coated sample varies from ~ 6 to 5. The measured resolving power is on average 0.85 less than the simulated resolving power. This occurs because varying bandpasses within the 2 mm FTS aperture decrease the resolving power, whereas the simulation assumes a uniform bandpass. In order to reduce the spread in resolving power along the filter, the filters need to be made with higher resolution lithography to better match design cross-slot parameters and reduce the radii of the rounded corners. The filters are currently made with ion milling lithography. If better resolution cannot be achieved with this technique, another fabrication method to test is electron beam lithography.

8.6 Conclusion and Future Work

We successfully fabricated, measured, and modeled a non-AR coated and AR coated 44 μm MMBP filter and BEGINS prototype LVF with high transmission when AR coated. When cooled to cryogenic temperatures the LVF displayed a transmission greater than 80%. Comparisons between simulations and measurements show how the filter's response is sensitive to changes in the design cross-slot features when fabricated. Incorporating the changes in the cross-slot features after fabrication allows us to model our measurements more accurately. However, for the LVF this is more challenging since the cross parameters are changing across the filter. There was a 4% percent difference between the measured and predicted bandpass peak centers which is within the 5% tolerance for the BEGINS LVF. We also discovered that for the LVF the measured resolving power decreased along the length of filter. This can be improved with higher resolution lithography, in which the fabricated cross-slot geometry will more closely match the design geometry. To combat out-of-band power transmitted in the grating lobes we will experiment with different mesh aperture geometries to further reduce or eliminate the grating lobes for the next prototype LVF. Lastly, the transmission line model developed helps us to understand how the maximum transmission changes with resistance, determine how the fringe rate changes with substrate material and thicknesses, and predicts the increase in transmission when AR coatings are applied.

Chapter 9

Conclusions and Future Work

In this thesis I have discussed my contribution towards the technological advancement of KIDs and metal-mesh LVFs for mid- to far-IR observatories, specifically the proposed sub-orbital and orbital observatories BEGINS and PRIMA. Both observatories have the potential to demonstrate new technology and enable new observations in mid- to far-IR astronomy. Below I highlight my accomplishments and future work.

TiN KIDs for BEGINS: In this chapter I discussed the design and characterization of a 25 μm BEGINS KID prototype array which was optically coupled to a Fresnel zone plate lens array. We discovered that although the FZP lenses provide a quick path to optical measurements they do not efficiently focus radiation onto the KID absorber/inductor. This, along with possible stray light in our cryostat, is likely the reason that the empirical NEP was a factor of 1.2 above the required NEP of 7.58×10^{-17} W/$\sqrt{\text{Hz}}$ for $\lambda = 25$ μm. To improve the NEPs the next prototype array will be bonded to a Si microlens array. This will ensure that the inductors do not absorb stray light from neighboring lenses. We have already fabricated a new 25 μm BEGINS TiN KID prototype array for microlens array bonding. The inductor volumes of the new array were reduced to 70 μm to increase responsivity. This work also displayed the use of PPCs as the capacitor geometry for KIDs to reduce S_{TLS} and reduce KID pixel size. We found that the S_{TLS} was comparable to KIDs with IDCs.

Mid-IR KIDs for GEP: The Galaxy Evolution Probe (GEP) was the predecessor concept probe to PRIMA. The shortest detection wavelength was 10 μm, compared to 25 μm for PRIMA.

In this chapter I presented an inductor geometry for aluminum KIDs sensitive to wavelengths of 10 μm and preliminary dark measurement of a prototype array. This is not within a wavelength range that has been well developed for KIDs. The inductor was shown to have around 73% absorption efficiency through simulations. From dark measurements the T_c and α were estimated to be 1.32 K and 0.763, respectively. This device was made with IDCs and had an estimated $S_{TLS} = 2.84\times10^{-16}$ Hz^{-1}. The measured S_{TLS} limits the predicted NEP of the array. However, employing PPCs like those in BEGINS and PRIMA decreases the NEP. After this work we shifted our focus to PRIMA KIDs and did not continue to optical measurements for NEPs of the device. This work is still promising for future observatories that plan to utilize KIDs in this wavelength range.

Aluminum KIDs for PRIMA: In this chapter I discussed the first generation of PRIMA KIDs and characterization of a 25 μm PRIMA KID prototype array optically coupled to a Si microlens array. This work displayed the successful bonding of a microlens array to the back-side of a KID array and successful optical measurements. The most sensitive detector on the prototype array was photon-noise limited down to 0.1 fW with a limiting detector NEP $\sim 6.5\times10^{-19}$ W/$\sqrt{\text{HZ}}$. This is greater than the PRIMA NEP requirement at 25 μm which is on the order of 2.5×10^{-19} W/$\sqrt{\text{Hz}}$. We found that short quasiparticle lifetimes around 50-150 μs and TLS noise were limiting the NEP. To address the short quasiparticle lifetimes we changed the fabrication method to the method used on aluminum KID arrays for the longer wavelength range of PRIMA. This array employed electron beam lithography over UV stepper lithography and displayed lifetimes on the order of 1 ms. Preliminary measurements of the new 25 μm prototype array have shown improved lifetimes around 1 ms and NEPs below the PRIMA requirement. The inductor volume of the new array was also decreased to improve responsivity. We will investigate TLS noise by testing IDCs against PPCs on the same array to determine which reduces TLS noise. This chapter also included a derivation to determine the absorption efficiency of the KID absorbers from FTS measurements of a 1-inch Si substrate with the KID aluminum inductor trace patterned on it. This derivation can be applied to FTS measurements of detectors with other inductor geometries.

Linear Variable Filter Development for BEGINS: In this chapter I present the development and characterization of a 44 μm MMBP and prototype LVF for BEGINS. I explain how the filter can be modeled through simulations and present a transmission line model. We successfully developed an AR coated LVF with high transmission of over 80% at cryogenic temperatures. This is a promising start for the future LVFs to be employed in BEGINS and possibly PRIMA. Comparisons between simulations and measurements show how the filter's response is sensitive to changes in the design cross-slot features when fabricated. Incorporating the changes in the cross-slot parameters after fabrication allowed us to model our measurements more accurately. There is still work to be done to improve the filters because of the high frequency grating lobes that will introduce power at undesired wavelengths. To combat the grating lobes we will experiment with different aperture geometries to further reduce and if possible eliminate the grating lobes for the next prototype LVF.

Bibliography

[1] Nireos. what is hyperspectral imagaing? `https://www.nireos.com/hyperspectral-imaging/`. Accessed: 2023-10-16.

[2] Identification of carbon dioxide in an exoplanet atmosphere. Nature, 614(7949):649–652, 2023.

[3] Baraa F Al-Azzawi, Jonathan M Rigelsford, and Richard J Langley. A systematic transmission line model for the analysis of self-resonant structures within multi-layer dielectric media. IEEE Transactions on Microwave Theory and Techniques, 67(10):4118–4129, 2019.

[4] S Aslam, RK Achterberg, SB Calcutt, V Cottini, NJ Gorius, T Hewagama, PG Irwin, CA Nixon, G Quilligan, M Roos-Serote, et al. Advanced net flux radiometer for the ice giants. Space Science Reviews, 216(1):1–20, 2020.

[5] Shahid Aslam, Michael Amato, Neil Bowles, Simon Calcutt, Tilak Hewagama, Joseph Howard, Carly Howett, Wen-Ting Hsieh, Terry Hurford, Jane Hurley, et al. Dual-telescope multi-channel thermal-infrared radiometer for outer planet fly-by missions. Acta Astronautica, 128:628–639, 2016.

[6] R Barends, S Van Vliet, JJA Baselmans, SJC Yates, JR Gao, and TM Klapwijk. Enhancement of quasiparticle recombination in ta and al superconductors by implantation of magnetic and nonmagnetic atoms. Physical Review B, 79(2):020509, 2009.

[7] Alyssa Barlis. Development of Kinetic Inductance Detectors for Far-infrared Spectroscopy in Astrophysics. University of Pennsylvania, 2019.

[8] Samir Beldi, Faouzi Boussaha, Jie Hu, Alessandro Monfardini, Alessandro Traini, Florence Levy-Bertrand, Christine Chaumont, Manuel Gonzales, Josiane Firminy, Florent Reix, et al. High q-factor near infrared and visible al 2 o 3-based parallel-plate capacitor kinetic inductance detectors. Optics express, 27(9):13319–13328, 2019.

[9] J Böhm, S Wulff, C Honingh, K Jacobs, and P Warzanowski. Cryogenic temperature-dependence of hrfz silicon refractive index from mid-to far-ir down to 5 k. In 2021 46th International Conference on Infrared, Millimeter and Terahertz Waves (IRMMW-THz), pages 1–2. IEEE, 2021.

[10] Ari D Brown, Shahid Aslam, JA Chervenak, Wei-Chung Huang, Willie C Merrell, Manuel Quijada, Rosalind Steptoe-Jackson, and Edward J Wollack. Radiation hard bandpass filters for mid-to far-ir planetary instruments. In International Workshop on Instrumentation for Planetary Missions, volume 1683, page 1107, 2012.

[11] John H Burnett, Eric C Benck, Simon G Kaplan, Erik Stover, and Adam Phenis. Index of refraction of germanium. Applied Optics, 59(13):3985–3991, 2020.

[12] L Cardani, I Colantoni, A Cruciani, S Di Domizio, M Vignati, F Bellini, N Casali, MG Castellano, A Coppolecchia, C Cosmelli, et al. Energy resolution and efficiency of phonon-mediated kinetic inductance detectors for light detection. Applied Physics Letters, 107(9), 2015.

[13] Salvatore Celozzi, Rodolfo Araneo, Paolo Burghignoli, and Giampiero Lovat. Frequency selective surfaces. 2023.

[14] Mark Clampin. The james webb space telescope (jwst). Advances in Space Research, 41(12):1983–1991, 2008.

[15] Anita L Cochran, Anny-Chantal Levasseur-Regourd, Martin Cordiner, Edith Hadamcik, Jérémie Lasue, Adeline Gicquel, David G Schleicher, Steven B Charnley, Michael J Mumma, Lucas Paganini, et al. The composition of comets. Space Science Reviews, 197:9–46, 2015.

[16] Grégoire Coiffard, BA Mazin, M Daal, P Szypryt, G Ulbricht, and N Zobrist. Parallel plate microwave kinetic inductance detectors. In Low Temperature Detectors (LTD) workshop, Japan, 2017.

[17] Nicholas Cothard. Parallel plate capacitor aluminum kids for far-infrared space-based observatories. Journal of Low Temperature Physics, LTD 20 Proceeding(Submitted), 2023.

[18] JT Cox and G Hass. Antireflection coatings for germanium and silicon in the infrared. JOSA, 48(10):677–680, 1958.

[19] JE Davis. Bandpass interference filters for very far infrared astronomy. Infrared Physics, 20(4):287–290, 1980.

[20] Peter K Day, Henry G LeDuc, Benjamin A Mazin, Anastasios Vayonakis, and Jonas Zmuidzinas. A broadband superconducting detector suitable for use in large arrays. Nature, 425(6960):817–821, 2003.

[21] Ilse De Looze, Diane Cormier, Vianney Lebouteiller, Suzanne Madden, Maarten Baes, George J Bendo, Médéric Boquien, Alessandro Boselli, David L Clements, Luca Cortese, et al. The applicability of far-infrared fine-structure lines as star formation rate tracers over wide ranges of metallicities and galaxy types. Astronomy & Astrophysics, 568:A62, 2014.

[22] Steven AH De Rooij, Jochem JA Baselmans, Vignesh Murugesan, David J Thoen, and Pieter J De Visser. Strong reduction of quasiparticle fluctuations in a superconductor due to decoupling of the quasiparticle number and lifetime. Physical Review B, 104(18):L180506, 2021.

[23] Pieter J de Visser, JJA Baselmans, Juan Bueno, Nuria Llombart, and TM Klapwijk. Fluctuations in the electron system of a superconductor exposed to a photon flux. Nature communications, 5(1):3130, 2014.

[24] PJ De Visser. Quasiparticle dynamics in aluminium superconducting microwave resonators. 2014.

[25] P Diener, HG Leduc, SJC Yates, YJY Lankwarden, and JJA Baselmans. Design and testing of kinetic inductance detectors made of titanium nitride. Journal of Low Temperature Physics, 167:305–310, 2012.

[26] CT Donnan, DJ McLeod, JS Dunlop, RJ McLure, AC Carnall, R Begley, F Cullen, ML Hamadouche, RAA Bowler, D Magee, et al. The evolution of the galaxy uv luminosity function at redshifts z 8–15 from deep jwst and ground-based near-infrared imaging. Monthly Notices of the Royal Astronomical Society, 518(4):6011–6040, 2023.

[27] Simon Doyle, Phil Mauskopf, Chris Dunscombe, Adrian Porch, and Jack Naylon. A lumped element kinetic inductance device for detection of thz radiation. In 2007 Joint 32nd International Conference on Infrared and Millimeter Waves and the 15th International Conference on Terahertz Electronics, pages 450–451. IEEE, 2007.

[28] Simon Doyle, Jack Naylon, Philip Mauskopf, Adrian Porch, Stafford Withington, David Goldie, Dorota M Glowacka, Jochem JA Baselmans, Stephen JC Yates, and Henk Hoevers. Lumped element kinetic inductance detectors for far-infrared astronomy. In Millimeter and Submillimeter Detectors and Instrumentation for Astronomy IV, volume 7020, pages 239–248. SPIE, 2008.

[29] BT Draine and Aigen Li. Infrared emission from interstellar dust. iv. the silicate-graphite-pah model in the post-spitzer era. The Astrophysical Journal, 657(2):810, 2007.

[30] BT Draine, Aigen Li, Brandon S Hensley, Leslie Kipp Hunt, K Sandstrom, and J-DT Smith. Excitation of polycyclic aromatic hydrocarbon emission: dependence on size distribution, ionization, and starlight spectrum and intensity. The Astrophysical Journal, 917(1):3, 2021.

[31] Duncan Farrah, Kimberly Ennico Smith, David Ardila, Charles M Bradford, Michael Dipirro, Carl Ferkinhoff, Jason Glenn, Paul Goldsmith, David Leisawitz, Thomas Nikola, et al. Far-infrared instrumentation and technological development for the next decade. Journal of Astronomical Telescopes, Instruments, and Systems, 5(2):020901–020901, 2019.

[32] GG Fazio, JL Hora, LE Allen, MLN Ashby, P Barmby, LK Deutsch, J-S Huang, S Kleiner, M Marengo, ST Megeath, et al. The infrared array camera (irac) for the spitzer space telescope. The Astrophysical Journal Supplement Series, 154(1):10, 2004.

[33] Daniel Flanigan. Kinetic inductance detectors for measuring the polarization of the cosmic microwave background. PhD thesis, Columbia University, 2018.

[34] Adalyn Elizabeth Blenman Fyhrie. Increasing the Detail and Sensitivity of Far-Infrared/Submillimeter Observations in Astrophysics: Kinetic Inductance Detector Development and Molecular Gas Dynamics in Galaxy Merger NGC 6240. PhD thesis, University of Colorado at Boulder, 2019.

[35] Jiansong Gao. The physics of superconducting microwave resonators. California Institute of Technology, 2008.

[36] Jiansong Gao, Miguel Daal, John M Martinis, Anastasios Vayonakis, Jonas Zmuidzinas, Bernard Sadoulet, Benjamin A Mazin, Peter K Day, and Henry G Leduc. A semiempirical model for two-level system noise in superconducting microresonators. Applied Physics Letters, 92(21):212504, 2008.

[37] Jiansong Gao, MR Vissers, MO Sandberg, FCS Da Silva, Sae Woo Nam, DP Pappas, DS Wisbey, EC Langman, SR Meeker, BA Mazin, et al. A titanium-nitride near-infrared kinetic inductance photon-counting detector and its anomalous electrodynamics. Applied Physics Letters, 101(14), 2012.

[38] Jiansong Gao, J Zmuidzinas, A Vayonakis, P Day, B Mazin, and H Leduc. Equivalence of the effects on the complex conductivity of superconductor due to temperature change and external pair breaking. Journal of Low Temperature Physics, 151(1-2):557–563, 2008.

[39] AJ Gatesman, J Waldman, M Ji, C Musante, and S Yagvesson. An anti-reflection coating for silicon optics at terahertz frequencies. IEEE microwave and guided wave letters, 10(7):264–266, 2000.

[40] J Glenn, A Kogut, E Sharp, G Cataldo, T Essinger-Hileman, E Switzer, K Denis, K Rostem, B Hensley, E Rosolowsky, et al. Begins: The balloon experiment for galactic infrared science. In American Astronomical Society Meeting Abstracts, volume 53, pages 232–01, 2021.

[41] Jason Glenn. Balloon Experiment for Galactic INfrared Science Proposal to NASA ROSES NNH21ZDA001NAPRA. NASA Goddard Space Flight Center, 2021.

[42] Steve Hailey-Dunsheath. Kinetic inductance detectors for the origins space telescope. Journal of Astronomical Telescopes, Instruments, and Systems.

[43] Steven Hailey-Dunsheath. Sensitive mid and far-ir kinetic inductance detector arrays for space astronomy. NASA APRA Proposal, pages 17–APRA17, 2017.

[44] Steven Hailey-Dunsheath, Reinier MJ Janssen, Jason Glenn, Charles M Bradford, Joanna Perido, Joseph Redford, and Jonas Zmuidzinas. Kinetic inductance detectors for the origins space telescope. Journal of Astronomical Telescopes, Instruments, and Systems, 7(1):011015–011015, 2021.

[45] Ryan C Hickox and David M Alexander. Obscured active galactic nuclei. Annual Review of Astronomy and Astrophysics, 56:625–671, 2018.

[46] James R Houck, Thomas L Roellig, Jeff Van Cleve, William J Forrest, Terry Herter, Charles R Lawrence, Keith Matthews, Harold J Reitsema, B Thomas Soifer, Dan M Watson, et al. The infrared spectrograph*(irs) on the spitzer space telescope. The Astrophysical Journal Supplement Series, 154(1):18, 2004.

[47] Johannes Hubmayr, Jim Beall, Dan Becker, H-M Cho, Mark Devlin, Bradley Dober, Chris Groppi, Gene C Hilton, Kent D Irwin, Dale Li, et al. Photon-noise limited sensitivity in titanium nitride kinetic inductance detectors. Applied Physics Letters, 106(7):073505, 2015.

[48] Nur Ismail, Cristine Calil Kores, Dimitri Geskus, and Markus Pollnau. Fabry-pérot resonator: spectral line shapes, generic and related airy distributions, linewidths, finesses, and performance at low or frequency-dependent reflectivity. Optics express, 24(15):16366–16389, 2016.

[49] AP Jones, M Köhler, N Ysard, M Bocchio, and L Verstraete. The global dust modelling framework themis. Astronomy & Astrophysics, 602:A46, 2017.

[50] Elijah Kane. Journal of Low Temperature Physics, 2023.

[51] Steven B Kaplan, CC Chi, DN Langenberg, Jhy-Jiun Chang, S Jafarey, and DJ Scalapino. Quasiparticle and phonon lifetimes in superconductors. Physical Review B, 14(11):4854, 1976.

[52] A Kardakova, M Finkel, D Morozov, V Kovalyuk, P An, C Dunscombe, M Tarkhov, P Mauskopf, TM Klapwijk, and G Goltsman. The electron-phonon relaxation time in thin superconducting titanium nitride films. Applied Physics Letters, 103(25), 2013.

[53] MF Kessler, JA Steinz, ME Anderegg, J Clavel, G Drechsel, P Estaria, J Faelker, JR Riedinger, A Robson, BG Taylor, et al. The infrared space observatory (iso) mission. Astronomy and Astrophysics, Vol. 315, No. 2, p. L27-L31, 315:L27–L31, 1996.

[54] M Stoutimore Khalil, MJA Stoutimore, FC Wellstood, and KD Osborn. An analysis method for asymmetric resonator transmission applied to superconducting devices. Journal of Applied Physics, 111(5), 2012.

[55] Atsuko Kibayashi, Hirokazu Ishino, Yosuke Yamada, Akinori Okamoto, Yosuke Kida, Masashi Hazumi, Nobuaki Sato, and Hiroki Watanabe. Development of lumped element kinetic inductance detectors for phonon and photon detections. In 2015 IEEE International Instrumentation and Measurement Technology Conference (I2MTC) Proceedings, pages 1042–1045. IEEE, 2015.

[56] Charles Kittel. Introduction to solid state physics. John Wiley & sons, inc, 2005.

[57] Shwetank Kumar. Submillimeter wave camera using a novel photon detector technology. California Institute of Technology, 2008.

[58] Henry G Leduc, Bruce Bumble, Peter K Day, Byeong Ho Eom, Jiansong Gao, Sunil Golwala, Benjamin A Mazin, Sean McHugh, Andrew Merrill, David C Moore, et al. Titanium nitride films for ultrasensitive microresonator detectors. Applied Physics Letters, 97(10):102509, 2010.

[59] A Léger, L d'Hendecourt, and D Defourneau. Physics of ir emission by interstellar pah molecules. Astronomy and Astrophysics, 216:148–164, 1989.

[60] A Léger, L d'Hendecourt, and D Defourneau. Physics of ir emission by interstellar pah molecules. Astronomy and Astrophysics (ISSN 0004-6361), vol. 216, no. 1-2, June 1989, p. 148-164., 216:148–164, 1989.

[61] David Leisawitz, Edward Amatucci, Ruth Carter, Michael DiPirro, Anel Flores, Johannes Staguhn, Chi Wu, Lynn Allen, Jonathan Arenberg, Lee Armus, et al. The origins space telescope: mission concept overview. In Space Telescopes and Instrumentation 2018: Optical, Infrared, and Millimeter Wave, volume 10698, pages 363–375. SPIE, 2018.

[62] David Leisawitz, Matteo Bonato, Duncan Farrah, T Tupper Hyde, Aláine Lee, Joshua Bennett Lovell, Brenda Matthews, Lee G Mundy, Conor Nixon, Petr Pokorny, et al. The science case for a far-infrared interferometer in the era of jwst and alma. In Infrared Remote Sensing and Instrumentation XXXI, volume 12686, pages 68–78. SPIE, 2023.

[63] Ian Lowe, Gabriele Coppi, Peter AR Ade, Peter C Ashton, Jason E Austermann, James Beall, Susan Clark, Erin G Cox, Mark J Devlin, Simon Dicker, et al. The balloon-borne large aperture submillimeter telescope observatory. In Ground-based and Airborne Telescopes VIII, volume 11445, pages 1299–1309. SPIE, 2020.

[64] Amy E Lowitz. Kinetic inductance detectors for CMB polarimetry at 100 GHz. The University of Wisconsin-Madison, 2017.

[65] Changgui Lu, Zhengqing Qi, Wengao Guo, and Yiping Cui. A new fold-cross metal mesh filter for suppressing side lobe leakage in terahertz region. Optics Communications, 413:190–195, 2018.

[66] Piero Madau and Mark Dickinson. Cosmic star-formation history. Annual Review of Astronomy and Astrophysics, 52:415–486, 2014.

[67] A Maragkoudakis, E Peeters, and A Ricca. Probing the size and charge of polycyclic aromatic hydrocarbons. Monthly Notices of the Royal Astronomical Society, 494(1):642–664, 2020.

[68] Richard E Matick. Transmission lines for digital and communication networks: an introduction to transmission lines, high-frequency and high-speed pulse characteristics and applications. (No Title), 1969.

[69] Daniel C Mattis and John Bardeen. Theory of the anomalous skin effect in normal and superconducting metals. Physical Review, 111(2):412, 1958.

[70] Benjamin A Mazin. Microwave kinetic inductance detectors. California Institute of Technology, 2005.

[71] Benjamin A Mazin. Microwave kinetic inductance detectors: The first decade. In AIP Conference Proceedings, volume 1185, pages 135–142. American Institute of Physics, 2009.

[72] H McCarrick, D Flanigan, G Jones, BR Johnson, P Ade, D Araujo, K Bradford, R Cantor, G Che, P Day, et al. Horn-coupled, commercially-fabricated aluminum lumped-element kinetic inductance detectors for millimeter wavelengths. Review of Scientific Instruments, 85(12):123117, 2014.

[73] Arline M Melo, Angelo L Gobbi, Maria HO Piazzetta, and Alexandre MPA Da Silva. Cross-shaped terahertz metal mesh filters: Historical review and results. Advances in Optical Technologies, 2012, 2012.

[74] Willie C Merrell, Shahid Aslam, Ari D Brown, James A Chervenak, Wei-Chung Huang, Manuel Quijada, and Edward J Wollack. Compact micromachined infrared bandpass filters for planetary spectroscopy. Applied optics, 51(15):3046–3053, 2012.

[75] KD Möller, JB Warren, JB Heaney, and C Kotecki. Cross-shaped bandpass filters for the near-and mid-infrared wavelength regions. Applied optics, 35(31):6210–6215, 1996.

[76] Alessandro Monfardini, LJ Swenson, Aurélien Bideaud, FX Désert, SJC Yates, Angélique Benoit, AM Baryshev, JJA Baselmans, S Doyle, B Klein, et al. Nika: A millimeter-wave kinetic inductance camera. Astronomy & Astrophysics, 521:A29, 2010.

[77] Engineering National Academies of Sciences and Medicine. Origins, Worlds, and Life: A Decadal Strategy for Planetary Science and Astrobiology 2023-2032. The National Academies Press, Washington, DC, 2022.

[78] Craig W Nelson, Archita Hati, and David A Howe. Phase inversion and collapse of cross-spectral function. Electronics letters, 49(25):1640–1641, 2013.

[79] G Neugebauer, HJ Habing, R Van Duinen, HH Aumann, B Baud, CA Beichman, DA Beintema, N Boggess, PE Clegg, Teije De Jong, et al. The infrared astronomical satellite (iras) mission. Astrophysical Journal, Part 2-Letters to the Editor (ISSN 0004-637X), vol. 278, March 1, 1984, p. L1-L6. Research supported by the Science and Engineering Research Council and NASA., 278:L1–L6, 1984.

[80] Omid Noroozian. Superconducting microwave resonator arrays for submillimeter/far-infrared imaging. PhD thesis, California Institute of Technology, 2012.

[81] Omid Noroozian, Jiansong Gao, Jonas Zmuidzinas, Henry G LeDuc, and Benjamin A Mazin. Two-level system noise reduction for microwave kinetic inductance detectors. In AIP Conference Proceedings, volume 1185, pages 148–151. American Institute of Physics, 2009.

[82] A Paiella, ES Battistelli, MG Castellano, I Colantoni, F Columbro, A Coppolecchia, G D'Alessandro, P De Bernardis, S Gordon, L Lamagna, et al. Kinetic inductance detectors and readout electronics for the olimpo experiment. In Journal of Physics: Conference Series, volume 1182, page 012005. IOP Publishing, 2019.

[83] A Paiella, A Coppolecchia, MG Castellano, I Colantoni, A Cruciani, A D'Addabbo, P de Bernardis, S Masi, and G Presta. Development of lumped element kinetic inductance detectors for the w-band. Journal of Low Temperature Physics, 184(1-2):97–102, 2016.

[84] A Pallottini, S Gallerani, A Ferrara, B Yue, L Vallini, R Maiolino, and C Feruglio. Mapping metals at high redshift with far-infrared lines. Monthly Notices of the Royal Astronomical Society, 453(2):1898–1909, 2015.

[85] Z Pan, KR Dibert, J Zhang, PS Barry, AJ Anderson, AN Bender, BA Benson, T Cecil, CL Chang, R Gualtieri, et al. Noise optimization for mkids with different design geometries and material selections. IEEE Transactions on Applied Superconductivity, 33(5):1–8, 2023.

[86] GL Pilbratt, JR Riedinger, T Passvogel, G Crone, D Doyle, U Gageur, AM Heras, C Jewell, L Metcalfe, S Ott, et al. Herschel space observatory-an esa facility for far-infrared and submillimetre astronomy. Astronomy & Astrophysics, 518:L1, 2010.

[87] Klaus M Pontoppidan, Jaclyn Barrientes, Claire Blome, Hannah Braun, Matthew Brown, Margaret Carruthers, Dan Coe, Joseph DePasquale, Néstor Espinoza, Macarena Garcia Marin, et al. The jwst early release observations. The Astrophysical Journal Letters, 936(1):L14, 2022.

[88] David W Porterfield, JL Hesler, R Densing, ER Mueller, TW Crowe, and RM Weikle. Resonant metal-mesh bandpass filters for the far infrared. Applied Optics, 33(25):6046–6052, 1994.

[89] David M Pozar. Microwave engineering. John wiley & sons, 2011.

[90] K Sakai and T Yoshida. Single mesh narrow bandpass filters from the infrared to the submillimeter region. Infrared Physics, 18(2):137–140, 1978.

[91] Shigeyuki Sako, Takashi Miyata, Tomohiko Nakamura, Takashi Onaka, Yuji Ikeda, and Hirokazu Kataza. Developing metal mesh filters for mid-infrared astronomy of 25 to 40 micron.

In Advanced Optical and Mechanical Technologies in Telescopes and Instrumentation, volume 7018, pages 1696–1705. SPIE, 2008.

[92] Jack Sayers, Clint Bockstiegel, Spencer Brugger, Nicole G Czakon, Peter K Day, Thomas P Downes, Ran P Duan, Jiansong Gao, Amandeep K Gill, Jason Glenn, et al. The status of music: the multiwavelength sub-millimeter inductance camera. In Millimeter, Submillimeter, and Far-Infrared Detectors and Instrumentation for Astronomy VII, volume 9153, pages 57–74. SPIE, 2014.

[93] James A Schlaerth. Microwave kinetic inductance detector camera development for millimeter-wave astrophysics. PhD thesis, University of Colorado at Boulder, 2010.

[94] Seth Robert Siegel. A Multiwavelength Study of the Intracluster Medium and the Characterization of the Multiwavelength Sub/millimeter Inductance Camera. California Institute of Technology, 2016.

[95] Hunter RJ Stevenson, Jared E Payne, Joseph Eddy, Brad Ferguson, Ryan T Beazer, Gregory N Nielson, and Stephen M Schultz. Verification of metal-mesh filter response via ansys hfss simulation. In 2023 Intermountain Engineering, Technology and Computing (IETC), pages 288–292. IEEE, 2023.

[96] Orazio Svelto, David C Hanna, et al. Principles of lasers, volume 1. Springer, 2010.

[97] LJ Swenson, PK Day, BH Eom, HG Leduc, N Llombart, CM McKenney, O Noroozian, and J Zmuidzinas. Operation of a titanium nitride superconducting microresonator detector in the nonlinear regime. Journal of Applied Physics, 113(10), 2013.

[98] Eric Switzer. Exclaim: Kinetic inductance detector physics model.

[99] VP Tomaselli, DC Edewaard, P Gillan, and KD Möller. Far-infrared bandpass filters from cross-shaped grids. Applied Optics, 20(8):1361–1366, 1981.

[100] Reinhard Ulrich. Far-infrared properties of metallic mesh and its complementary structure. Infrared Physics, 7(1):37–55, 1967.

[101] Michael R Vissers, Jiansong Gao, David S Wisbey, Dustin A Hite, Chang C Tsuei, Antonio D Corcoles, Matthias Steffen, and David P Pappas. Low loss superconducting titanium nitride coplanar waveguide resonators. Applied Physics Letters, 97(23), 2010.

[102] Alexander B Walter, Neelay Fruitwala, Sarah Steiger, John I Bailey, Nicholas Zobrist, Noah Swimmer, Isabel Lipartito, Jennifer Pearl Smith, Seth R Meeker, Clint Bockstiegel, et al. The mkid exoplanet camera for subaru scexao. Publications of the Astronomical Society of the Pacific, 132(1018):125005, 2020.

[103] Michael W Werner, TL Roellig, FJ Low, George H Rieke, M Rieke, WF Hoffmann, E Young, JR Houck, B Brandl, GG Fazio, et al. The spitzer space telescope mission. The Astrophysical Journal Supplement Series, 154(1):1, 2004.

[104] Jordan Wheeler. Millimeter-Wave Galaxy Spectroscopy: SuperSpec On-Chip Spectrometer Technology Development and ALMA Observations of Molecular Gas in the Arp 220 Nucleus. University of Colorado at Boulder, 2019.

[105] James C Wiltse. The fresnel zone-plate lens. In Millimeter wave technology III, volume 544, pages 41–47. SPIE, 1985.

[106] Edward J Wollack, Kevin L Denis, Alyssa Barlis, Meng-Ping Chang, Alexander S Kutyrev, Kevin H Miller, and Peter C Nagler. Far-infrared properties of cyclic olefin copolymer. Optics Letters, 45(3):780–783, 2020.

[107] Alwyn Wootten and A Richard Thompson. The atacama large millimeter/submillimeter array. Proceedings of the IEEE, 97(8):1463–1471, 2009.

[108] Jonas Zmuidzinas. Superconducting microresonators: Physics and applications. Annu. Rev. Condens. Matter Phys., 3(1):169–214, 2012.

[109] Jonas Zmuidzinas, B Mazin, A Vayonakis, P Day, and HG LeDuc. Multiplexable kinetic inductance detectors. In Proceedings far–IR, sub–mm, and mm detector workshop, edited by J. Wolf, J. Farhoomand, and CR McCreight volume NASA CP/211408, 2002.